US ARMY
MATERIEL
COMMAND

AD

# TECHNICAL REPORT BRL-TR-2722

# RADIAL EXPANSION OF CAVITIES PRODUCED BY THE AXISYMMETRIC STEADY PENETRATION OF HYPERVELOCITY RODS

Brian R. Scott

April 1986

DTIC
ELECTE
S JUN 0 3 1986
D
D

# US ARMY BALLISTIC RESEARCH LABORATORY
## ABERDEEN PROVING GROUND, MARYLAND

86 6 2 072

| REPORT DOCUMENTATION PAGE | | READ INSTRUCTIONS BEFORE COMPLETING FORM |
|---|---|---|
| 1. REPORT NUMBER<br>Technical Report BRL-TR-2722 | 2. GOVT ACCESSION NO.<br>ADA 168 186 | 3. RECIPIENT'S CATALOG NUMBER |
| 4. TITLE *(and Subtitle)*<br>Radial Expansion of Cavities Produced by the Axisymmetric Steady Penetration of Hypervelocity Rods | | 5. TYPE OF REPORT & PERIOD COVERED<br>Technical Report |
| | | 6. PERFORMING ORG. REPORT NUMBER |
| 7. AUTHOR(s)<br>Brian R. Scott | | 8. CONTRACT OR GRANT NUMBER(s) |
| 9. PERFORMING ORGANIZATION NAME AND ADDRESS<br>US Army Ballistic Ressearch Laboratory<br>ATTN: SLCBR-TB<br>Aberdeen Proving Ground, MD 21005-5066 | | 10. PROGRAM ELEMENT, PROJECT, TASK AREA & WORK UNIT NUMBERS<br>RDTE 1L162618AH80 |
| 11. CONTROLLING OFFICE NAME AND ADDRESS<br>US Army Ballistic Research Laboratory<br>ATTN: SLCBR-DD-T<br>Aberdeen Proving Ground, MD 21005-5066 | | 12. REPORT DATE<br>April 1986 |
| | | 13. NUMBER OF PAGES<br>112 |
| 14. MONITORING AGENCY NAME & ADDRESS(*if different from Controlling Office*) | | 15. SECURITY CLASS. *(of this report)*<br>UNCLASSIFIED |
| | | 15a. DECLASSIFICATION/DOWNGRADING SCHEDULE |

16. DISTRIBUTION STATEMENT *(of this Report)*

Approved for public release; distribution unlimited.

17. DISTRIBUTION STATEMENT *(of the abstract entered in Block 20, if different from Report)*

18. SUPPLEMENTARY NOTES

19. KEY WORDS *(Continue on reverse side if necessary and identify by block number)*

| | | |
|---|---|---|
| hole growth | ballistic impact | hypervelocity |
| hole volume | plasticity | shaped charge jet |
| craters | elasticity | kinetic energy penetrator |
| cavities | visco-plastic | |
| penetration | initial value problems | |

20. ABSTRACT *(Continue on reverse side if necessary and identify by block number)*

A model for the expansion of a cavity created during the penetration of high-speed rods is presented. This model was formulated by making several assumptions as to the behavior of the deforming target material during the cavity expansion process. The assumptions are supported by previous experimental and finite difference investigations. Upon specification of the matching conditions at the boundaries of the plastic deformation regions, the governing system of nonlinear field equations reduces to simpler ordinary

DD $_{1\ JAN\ 73}^{FORM}$ 1473    EDITION OF 1 NOV 65 IS OBSOLETE

differential equations. Initial conditions are estimated and the resulting initial value problems are solved with a standard Runge-Kutta technique. Parametric trends are subsequently established and the model predictions compare quantitatively well with experimental observations. It is concluded that the model accurately predicts the proper behavior but the accuracy of results depends significantly upon the precision with which the initial conditions and the target material characteristics may be specified.

## TABLE OF CONTENTS

## TABLE OF CONTENTS (cont)

## LIST OF ILLUSTRATIONS

# LIST OF ILLUSTRATIONS (cont)

# I.  INTRODUCTION AND STATEMENT OF THE PROBLEM

The collision of high speed projectiles with solid targets has been a subject of considerable interest to military, industrial and academic communities for the past four decades.  World War II stimulated analytic research oriented towards improving armor and warhead designs.  The advent of the space program in the late fifties created a need for the protection of spacecraft from meteorite impact.  Industrial applications of impact and penetration processes include mining operations, oil well stimulation, plate, cable and pipe cutting, demolitions and many others.

The subject of impact mechanics is quite broad.  It incorporates such classical fields as fluid mechanics, solid mechanics, solid state physics, mathematics and materials science into the analytical and experimental treatments of complex, practical problems.  Several general reference texts are available that review the many impact type applications as well as the research techniques developed and applied with relative success (Backman [1], Billington [2], Goldsmith [3], Johnson [4], Kinslow [5], Zukas [6], etc.).  Review articles dealing primarily with spacecraft protection can be found in the Proceedings of the Hypervelocity Impact Symposia [7], held during the early sixties (Allison [8], Cook [9], Hopkins [10], etc.) and in the open literature (Backman [11], Bjork [12], Cook [13], Eichelberger [14], Herrmann [15, 16], Prater [17], Vinson [18], etc.).  Review articles concerned with military armor applications can be found in government publications (Bethe [19], Perez [20], Wright [21], etc.) as well as in the open literature (Byrnside [22], Christman [23, 24], Eichelberger [25], Gehring [26], Jonas [27], Sagamonyan [28], etc.).  Both of the aforementioned categories involve the penetration of high speed projectiles into target materials (armor or shields).  The space application (conventionally termed hypervelocity impact) typically involves geometrically compact projectiles (meteorites) with impact velocities ranging from 1 to 80 km/s and targets configured from thin metallic plates.  Military armor on the other hand is considerably more massive often involving metal target thicknesses on the order of hundreds of centimeters. The projectiles, which these armors are designed to stop, usually have long cylindrical geometries and impact velocities significantly less (1-12 km/s) than the meteor class.  In both categories (hypervelocity impact and armor penetration) however, the penetrator velocities are sufficiently great to produce impact stresses much greater than the resisting strength of the target materials.  Consequently, a crater forms within the target in a time frame of the order of microseconds.  The penetrator may disintegrate if the impact velocity approaches the 12 km/s range; it will certainly deform within the range of 1-12 km/s, the extent of which will depend on the relative magnitudes of the impact stresses and characteristic strengths.  Hypervelocity, within the impact mechanics community, is usually defined as a projectile velocity which exceeds the longitudinal wave speed of the target material.  Most metals have wave speeds between 2 and 7 km/s.  Therefore, depending on the target, some typical impact velocities may be less than the hypervelocity definition. However, within the context of this report, hypervelocity will define a velocity sufficient to both deform the penetrator and produce a target cavity. For most conventional metallic penetrators, an impact velocity greater than 1 km/s will be considered hypervelocity.

Figure 1 depicts three typical situations involving the impact of representative projectiles upon thin and thick targets.  The projectile trajectories are normal to the target surfaces.
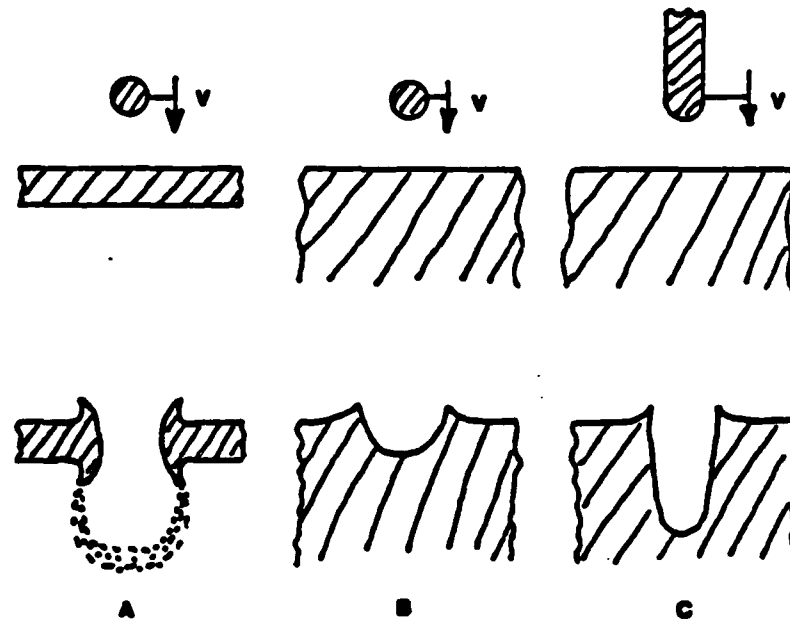
Figure 1. Three Impact Configurations, Before and After the Event

Configurations A and B represent the hypervelocity, meteorite impact category. As noted in the already referenced papers, these configurations have been extensively studied experimentally (Cook [9], Prater [17], Abbott [29], Holloway [30], Johnson [31], Keys [32], Kineke [33], Pond [34], Turpin [35], Yuan [36], etc.), analytically using engineering models (Davids [37], Fuchs [38], Öpik [39], Rae [40], Rand [41], Rostoker [42], Seizew [43], Silberstein [44], Scott [45], Taylor [46], Whitesides [47], Zaid [48], etc.) and numerically via finite difference/finite element methods (Bjork [12], Hardage [49], Riney [50, 51, 52], Sedgewick [53], Wilkins [54], etc.). The problem is very complex; wave propagation, unknown dynamic material properties, phase changes, fracture, time-dependent boundary conditions, nonequilibrium thermodynamics, etc., all combine to prevent a general analytic solution. Knowledge is gleaned from the many analyses of results using varying degrees of approximation. Fortunately, most of the above sources of analytic difficulty have been investigated either independently or in specific combinations making the hypervelocity impact category of problems rather well understood. Such is not the case for the configuration C of Figure 1.

While much of the behavior evident in the two other configurations occurs also in long penetrator/thick armor applications, the problem is considerably different. Most obvious is the shape of the resulting crater, which appears almost hemispherical in B but becomes more cylindrical as the length of the penetrator increases. Also, the process of cavity enlargement, completed rather quickly in A and B, will take considerably longer when the length of the penetrator increases. Indeed, it is this extra time of interest that hinders the application of the finite difference techniques to the deep penetration problem. Only a few numerical studies have been published (Harlow

8

[55], Kucher [56, 57], etc.) and consequently much less is understood, especially with respect to individual problem parameter dependence. This deep penetration problem has, however, been of considerable interest to the defense community for many years. Protective armors of tanks and armored personnel carriers have in the past been designed with understanding gained from combined experimental and engineering model research approaches. The experiments (Birkhoff [58], Boyle [59], Brooks [60], Cook [13], Eichelberger [61, 62], Fugelso [63], Glass [64], Hauver [65], Hohler [66], Johnson [67], Moss [68], Perez [20], Pond [69], Pritchard [70], Summers [71], Weihrauch [72, 73], White [74], etc.) identify physical behaviors and trends that allow for subsequent analytic approximations. Perhaps the single most important parameter in the eyes of the armor designer is the depth to which a projectile will penetrate. Indeed, most of the analytic studies to date have concentrated on the penetration rate behavior (the rate at which the penetrator/target interface moves along the penetration trajectory). Christman [24] describes the penetration process in terms of four phases: transient, primary, secondary and recovery. Figure 2 shows, schematically, these four phases in terms of pressure-time behavior.
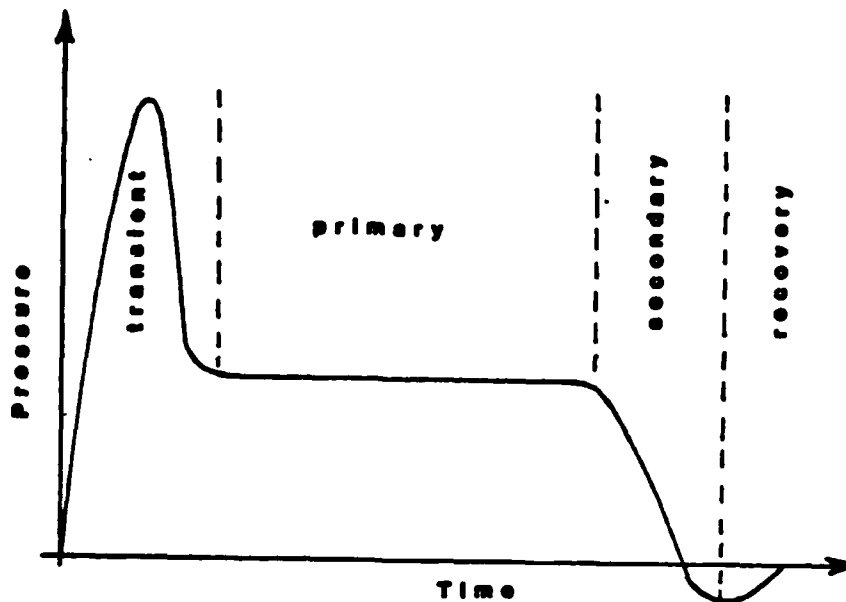


Figure 2. The Four Phases of High-Velocity Penetration,
Christman [24]

Upon initial impact, shock waves form, optical flashes are observed and the pressures measured are quite high. The shocks spread into the target ahead of the penetrator with diminishing intensity due to both geometrical divergence and material effects (Mok [75], Rae [40], Torvik [76], etc.). If the penetrator has sufficient length, then the penetration process enters a quasi-steady phase where pressures, less than the transient case, and along the penetration trajectory are almost constant. An interaction zone, encompassing the penetrator/target interface, moves with a constant characteristic velocity deeper into the target, eroding penetrator material as it progresses. Eventually, the rear of the penetrator enters this moving interaction zone and upon being eroded, the process enters the secondary phase. The penetrator is no longer important, the momentum imparted to the target by the first two phases is gradually reduced by irreversible mechanisms until the static strength properties of the target predominate, allowing for reversible recovery to occur. This overall process has been observed experimentally (Boyle [59], Christman [24], Eichelberger [77]) and in finite difference calculations (Harlow [55], Kucher [57]). The extent and relative importance of each individual phase depends upon both the penetrator and target characteristics. For meteorite impact problems, the primary or quasi-steady phase never materializes while for very long penetrators, this particular phase accounts for the majority of the penetration process. The most serious threat to ballistic armor involves both long rods (fired from propellant driven guns, .5-3 km/s) and very long metallic jets (2-12 km/s), produced by the detonation of shaped charge warheads. Under the presumption that the pressures generated greatly exceed the material strength of the target, the theory for deep steady penetration was developed during the World War II era. A one-dimensional, incompressible, streamline analogy yielded estimates for the penetration rate and final penetration depth. The derivation and subsequent verification (experimental and computational) along with a review of some of the assumption relaxations of this model are presented in Appendix A. Many analytic efforts have considered the penetration behavior along the penetration trajectory (Alekseevskii [78], Birkhoff [58], Hill [79], Majerus [80], Perez [81], Sagamonyan [82], Tate [83, 84], Wright [85] and others), but precious few have considered the behavior orthogonal to the penetration path. Wright [21] points out the many limitations associated with the penetration model and notes the need to consider the dynamics of hole growth in the formulation of a more realistic penetration theory. The growth of the target cavity, along directions orthogonal to the penetration trajectory, deep within thick targets is the subject of this report.


The subject of this report involves the deep penetration of long rods (or jets) into massive targets. Figure 3 shows the essential elements of such a problem.
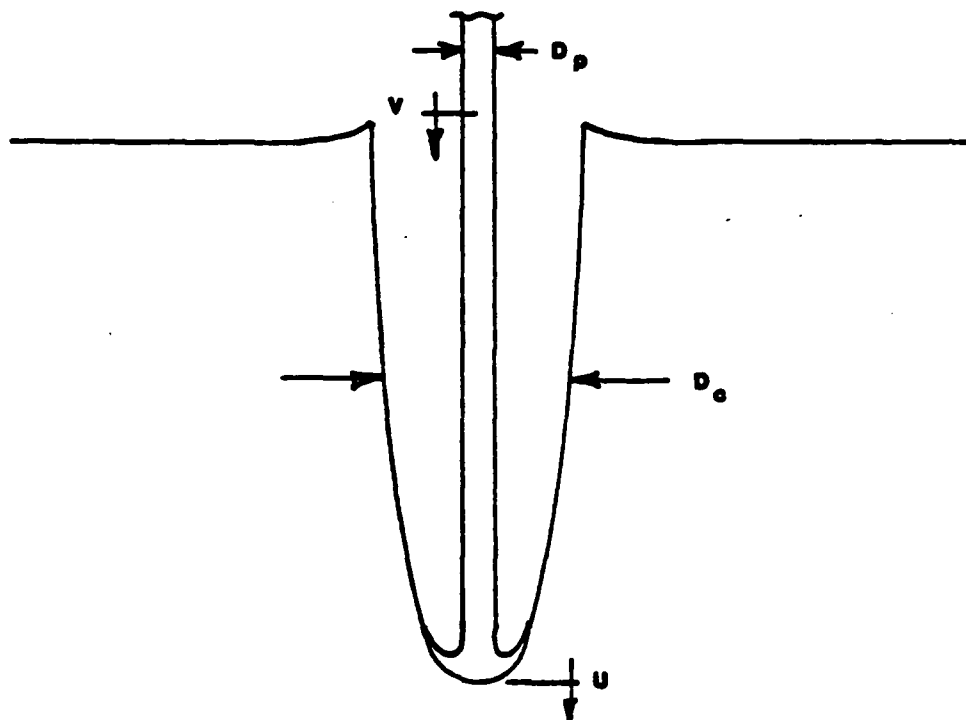
Figure 3. The Deep Penetration of Hypervelocity Rods

A hypervelocity penetrator, characterized by its length (assumed many times greater than its lateral dimension, $D_p$), density and velocity, V, strikes and subsequently penetrates a massive target characterized by its density, strength properties and lateral dimension. A cavity, described by its diameter, $D_c$, at specific depths within the target forms behind a translating interaction surface moving with a characteristic velocity, U. It is the objective of this report to:

a. Develop a model of the dynamic growth of the cavity dimension, $D_c$, and its final value.

b. Determine appropriate initial and/or boundary conditions and solve the system for specific problems.

c. Determine the model's parametric dependence, limits of applicability and predictive accuracy.

d. Improve the fundamental understanding of the penetrator/target interaction.

11

## II. FORMULATION OF THE PROBLEM

The overall objective of this report is to develop a model for the cavity expansion behavior orthogonal to the penetration path and subsequently apply this model to practical impact configurations. Parametric dependencies and model accuracies need to be determined. The analysis may proceed along three different approaches: empirical data correlation, approximate analytical methods, or multidimensional finite difference/finite element computer codes. The empirical approach requires extensive experimental data bases, the dimensionless groupings of important problem parameters are not always obvious and the understanding of the material behavior and physical processes involved is not significantly improved by the effort. Examples of this approach can be found in the review article by Backman and Goldsmith [11]. At the opposite extreme is the numerical approach. The direct approximation of the complete equations of continuum physics, while allowing for the treatment of more general problems, has the disadvantage of obscuring the effects of individual problem parameters. Parametric studies require the repetition of expensive, time-consuming calculations and often the resolution is sacrificed in an attempt to reduce the overall cost. The accuracy of the numerical solutions depends not only on the discretization errors inherent in the method but is severely dependent on the accuracy to which the material behavior may be described. Zukas, et al. [6, 27] review the many contemporary codes, their respective successes and limitations. The intermediate approach, approximate analysis, employs simplifying assumptions which reduce the general field equations to more analytically tractable forms. The most important physical and material behaviors are explicitly retained while less significant behaviors are neglected. Approximations and simplifications should be supported by experimental, theoretical or numerical arguments so that the results may retain reasonable accuracy when compared with the actual complex problem.

This report will follow the analytical modeling approach in hopes of discerning the most significant problem parameters and their influence upon the cavity growth behavior.

The formulation may be considerably simplified from the onset by the application of the assumptions; material isotropy and axial symmetry. In addition to the obvious analytic advantage gained, these approximations simplify the experimental determination of material properties. From a physical viewpoint, both conditions are quite appropriate for the stated problem. Material isotropy is conventionally assumed for homogeneous, amorphous and polycrystalline solids. In the latter case, isotropic properties can be interpreted as averages, taken over continuum samples encompassing many randomly oriented grains, of locally anisotropic properties of individual grains. Since most practical armors are configured with steel or aluminum elements, material isotropy will be assumed throughout the remainder of this report. Subjects involving fiber reinforced materials, composite penetrators or target materials that exhibit significant processing induced anisotropy are, therefore, precluded from further study. The second major approximation, axial symmetry, is quite appropriate for the study of deep penetration. Nearly all practical penetrators have cylindrical geome-tries and are designed to impact a target end on (cylinder axis and trajectory are coincident with the target surface normal). For instances where the penetrator axis is not normal to the target surface (oblique impact), the geometry near the entrance surface of the target invalidates the symmetry

12

assumption, however, it has been observed both experimentally (Weihrauch [72, 73]) and computationally (Kucher [86]) that for depths greater than several rod diameters below the oblique entrance surface, the penetration process appears axially symmetric. Thin plates and behavior near oblique free surfaces will, however, not be considered. The lateral boundaries of the target will be assumed to be either infinite in dimension or finite with cylindrical geometry. Actual targets usually use rectangular plates but the lateral dimensions are so large when compared with the final cavity dimension that the infinite approximation is valid.

Cylindrical, Eulerian coordinates are selected with the origin located at the point of initial impact upon the target top surface. A cylindrical rod (or jet) will penetrate the target along the axis of symmetry (z axis) imparting to elements of mass at each axial plane, an amount of radial momenta sufficient to produce cavity expansion. The penetrator feeds into a translating interaction region (characteristic mushroom shape) where it subsequently inverts and flows parallel to the expanding cavity surface. As noted in the Introduction and as derived in Appendix A, the translating surface moves through the target with an approximately constant rate. Utilization of pulsed x-ray photographic techniques (Weihrauch [72, 73], Fugelso [63], and much unpublished US Army Ballistic Research Laboratory evidence) enables observation of this interaction region during the penetration process. Figure 4 is an example of such an observation. The contrast due to differences in material density allows the identification of the penetrator, cavity and the interaction regions. While the fundamental understanding of the shape and extent of the interaction surface is not quantitatively developed, the experimental results qualitatively describe it as somewhat hemispherical in shape with dimension greater than the penetrator diameter. The experimental results disclose that not only does this surface propagate according to the steady penetration theory but also the shape and extent of the interaction surface appear steady as the penetration process proceeds. This is confirmed by the finite difference calculations of Harlow [55] and Kucher [56, 57]. The results of impact experiments using transparent materials (glass, PMMA, etc.) show that preceding the penetrator "bulb" are observable waves. If the penetration rate, U, exceeds the local sound speed, $c_o$, of the target material, then the wave resembles a bow shock associated with supersonic flow about a blunt body of revolution. Figure 5 is an example of such a case where the target material is PMMA (sound speed, 2.7 km/s) and the penetrator is a metallic jet moving with a penetration rate of 4.5 km/s. Figure 6 is an example of essentially the same configuration except that the target material is glass. Here the characteristic wave speed exceeds the penetration rate and the leading wave is spherical in shape, appears to have originated at the point of initial contact and is diverging as it outruns the penetrator. These observations are described in the experimental papers (Boyle [59], Cook [9], Keys [32], etc.) and confirmed once again in the finite difference calculations of Hardage [49], Harlow [55], Kucher [56, 57] and others. The important point to note is that in either case (subsonic or supersonic) the material ahead of the penetrator has already been accelerated to some unknown degree by the time the penetrator/target interface arrives at a specific axial plane. Figure 7 is a sketch that identifies these characteristics of the subsonic and supersonic penetration cases ($c_o$ represents the elastic wave speed). It will be assumed that this behavior exists also in optically opaque targets, specifically metals. The two most commonly used target metals (steel and aluminum) have elastic wave speeds on the order of 6

13

Figure 4. Flash X-ray Photograph of a Metallic Jet Penetrating a
Semi-infinite Target (Courtesy of Dr. William de Rosset, USABRL)
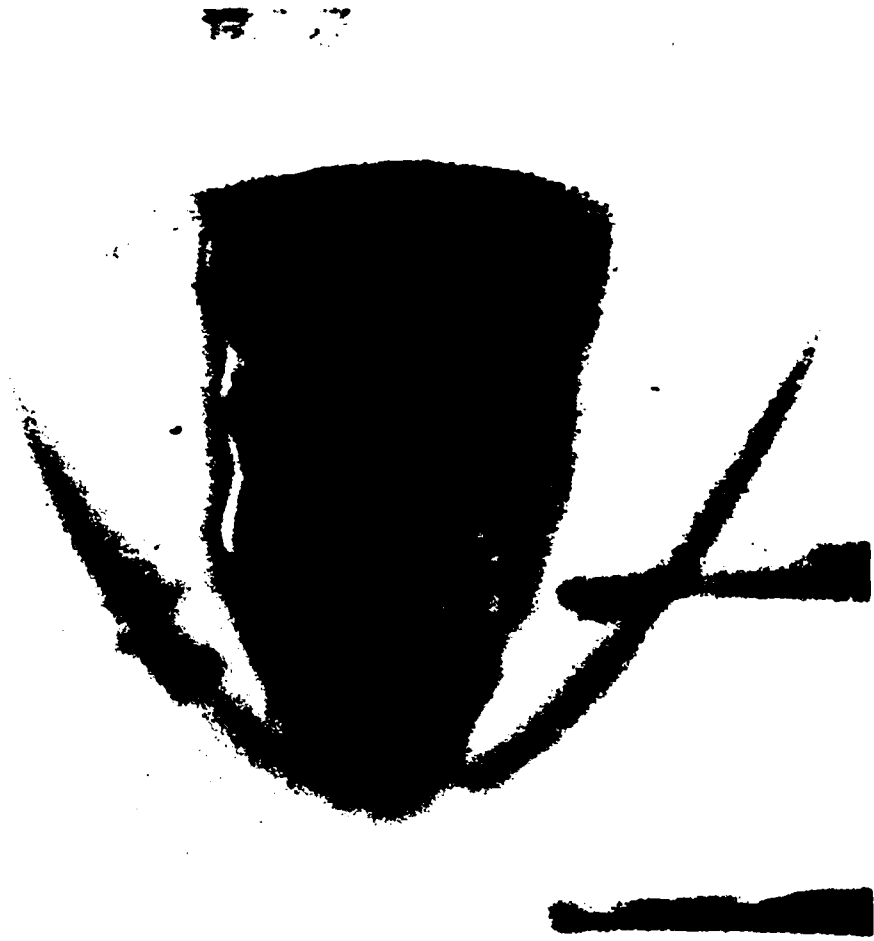
Figure 5. Framing Camera Photograph of a Metallic Jet Penetrating Polymethyl Methacrylate, Supersonic ($U > c_o$) (Courtesy of George Hauver, USABRL)
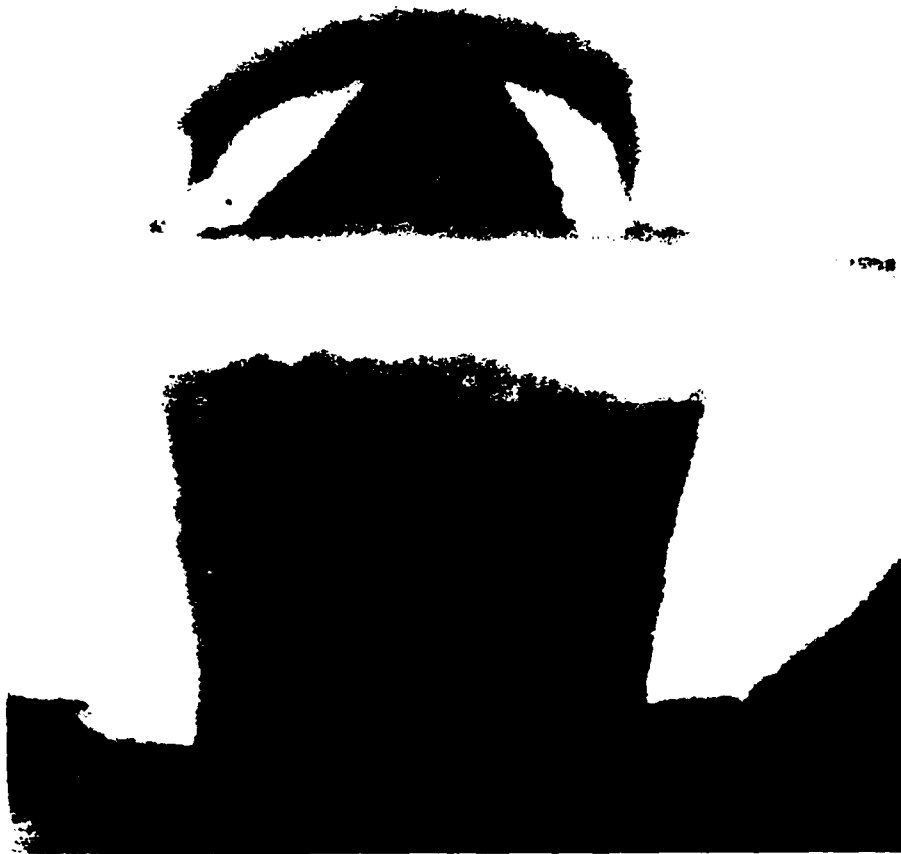
Figure 6. Framing Camera Photograph of a Metallic Jet Penetrating
Glass, Subsonic ($U < c_o$) (Courtesy of George Hauver, USABRL)
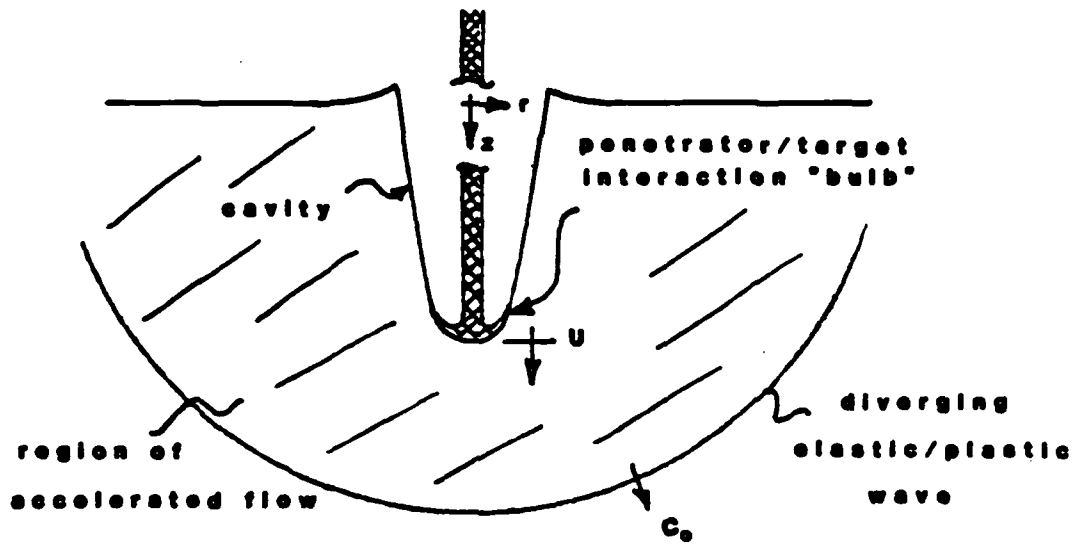
A. Subsonic penetration $(U < C_o)$
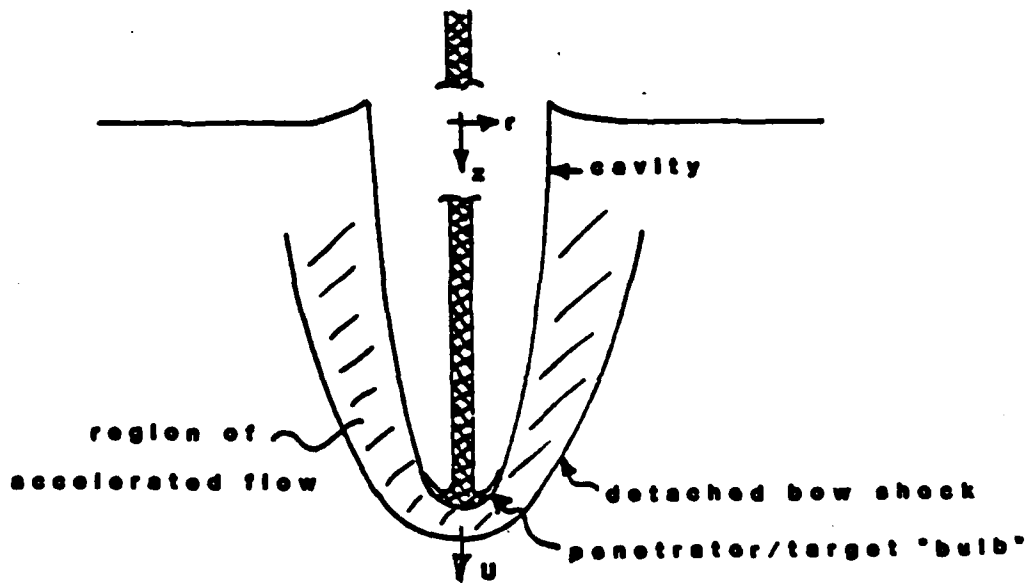
B. Supersonic penetration $(U > C_o)$

Figure 7. Schematic Description of the Deep Penetration Process
for Both High and Low Sound Speed Target Materials

km/s, making the subsonic case likely for most practical applications. The nature and behavior of these impact generated waves in solids has been the subject of considerable research and falls within the general category of wave propagation (Backman [87], Cristescu [88], Davids [37], von Karman [89], Koehler [90], Kolsky [91], Lipkin [92], Mok [75], Wilkins [54], etc.). The subject will be addressed later in this text when boundary conditions are considered.

Up to this point, little has been said about the nature of the material flow within the target that ultimately determines the crater surface. Experiments utilizing wax and plasticine (Frazier [93], Holloway [30], Johnson [67]) and those using metals (Dong [94], Glass [64], Pond [69], Weihrauch [72, 73]) have approached this topic by studying postmortem deformation fields. The embedding of material tracers within the target or the layering of dissimilar plates allows the measurement of displacements and subsequent calculations of finite strain tensors and invariants to be performed. The observations from these experiments may be summarized as follows:

a. Target mass remains essentially constant throughout the penetration process. Some mass is ejected during the initial transient phase as a shear lip forms but as the depth of the cavity increases, this fraction of the total mass becomes negligible.

b. The target density, before and after penetration, varies only slightly (on the order of one percent or less).

c. The target material between the cavity surface and a radial surface slightly larger undergoes finite radial and axial displacements (shear deformation).

d. Beyond this unspecified radius, the deformation appears to be pure radial expansion. The degree of deformation decreases with increasing radial coordinate.

e. For certain polycrystalline targets it is sometimes possible to discern a maximum radius of permanent grain reorganization (limit of plastic deformation).

f. The deformation field is symmetric with respect to the penetration axis.

The above observations involve only the final deformation field. However, Weihrauch [72], using a target composed of copper plates, was able to sequentially observe the penetration of a copper rod during the event. Figure 8A is a sketch of these observations. The surfaces of the individual plates appear to deform in a parallel fashion. Once again, the finite difference calculations of Kucher [56], Figure 8B, agree qualitatively well with these experiments.
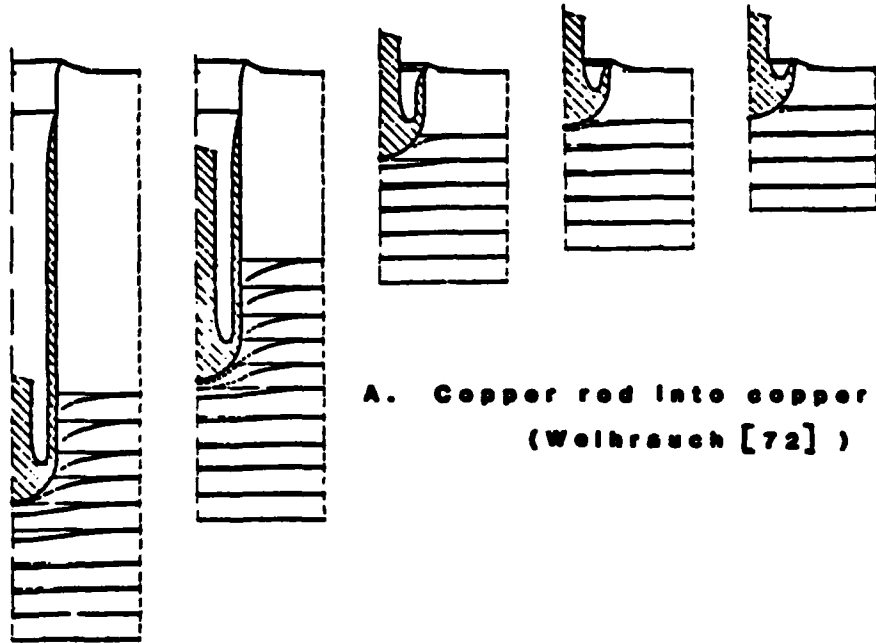
A.  Copper rod into copper plates
    (Weihrauch [72] )
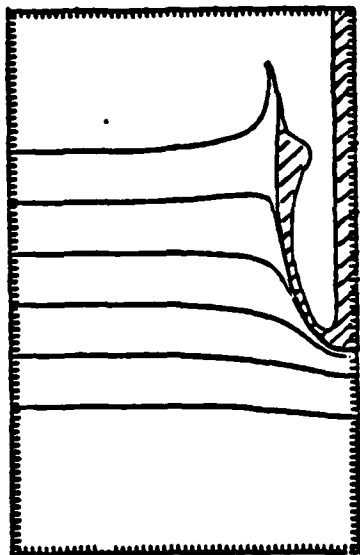
B.  Copper rod into steel plate
    (lines represent tracer surfaces)
    (Kucher [56] )

Figure 8.  Deformation Fields During the Penetration Event

## A. Breakdown into Regions of Different Deformations

With the support of both experimental and numerical evidence, the following situation will be assumed: the deformation of a target being penetrated by a long, axially aligned rod, separates into four distinct but interacting spatial regions. Figure 9 identifies these four regions, ordered according to their relative radial dimensions. The regions are separated by boundaries that translate in time along axial planes (z = constant) as the cavity expands. The wave that precedes the penetrator "bulb" is described as an elastic/plastic wave which propagates with a characteristic wave speed. It separates quiescent target material from that which has been affected in varying degrees by the passing of this wave. The stress distribution within this affected zone, although not quantitatively defined, is expected to vary from negligible magnitudes at the larger radii to the stagnation pressure at the symmetry axis. At some radius, b, the stresses should be sufficient to meet or exceed standard plastic yield criteria. Region IV then represents the part of the target, upon a specific axial plane, that can be appropriately modeled with elasticity theory. Region III, bounded by the radii a' and b, represents target material that undergoes plane radial deformations under stresses greater than the elastic range. Region II involves plastic deformation in both radial and axial directions. It is bounded by the radius, a', and the cavity wall, a. Between the cavity and the axis of symmetry, Region I, the penetrator enters the translating interaction region, inverts and flows along the target cavity. In each individual region, the nature of the deformations will determine the appropriate formulations. The four regions will be ultimately coupled by the requirement of continuity at each of the boundaries. For any specified axial coordinate, the cavity expansion process begins when the penetrator/target "bulb" passes this axial plane and ends when the stresses in the target decay to the point where material strength halts further deformation.

## B. The Elastic Region IV

From the principle of linear momentum, the equations of motion in differential tensor form may be written:

$$\sigma_{ji,j} + b_i = \rho \frac{D}{Dt} U_i \tag{1}$$

where $U_i$ represents the components of the velocity vector, $\sigma_{ji}$ is the stress tensor, $b_i$ is the body force vector, $\rho$ is the density and the operator $\frac{D}{Dt}$, is the material derivative operator. Cylindrical Eulerian coordinates have already been selected and with the assumption of plane axisymmetric deformation, the radial equation of motion is:

$$\frac{\partial \sigma_{rr}}{\partial r} + \frac{\sigma_{rr} - \sigma_{\theta\theta}}{r} + \rho \, b_r = \rho \frac{D}{Dt} U_r \tag{2}$$

where $\sigma_{rr}$ and $\sigma_{\theta\theta}$ are the radial and circumferential stresses, respectively, which are also principal in this configuration. If inertia forces are assumed negligible throughout this region (they certainly are smaller than those in Regions II and III), then in absence of applied body forces, equation (2) simplifies to the plane strain equation of equilibrium:

20
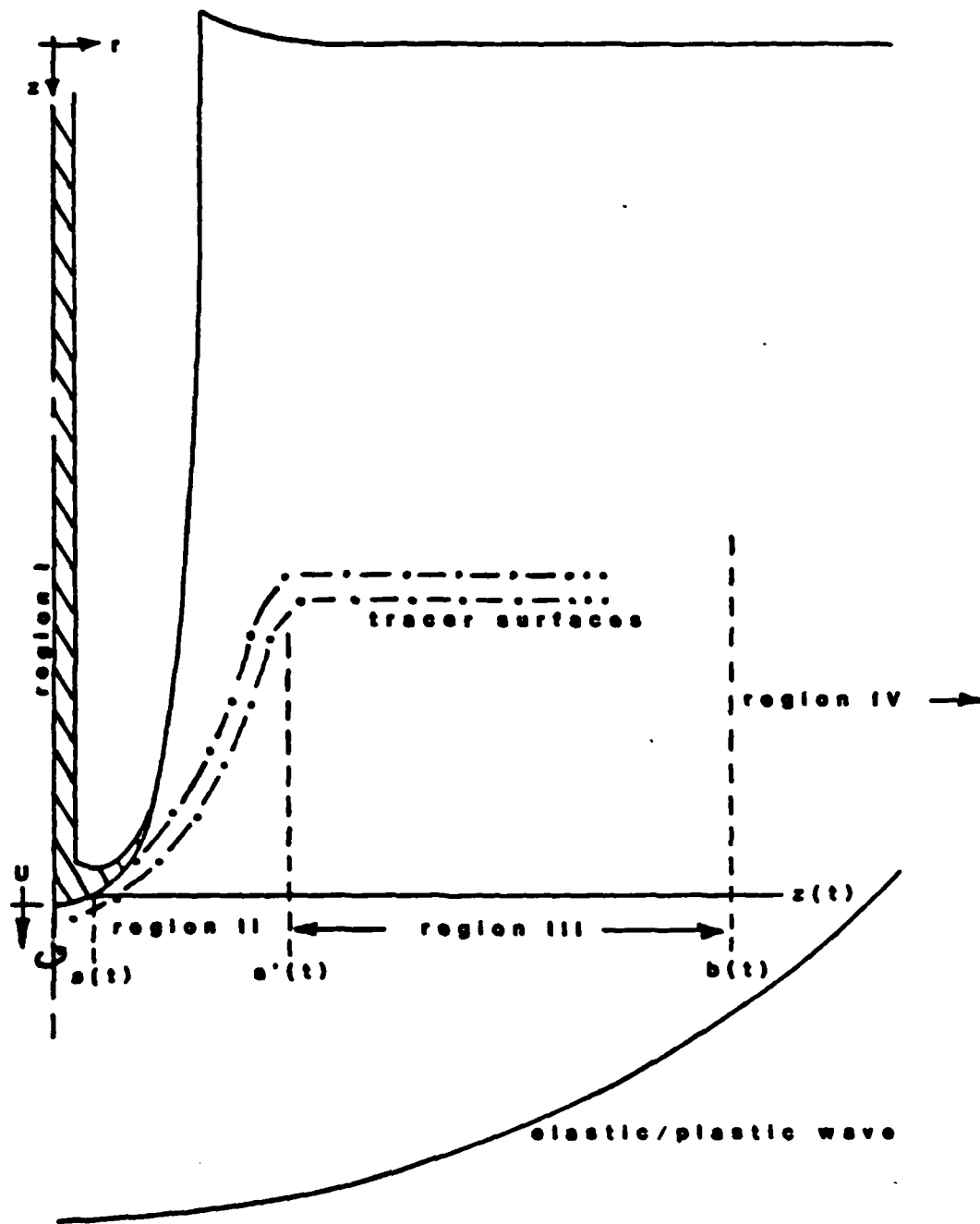
Figure 9.   Sketch of the Separation of the Target into Regions
            of Different Deformations (Subsonic Flow)

$$\frac{\partial \sigma_{rr}}{\partial r} \quad \frac{\sigma_{rr} - \sigma_{\theta\theta}}{r} = 0 \qquad (3)$$

which is appropriate for the elastic loading of a long, thick tube by uniform internal pressure. The solution to this problem is well known (Timoshenko [95]). The stress distribution is of the form:

$$\sigma_{rr} = \frac{K_1}{r^2} + K_0$$

$$\sigma_{\theta\theta} = \frac{-K_1}{r^2} + K_0 \qquad (4)$$

$$\sigma_{zz} = 2\nu K_0$$

where $\nu$ is Poisson's ratio, $K_0$ and $K_1$ are constants determined by application of the boundary conditions and the axial stress, $\sigma_{zz}$, is not zero in general. If the target has relatively large lateral dimension such that the semi-infinite approximation is valid, then it may be assumed that the radial stress vanishes for large radial coordinates. The constant, $K_0$, must therefore be zero and the stress distribution for the semi-infinite target is given by:

$$\sigma_{rr} = \frac{K_1}{r^2}$$

$$\sigma_{\theta\theta} = \frac{-K_1}{r^2} \qquad (5)$$

$$\sigma_{zz} = 0 .$$

If the lateral boundary has a finite dimension, c, the condition that the radial stress vanishes at this boundary yields a slightly different form:

$$\sigma_{rr} = K_0 \left(1 - \frac{c^2}{r^2}\right)$$

$$\sigma_{\theta\theta} = K_0 \left(1 + \frac{c^2}{r^2}\right) \qquad (6)$$

$$\sigma_{zz} = 2K_0 \nu .$$

The remaining undetermined constant, for either case, requires that another boundary condition be specified. This will be accomplished once the formulation in Region III is completed and stress continuity at the elastic/plastic boundary, b, is imposed.

## C. The Plane Plastic Region III

The elastic Region IV utilized the assumptions of axisymmetric plane deformation, negligible inertia effects and small displacements in order to determine the internal stress distributions. The last two approximations are perhaps only accurate for large radial positions, sufficiently far from the penetrator/target interaction "bulb." Region III encompasses material of

22

significantly smaller radii, thereby precluding the use of the same set of assumptions. Experimental evidence supports the contention of a region of axisymmetric planar flow, but also categorizes the deformation as finite and irreversible. The experiments additionally observe that the flow process does not include substantial permanent density change. The numerical studies show that compressibility effects, while not completely negligible, are usually spacially localized around shock surfaces which eventually diverge with time and distance. It is expected that strains as well as strain rates will be large within this region but it will be assumed that throughout the process, incompressibility will apply. The analysis will be limited to plastic, radial deformations.

Let $U_i$ (r, z, $\theta$, t) be the instantaneous velocity components of plastically flowing target material at any given Eulerian coordinate point (r, $\theta$, z). The axial symmetry of the problem requires that the tangential velocity component, $U_\theta$, vanish and the presumption of plane flow eliminates the axial component, $U_z$. Then with respect to a specific axial plane, only the radial velocity, $U_r$, remains. The continuity equation for an incompressible flow is:

$$\frac{\partial U_r}{\partial r} + \frac{U_r}{r} = 0 \tag{7}$$

where $U_r$ varies with radial position, r, and time. The solution to this equation is:

$$U_r = \frac{\dot{\phi}(t)}{r} \tag{8}$$

where $\dot{\phi}(t)$ represents an arbitrary but differentiable function of time. The tensor equations of motion, in terms of the stress tensor, $\sigma_{ij}$, the scalar density, $\rho$, the coordinates, $x_i$, velocity vector, $U_i$, and body force vector, $b_i$, may be written:

$$\rho \left( \frac{\partial u_i}{\partial t} + u_j \frac{\partial u_i}{\partial x_j} \right) = b_i + \frac{\partial \sigma_{ij}}{\partial x_j} . \tag{9}$$

In the absence of body forces, the radial equation of motion for plane axisymmetric flow simplifies with $\left( u_\theta, \frac{\partial}{\partial \theta}, \sigma_{rz}, u_z = 0 \right)$ to:

$$\rho \left( \frac{\partial u_r}{\partial t} + u_r \frac{\partial u_r}{\partial r} \right)^{\cdot} = \frac{\partial \sigma_{rr}}{\partial r} + \frac{\sigma_{rr} - \sigma_{\theta\theta}}{r} . \tag{10}$$

As in the plane elastic Region IV, the stresses are also principal in this configuration. Substitution of equation (8) into equation (10) yields:

$$\rho \left( \frac{\ddot{\phi}}{r} - \frac{\dot{\phi}^2}{r^3} \right) = \frac{\partial \sigma_r}{\partial r} + \frac{\sigma_r - \sigma_\theta}{r} \tag{11}$$

where the dots denote differentiation with respect to time and the stress is described by the principle stress vector. Equation (11) is identical to the governing equation of motion derived by Hill, et al. [79] and later by Appelby

23

[96] and Al-Hassani [97] for a thick walled, incompressible axially constrained tube under uniform internal pressure. Appelby's formulation assumed plane strain deformation, stress free outer boundaries, Tresca yield behavior and a visco-plastic flow rule. Expansion histories of the inner surface were prescribed and the internal pressure, necessary to produce such, was calculated. A comparison was made of the individual contributions of inertia, viscosity and perfect plasticity to this time dependent pressure. The inverse problem of specifying the pressure history and then solving for the velocity and deformation fields was not attempted. An earlier Russian effort, Agagabian [98], considered the same geometrical configuration and very similar relations for plastic yield and flow but allowed only small displacements. The radial equation of motion derived by this author was:

$$\rho \; \frac{\ddot{\varphi}}{r} = \frac{\partial \sigma_r}{\partial r} + \frac{\sigma_r - \sigma_\theta}{r} \qquad (12)$$

which differs from equation (11) in the acceleration term, lacking the contribution of the convective term. With identical boundary conditions as Appelby, Agagabian obtained an exact solution for the stress components (spatial and temporal). Agagabian also considered the case of a very thick tube such that the entire tube was not undergoing plastic deformation. The boundary separating elastic and plastic deformations was assumed continuous with respect to displacements and radial stress. The pressure was applied in a Heaviside step fashion with arbitrary magnitude. Stress distributions as well as the propagation behavior of the elastic/plastic interface were analytically determined. However, the chief limitations of this analysis, when considering the cavity expansion problem, are the small displacement approximation and the specification of unknown pressure history. Since this report is concerned with large radial displacements, the formulation will follow an approach parallel with the work of Hill, Appelby and Al-Hassani.

Returning to equation (11), the term furthest to the right hand side involves the difference of the two principle stresses, $\sigma_r$ and $\sigma_\theta$. The Tresca-Mohr yield criterion (condition of constant maximum shear stress) presumes that the greatest difference between the principle stress components equals twice the inherent material shear strength, $\tau$, (or the uniaxial yield strength in simple tension, $\sigma_y$) if the body is deforming plastically. Within the plane deformation regions of this problem, this criterion may be stated as:

$$|\sigma_r - \sigma_\theta| \leq 2\tau \qquad (13)$$

or

$$|\sigma_r - \sigma_z| \leq 2\tau \qquad (14)$$

or

$$|\sigma_z - \sigma_\theta| \leq 2\tau \qquad (15)$$

where all of the inequalities hold for the elastic state but only one or two equalities hold while the material is in the yield state. The selection of the Tresca-Mohr criterion over the commonly used Mises-Hencky criterion is typically based upon the ease to which either criterion may be applied to a specific problem. Both are usually regarded as equally valid and the

24

differences observed are, for the most part, insignificant. Over the past years, the Tresca-Mohr hypothesis has been found to agree reasonably well with experimental evidence and to satisfactorily characterize the yield state. Due to its conceptual simplicity and ease of application to this problem, the Tresca-Mohr condition will be assumed throughout the remainder of this report.

It is necessary to determine which equality (13-15) is applicable for target material in the yield state. The maximum shear stress is half of the difference of the greatest and least principal stresses; the intermediate principal stress does not influence the yield state. An ordering of the three principal stresses, therefore, determines the appropriate equality (13-15). Reference to the equilibrium stress distributions of thick-walled tubes subject to internal pressures sufficient to produce plastic deformation (Allen and Sopwith [99], Bethe [19], Cook [100], Hill, Lee and Tupper [101], Kachanov [102], Nadai [103], etc.) provides, perhaps, insight for the dynamic problem. In all of these references, the radial and circumferential stress distributions are essentially the same but the axial stresses differ according to the assumptions chosen to allow solution. Kachanov notes that the axial stress is half the sum of the radial and circumferential principal stresses for both the elastic state and the pure plastic state of a thin-walled tube. Nadai and subsequently Cook proposed that indeed this relationship should be a very good approximation for the plastic state of a thick-walled cylinder. Hill, et al., using a finite difference technique to solve the boundary value problem of pressure applied on the inner surface and a traction free exterior boundary, found that as plastic flow develops (in terms of increasing deformation), the axial stress approaches the mean of the two other stresses, especially for elements closest to the inside tube surface. Allen and Sopwith, after reviewing the solutions available at their time, compared the independent predictions with particular reference to the exterior boundary expansion and concluded that Cook's approximation of the axial stress relationship leads to only insignificant errors. Additionally, Bethe pointed out that plastic flow in the outer regions has already been assumed to be axially independent, the greatest stress difference is, therefore, $|\sigma_r - \sigma_\theta|$. This is consistent with

Cook's assumption and has been qualitatively confirmed for the dynamic case by the finite difference calculations of Wagner [104]. The equality (13) will then represent the condition of plastic flow:

$$|\sigma_r - \sigma_\theta| = \sigma_y \tag{16}$$

It would be quite convenient at this point that the yield strength, $\sigma_y$, be a material property independent of the strain history, temperature, hydrostatic pressure, etc. Unfortunately, this is not the case for most situations involving impact dynamics. Appendix B gives a brief review of some experiments and modeling efforts concerned with the variation of this yield strength during impact initiated deformation. One of the most obvious dependencies of the yield strength is upon the rate of strain (as several models reflect). Perhaps one of the more widely utilized models, especially within the Russian literature (Agagabian [98], Godunov [105, 106], etc.) is the viscoplastic flow law originally proposed by Hohenemser and Prager [107]. It can be written in the following forms (ex. Prager [108]):

$$\mu \dot{e}_{ij}^{\,p} = \langle F \rangle \frac{\partial F}{\partial \sigma_{ij}} \tag{17}$$

where $\dot{e}_{ij}$ represents the components of the plastic strain rate tensor, $\sigma_{ij}$ is the stress tensor, $\mu$ is the constant coefficient of viscosity and F is the yield function defined as:

$$F = |\sigma_1 - \sigma_2| - \sigma_y$$

and

$$\langle F \rangle = 0 \text{ if } F < 0$$

$$\langle F \rangle = F \text{ if } F \geq 0$$

(18)

where $\sigma_1$ and $\sigma_2$ are the maximum and minimum principal stress components respectively. Following the convention that tensile stresses are positive and recognizing from the equilibrium solutions that $\sigma_\theta > \sigma_r$, the yield function (18) and equation (16) yield:

$$F = \sigma_\theta - \sigma_r - \sigma_y$$

(19)

with this specific yield function, equation (17) reduces to two nonvanishing components of plastic strain rate:

$$\mu \dot{e}_{rr}^P = \sigma_r - \sigma_\theta + \sigma_y$$

(20)

and

$$\mu \dot{e}_{\theta\theta}^P = -(\sigma_r - \sigma_\theta + \sigma_y).$$

(21)

As is typically assumed in incremental plasticity (ex. Fung [109]), the rate of deformation tensor may be decomposed into elastic and plastic components:

$$\dot{e}_{ij} = \dot{e}_{ij}^P + \dot{e}_{ij}^e$$

(22)

and for most problems involving large plastic deformations, which this report subject is certainly one, the elastic contribution is assumed negligible, therefore,

$$\dot{e}_{ij} = \dot{e}_{ij}^P .$$

(23)

The nonzero components of the rate of deformation tensor for plane axisymmetric flow can be written as:

$$\dot{e}_{rr} = \frac{\partial u_r}{\partial r}$$

(24)

$$\dot{e}_{\theta\theta} = \frac{u_r}{r} .$$

(25)

26

Differentiating and substituting equation (8) into equations (24) and (25) and combining the results with equations (23), (20) and (21) yields the following relation:

$$\mu \frac{\dot{\phi}}{r^2} = \sigma_\theta - \sigma_r - \sigma_y \ . \tag{26}$$

Substitution of this equation into equation (11) then produces an expression relating the radial stress gradient and the function $\phi$ (t):

$$\frac{\partial \sigma_r}{\partial r} = \rho \left\{ \frac{\ddot{\phi}(t)}{r} - \frac{\dot{\phi}^2(t)}{r^3} \right\} + \frac{1}{r} \left( \sigma_y + \mu \frac{\dot{\phi}}{r^2} \right) \tag{27}$$

which may be directly integrated with respect to r, between the limits of the radial coordinate, r' (a' $\leq$ r' $\leq$ b) and the elastic/plastic boundary, b.

$$\sigma_r(r') - \sigma_r(b) = \left\{ \rho \ddot{\phi} + \sigma_y \right\} \ln \frac{r'}{b} + \frac{1}{2} \left( \rho \dot{\phi}^2 - \mu \dot{\phi} \right) \left( \frac{1}{r'^2} - \frac{1}{b^2} \right) \cdot \tag{28}$$

The circumferential stress, $\sigma_\theta$, from equation (26) is similarly written:

$$\sigma_\theta(r') = \sigma_y + \sigma_r(b) + \left\{ \rho \ddot{\phi} + \sigma_y \right\} \ln \frac{r'}{b} + \frac{1}{2} \rho \dot{\phi}^2 \left( \frac{1}{r'^2} - \frac{1}{b^2} \right) + \mu \frac{\dot{\phi}}{b^2} \ . \tag{29}$$

The instantaneous stress distribution is thereby determined for time, t', and any position within Region III if the instantaneous position of b(t') and the values $\phi(t')$, $\dot{\phi}(t')$, $\ddot{\phi}(t')$ are known. At this point, $\phi(t)$ remains undetermined.

## D.  The Three Dimensional Plastic Region II

In the introductory portion of this chapter, observations of final target deformations from experimental and numerical investigations were summarized. This region of the target, nearest to the cavity surface, exhibits axial and radial deformation. The degree of deformation is great and it is also expected that the deformation rates are large. Since the irreversible deformations are so much greater than elastic magnitude, plastic behavior should dominate. Glass [64] and Pond [69] experimentally determined the first strain invariant within the region adjacent to cavities in steel targets. Even at the cavity surface, where strains are maximum, the final compression was less than one percent. Similar observations were made by Holloway [30] who considered a much more compressible material, wax. Therefore, in addition to the approximations of axial symmetry and material isotropy, the plastically deforming target material in Region II will be assumed incompressible. Since the deformations are not restricted to axial planes, shear stress and shear flow are likely to some unknown degree in the r-z plane.

The differential equations of motion for axisymmetric flow in Eulerian coordinates may be written:

$$\rho \left\{ \frac{\partial u_r}{\partial t} + u_r \frac{\partial u_r}{\partial r} + u_z \frac{\partial u_r}{\partial z} \right\} = \frac{\partial \sigma_{rr}}{\partial r} + \frac{\sigma_{rr} - \sigma_{\theta\theta}}{r} + \frac{\partial \sigma_{rz}}{\partial z} \tag{30}$$

27

$$\rho \left\{ \frac{\partial u_z}{\partial t} + u_r \frac{\partial u_z}{\partial r} + u_z \frac{\partial u_z}{\partial z} \right\} = \frac{\partial \sigma_{rz}}{\partial r} + \frac{\sigma_{rz}}{r} + \frac{\partial \sigma_{zz}}{\partial z} \qquad (31)$$

$$u_\theta = 0 \qquad (32)$$

where $u_r$, $u_\theta$, and $u_z$ are the instantaneous components of velocity, $\rho$ is the target density and $\sigma_{ij}$ are the nonzero components of the instantaneous stress tensor. The incompressible continuity equation is:

$$\frac{\partial u_r}{\partial r} + \frac{u_r}{r} + \frac{\partial u_z}{\partial z} = 0 . \qquad (33)$$

The system of nonlinear partial differential equations (30 – 33) is indeterminate. Either additional independent equations must be supplied or assumptions that reduce the number of dependent variables must be imposed in order to obtain solutions. Most contemporary finite difference approaches utilize the former method. The incompressibility condition is relaxed, an energy conservation equation is formulated, constitutive equations are assumed and the resulting more complex system of nonlinear partial differential equations are approximated with a set of algebraic difference equations which are then solved on the computer in a variety of ways. Alder [110] describes some of these and presents examples of their relative accuracies. Unfortunately, this general approach is not without difficulties. In addition to the errors introduced by the differencing approximation, the formulation of the energy equation, the choice of the most appropriate constitutive model and the treatment of boundary conditions and shock singularities all involve varying degrees of approximation. Cost is often a limitation, especially when high resolution and minimal errors are desired. The alternate approach to the solution of the system of field equations is to reduce the original set (30–33) to simpler analytic form by suitable approximations. These simplifications should be supported by experimental evidence or theoretical argument.

The experiments of Glass [64], Moss [111] and Pond [34, 69] utilized some metallographic techniques to study the deformation fields of the target near hypervelocity impact cavities. While Pond and Glass embedded markers in the undeformed target to trace point displacements, Moss recognized that the microstructure typical of quenched and tempered, hardenable, low-carbon steel plate could serve as a reference grid from which shear strains can be calculated. Bands of plane chemical inhomogeneities that had been spread through the plate as it was rolled from an ingot are initially parallel with the top and bottom surfaces of the target plate. These reference bands are deformed as the penetrator perforates a given axial plane. Measurements of the slopes of the reference bands then determine the shear strain distribution. Moss investigated the nature of adiabatic shear bands by shear plugging plates with explosively driven punches. He estimates the shear strain rates and temperatures within these extremely small regions (on the order of $10^{-3}$ cm) which run orthogonal to the metallographic reference bands. Immediately adjacent to these shear bands is a region which resembles the deformation fields observed by Weihrauch [72] and Johnson [67] and calculated by Kucher [56]. The process of shear plugging is considerably different from long rod penetration. Consequently, an experiment was proposed and performed

28

utilizing the metallographic technique of Moss, but applied to the steady, deep penetration problem. Figure 10 shows the experimental configuration designed to exhibit the deformation field in Region II.
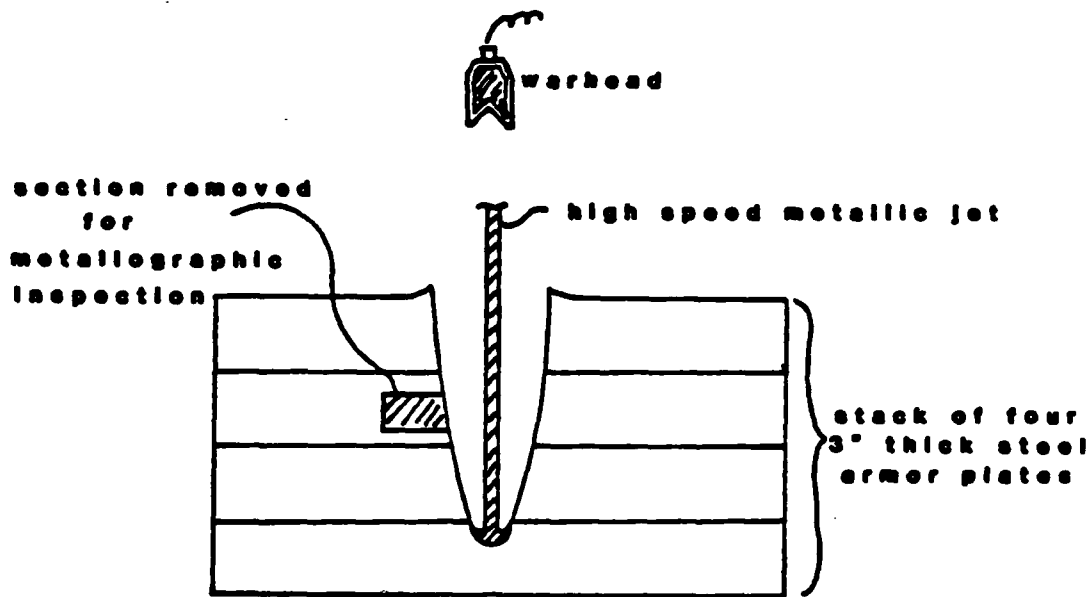


Figure 10. Test Configuration for the Observation of the Final
Deformation Field

The detonation of a shaped charge device produces an axially aligned, continuous, metallic jet with a velocity range typically between 2-8 km/s. The top target plate was located close enough to the warhead so that the jet penetrated the target in a continuous state (at great distances the jet particulates due to the inherent axial velocity gradient). The warhead was selected so that the target would be completely penetrated. According to Christman [23], upon initial impact with the top surface, the jet begins the transient penetration phase which quickly disappears and then enters the primary or quasi-steady penetration mode as described in Appendix A. After the event was completed, the perforated plates were recovered and inspected. Plate number two was selected for further study since it involved only the quasi-steady phase and the jet would still be completely continuous at this distance. This plate was then sawed in two along the axis of the hole, a section (see Figure 10) was removed, polished and macroetched with Oberhoeffer's etch. Figure 11 includes a sketch and photograph of the exposed banded structure after the penetration event, as observed under the microscope. The fibrous-like banded structure of alternating layers of ferrite and pearlite originally aligned along axial planes, deforms into directions parallel to the penetration trajectory near the cavity surface. The surfaces appear practically parallel to each other, especially as the distance from the cavity increases. The shear strain, $\gamma_{rz}$, is defined as:
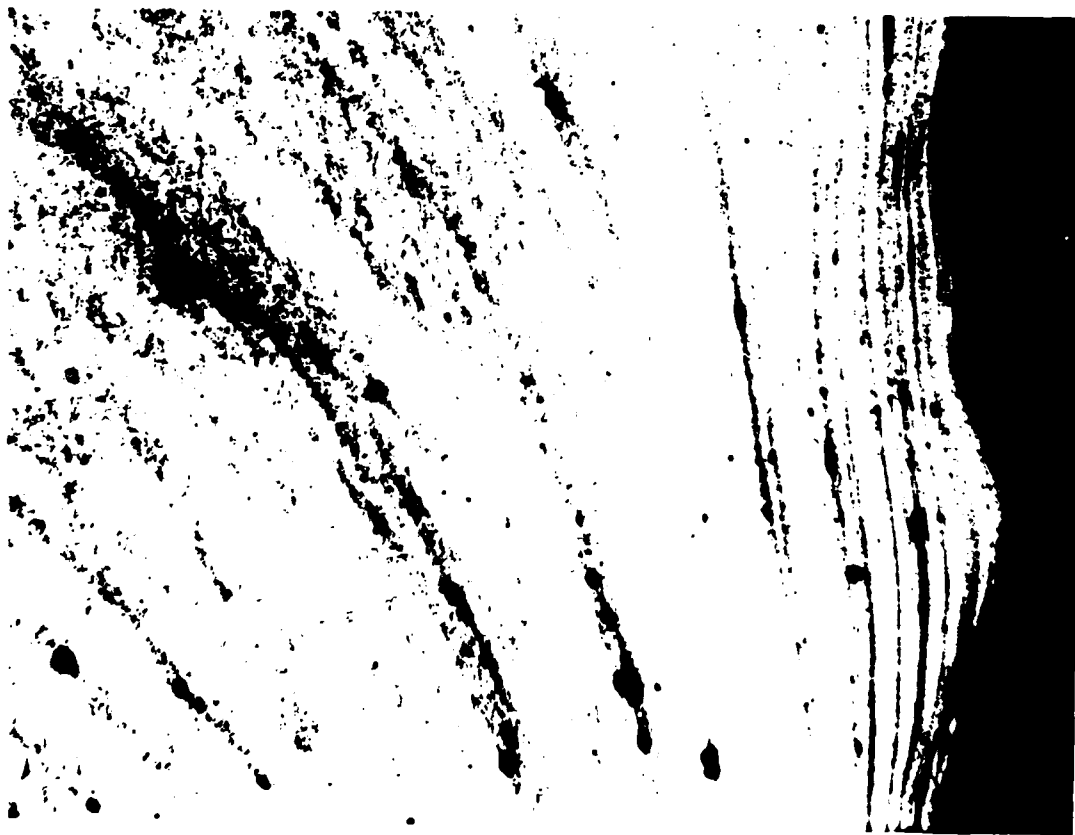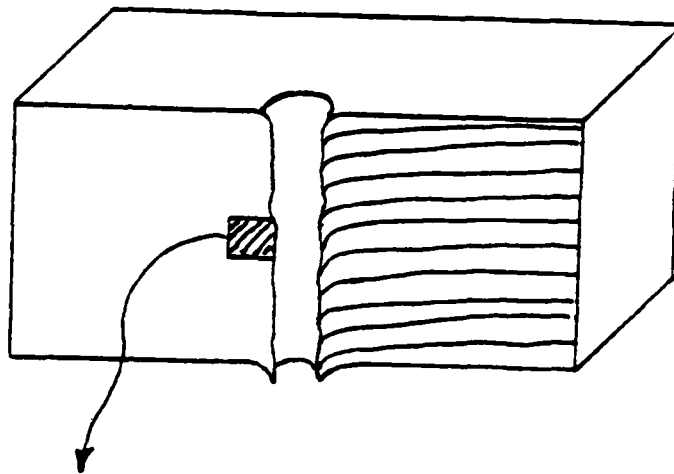
Figure 11. Sketch and Photograph of the Banded Structure Exposed
by Etching in Plate Two, After Penetration by a Metallic Jet, 50X

$$\gamma_{rz} = \frac{1}{2} \left( \frac{\partial \bar{u}_z}{\partial r} + \frac{\partial \bar{u}_z}{\partial z} \right) \tag{34}$$

where $\bar{u}_r$ and $\bar{u}_z$ represent the final displacements. If stretching in the axial direction is neglected (pure shear deformation in the r-z plane) then the axial gradient vanishes and equation (34) reduces to a relationship between the shear strain and the measured deflection angle, $\theta_1$:

$$\gamma_{rz} = \frac{1}{2} \frac{\partial u_z}{\partial r} = \frac{1}{2} \tan \theta_1 . \tag{35}$$

Several reference bands were selected for different axial planes through the thickness of plate number two. Deflection angles were measured along each of these bands for radial positions close to the cavity surface. Figure 12 gives the calculated shear strain distribution with respect to the radial coordinate. All of the reference bands yield distributions that fall within the shaded region, decay to negligible magnitudes at about the same radial coordinate, and exhibit no consistent variation with respect to axial position.

The observation of these reference band surfaces as well as the experimental evidence of Weihrauch [72] and the numerical calculations of Kucher [56] all suggest the assumption of parallel flow. The axial gradients of displacements and velocities, therefore, vanish in Region II. The approximation does not require that either the shear stress, $\sigma_{rz}$, or shear strain, $\gamma_{rz}$ equal zero, although they vanish by definition in Regions III and IV. Equations (30-33) simplify to:

$$\rho \left\{ \frac{\partial u_r}{\partial t} + u_r \frac{\partial u_r}{\partial r} \right\} = \frac{\partial \sigma_{rr}}{\partial r} + \frac{\sigma_{rr} - \sigma_{\theta\theta}}{r} + \frac{\partial \sigma_{zr}}{\partial z} \tag{36}$$

$$\rho \left\{ \frac{\partial u_z}{\partial t} + u_r \frac{\partial u_z}{\partial r} \right\} = \frac{\partial \sigma_{zr}}{\partial r} + \frac{\sigma_{zr}}{r} + \frac{\partial \sigma_{zz}}{\partial z} \tag{37}$$

$$\frac{\partial u_r}{\partial r} + \frac{u_r}{r} = 0 . \tag{38}$$

Equation (38) is identical to the incompressible continuity equation applicable to the plane deformation Region III. The radial velocity is, therefore:

$$u_r = \frac{f(z,t)}{r} \tag{39}$$

but the parallel flow restriction eliminates the axial dependence and the radial velocity then has identical form as in Region III:

$$u_r = \frac{\dot{\phi}(t)}{r} \tag{40}$$

31

where $\dot{\phi}(t)$ is an arbitrary, differentiable function of time. Equation (36) includes the axial gradient of the shear stress, $\sigma_{zr}$. This shear stress is given for the case of a Newtonian flow (which is perhaps appropriate in this region where deformations and rates are greatest):

$$\sigma_{zr} = \mu\left(\frac{\partial u_r}{\partial z} + \frac{\partial u_z}{\partial r}\right) \tag{41}$$

where $\mu$ is the viscosity coefficient as described in the formulation of the viscoplastic flow of Region III. The assumption of parallel flow once again eliminates the axial gradient of the radial velocity and upon differentiation with respect to z, equation (41) becomes:

$$\frac{\partial \sigma_{zr}}{\partial z} = \frac{\partial}{\partial z}\mu\frac{\partial u_z}{\partial r} . \tag{42}$$

The axial velocity field is assumed to be piece-wise continuous, thereby allowing the interchange of the partial derivatives and therefore:

$$\frac{\partial \sigma_{zr}}{\partial z} = \mu\frac{\partial}{\partial r}\frac{\partial u_z}{\partial z} = 0 . \tag{43}$$

Combining equations (36), (37), (40), (41) and (43) yields:

$$\rho\left\{\frac{\ddot{\phi}}{r} - \frac{\dot{\phi}^2}{r^3}\right\} = \frac{\partial \sigma_{rr}}{\partial r} + \frac{\sigma_{rr}-\sigma_{\theta\theta}}{r} \tag{44}$$

$$\rho\left\{\frac{\partial u_z}{\partial t} + \frac{\dot{\phi}}{r}\frac{\partial u_z}{\partial r}\right\} = \mu\left\{\frac{\partial^2 u_z}{\partial r^2} + \frac{1}{r}\frac{\partial u_z}{\partial r}\right\} + \frac{\partial \sigma_{zz}}{\partial z} \tag{45}$$

where because the shear stress, $\sigma_{zr}$, is not necessarily zero, the stresses $\sigma_{rr}$, $\sigma_{\theta\theta}$ and $\sigma_{zz}$ are not principal. The axial velocity distribution ($U_z(r,t)$) is undefined at this point, but does not appear explicitly in equation (44). With the exception that the stresses are not exactly principal, equation (44) has the identical form of the radial equation of motion developed in Region III. The stresses in Region III are principally due to the assumption of plane deformation. The Tresca yield condition and the Bingham-like flow rule of Hohenemser and Prager [107] were selected because of their analytic simplicity and because they accurately model behavior of metal deformations typical of impact and penetration problems (see Appendix B). In order to continue the formulation of Region II along the same approach as in Region III, the relative magnitudes of the stress components must be discerned.

Equation (41) suggests that the plastically flowing target material behaves much like a viscous fluid. The solid nature of the target has been implicitly assumed negligible in comparison with the viscous stresses that develop because of the very large deformation rates within this region. Suppose that the stress tensor may be described in more general form by:

32

$$\sigma_{ij} = \sigma_{ij}^{\ \ o} + \mu \left( \frac{\partial u_i}{\partial x_j} + \frac{\partial u_j}{\partial x_i} \right) + \lambda_o \frac{\partial u_k}{\partial x_k} \delta_{ij} \qquad (46)$$

where $\mu$ and $\lambda_o$ represent the conventional fluid viscosity coefficients, $\sigma_{ij}^{\ \ o}$ represents the rate independent components of the solid stress tensor and $x_i$ are the cylindrical coordinates. Incompressibility ($\partial U_k / \partial X_k = 0$), axial symmetry $\left( \frac{\partial}{\partial \theta}, U_\theta = 0 \right)$ and parallel flow ($\partial U_r / \partial_z = \partial U_z / \partial_z = 0$) simplify equation (46) to:

$$
\begin{array}{ll}
\sigma_{rr} = \sigma_{rr}^{\ \ 0} + 2\mu \dfrac{\partial u_r}{\partial r} & \sigma_{rz} = \sigma_{rz}^{\ \ o} + \mu \dfrac{\partial u_z}{\partial r} \\[2ex]
\sigma_{\theta\theta} = \sigma_{\theta\theta}^{\ \ o} + 2\mu \dfrac{u_r}{r} & \sigma_{r\theta} = 0 \\[2ex]
\sigma_{zz} = \sigma_{zz}^{\ \ o} & \sigma_{\theta z} = 0
\end{array}
\qquad (47)
$$

Utilizing equation (40), the nonzero components can be written:

$$
\begin{array}{ll}
\sigma_{rr} = \sigma_{rr}^{\ \ o} - 2\mu \dfrac{\dot{\phi}}{r^2} & \sigma_{rz} = \sigma_{rz}^{\ \ o} + \mu \dfrac{\partial u_z}{\partial r} \\[2ex]
\sigma_{\theta\theta} = \sigma_{\theta\theta}^{\ \ o} + 2\mu \dfrac{\dot{\phi}}{r^2} & \sigma_{zz} = \sigma_{zz}^{\ \ o}
\end{array}
\qquad (48)
$$

and further assuming that the rate dependent contributions predominate over the static terms during the time when rates of deformation are great, the components are approximately given as:

$$
\begin{array}{ll}
\sigma_{rr} = -2\mu \dfrac{\dot{\phi}}{r^2} & \sigma_{rz} = \mu \dfrac{\partial u_z}{\partial r} \\[2ex]
\sigma_{\theta\theta} = 2\mu \dfrac{\dot{\phi}}{r^2} & \sigma_{zz} = 0
\end{array}
\qquad (49)
$$

33

The maximum possible shear stresses can be deduced from the relations of Mohr for different plane systems:

$$\text{(r-z planes)}, \quad \tau_{rz} = \left\{\left(\frac{\sigma_{rr}}{2}\right)^2 + \sigma_{rz}^2\right\}^{1/2} = \mu\left\{\frac{\dot{\phi}^2}{r^4} + \left(\frac{\partial u_z}{\partial r}\right)^2\right\}^{1/2} \tag{50}$$

$$\text{(r-$\theta$ planes)}, \quad \tau_{r\theta} = \frac{1}{2}\left\{\sigma_{rr} - \sigma_{\theta\theta}\right\} = 2\mu\frac{\dot{\phi}}{r^2} \tag{51}$$

$$\text{($\theta$-z planes)}, \quad \tau_{\theta z} = \frac{1}{2}\left\{2\mu\frac{\dot{\phi}}{r^2}\right\} = \mu\frac{\dot{\phi}}{r^2} . \tag{52}$$

Depending on the magnitude of the radial gradient of the axial velocity, the maximum shear stress appears upon either axial (r-$\theta$) planes or planes including the symmetry axis (r-z). If it is assumed that the shear strain at any coordinate develops continuously over the time interval dt during which incremental deformations occur, the shear strain rate is then related to the shear strain by:

$$\dot{\gamma}_{rz} = \frac{\partial u_z}{\partial r} = \frac{d}{dt}\left(\frac{\partial \overline{U}_z}{\partial r}\right) \tag{53}$$

or in other words, the velocity and deformation gradients possess identical spatial functional forms. Figure 12 exhibits an observed shear strain distribution. The shear strain rate may be approximated with:

$$\frac{\partial u_z}{\partial r} = \hat{K} \exp\left\{-\lambda_1 (r-a)\right\} \tag{54}$$

where $\hat{K}$, the maximum possible shear rate, can be estimated by the presumption of slip at the target cavity when the shear strength of the target is exceeded.

$$\hat{K} = \frac{\partial u_z}{\partial r} = \frac{\sigma_y}{2\mu} . \tag{55}$$

The term $\dot{\phi}/r^2$ represents $u_r/r$. Within Region II, the radii are small (relative to the target dimension) and the radial velocities are maximum. Therefore, it will be assumed that throughout Region II that $\dot{\phi}/r^2 > \partial u_z/\partial r$ and $\tau_{z\theta} < \tau_{rz} < \tau_{r\theta}$. Assuming this to be the case, then the greatest shear stress is likely upon axial (r-$\theta$) planes. If, however, the radial gradient of axial velocity is of the same order as $\dot{\phi}/r^2$ then, shear deformation is equally likely upon both (r-z) and (r-$\theta$) planes.

34
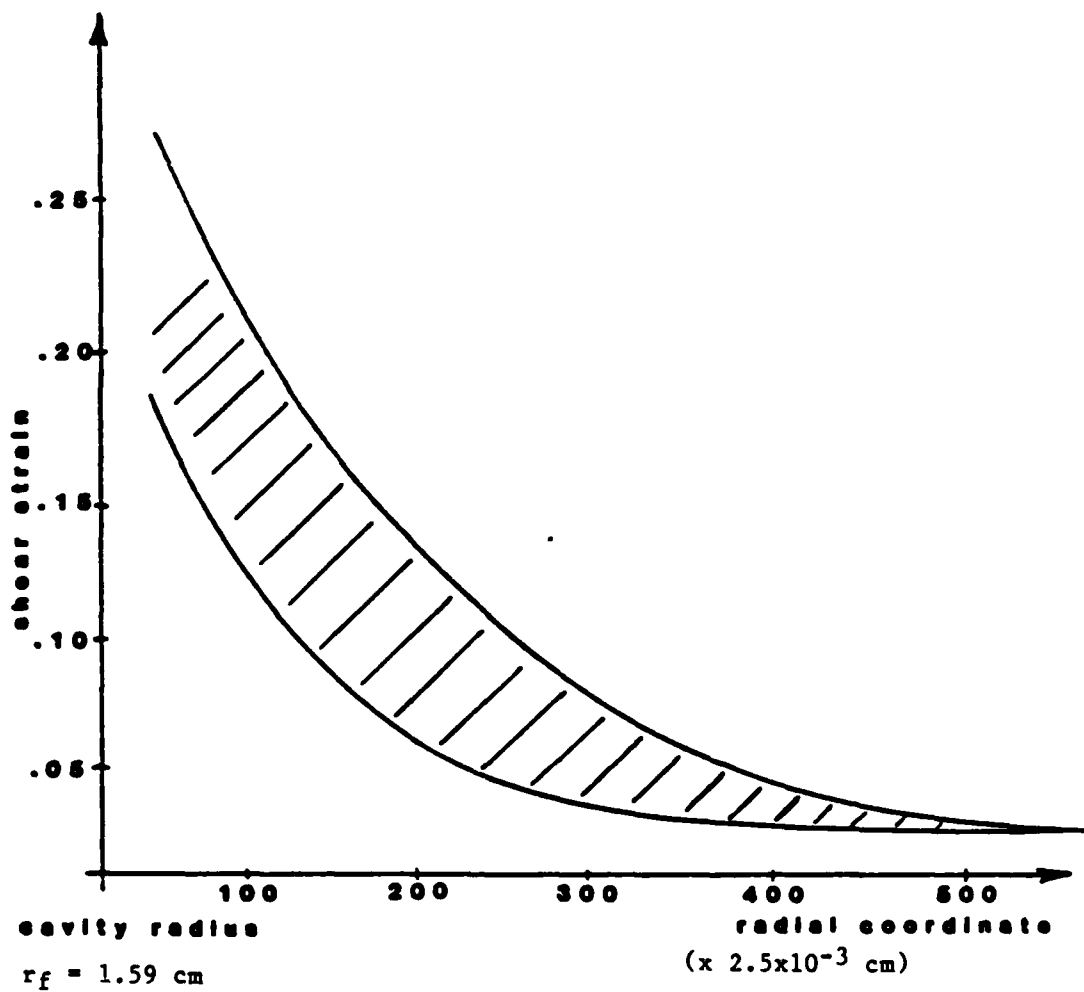
Figure 12. The Experimentally Measured Shear Strain Distribution

The Tresca yield criterion was applied within the formulation of Region III. The criterion considers the differences of the principal stresses, and as already noted, the hoop and radial stresses in Region II are not necessarily principal. They are principal if the radial gradient of axial velocity is completely negligible. However, the results depicted in Figure 12 and the argument leading to equation (54) suggest that this is not the case.

If the gradient term is of the same order as $\dot{\phi}/r^2$ everywhere within this region (actually this is perhaps a worst case situation) then the principal stress state will be different in general from the actual stress state. As a measure of how different, let

$$\frac{\partial u_z}{\partial r} = \frac{\dot{\phi}}{r^2} .$$

(56)

The approximate viscous stress state, equations (49) with equation (56) are related to the principal stress state, $S_i$, by the following relationship:

$$\begin{vmatrix} -2-s & 0 & 1 \\ 0 & 2-s & 0 \\ 1 & 0 & -s \end{vmatrix} \quad \mu \frac{\dot{\phi}}{r^2} = 0 .$$

(57)

The solution to the resulting cubic, algebraic equation yields three real, distinct roots that represent the components of the principal stress vector. The components are:

$$s_1 = +2.0\mu \frac{\dot{\phi}}{r^2}$$

$$s_2 = +0.41\mu \frac{\dot{\phi}}{r^2}$$

(58)

$$s_3 = -2.41\mu \frac{\dot{\phi}}{r^2} .$$

The largest difference between any two principal stress components is:

$$|s_1-s_3| = 4.4\mu \frac{\dot{\phi}}{r^2} .$$

(59)

The difference between the radial and circumferential stresses is:

$$|\sigma_{rr}-\sigma_{\theta\theta}| = 4.0\mu \frac{\dot{\phi}}{r^2} .$$

(60)

36

Accepting the approximate stress state (49) and estimating the shear strain rate ($\partial u_z/\partial r$) from experimental measurement ($\partial \overline{U}_z/\partial r$) yields the observation that expressions (59) and (60) are not significantly different. They differ on the order of ten percent or less depending upon the relative magnitude of the shear strain rate. In Region III, the principal and general stress states are identical by definition ($\partial \overline{U}_z/\partial r = \partial u_z/\partial r = 0$). In Region II, however, the axial deformation is nonzero but as just mentioned, the distinction between the expressions (59) and (60) is perhaps not significant for practical purposes. Radial flow is likely to predominate in both regions. This statement is once again supported by experimental and numerical evidence (Glass [64], Pond [69], Wagner [104], etc.). It should also be noted that the yield strength, presumed in the yield criterion, of target materials subject to ballistic impact is only crudely known. The errors associated with the estimation of a precise value most likely exceed any error introduced by the equivalencing of the principal and general stress vectors. With this in mind, the stress difference term in equation (44) will be approximated with a principal stress difference and subsequently the Tresca yield criterion and the Hohenemser-Prager flow rule will be applied in the same manner as in Region III. The resulting radial and circumferential stress distributions in Region II are:

$$\sigma_{rr}(r) = \sigma_{rr}(a) + \left\{\rho\ddot{\phi}+\sigma_y\right\} \ln \frac{r}{a} + \frac{1}{2}\left(\rho\dot{\phi}^2-\mu\dot{\phi}\right)\left(\frac{1}{r^2} - \frac{1}{a^2}\right) \tag{61}$$

$$\sigma_{\theta\theta}(r) = \sigma_{rr}(r) + \sigma_y + \mu \frac{\dot{\phi}}{r^2} \tag{62}$$

for $a \leq r \leq a'$.

The static contributions of the general stress tensor are assumed negligible since the deformation rates and viscous stress components are estimated as large. The assumption of parallel flow eliminates the axial gradients of the velocity. The axial stress component is, therefore, negligible. The shear stress component, $\sigma_{zr}$, is however, finite and is related to the axial velocity distribution by:

$$\sigma_{zr} = \mu \frac{\partial u_z}{\partial r} \tag{63}$$

where the gradient term may have the same form as the experimentally observed shear strain distribution. In order to more precisely determine the axial velocity distribution, equation (45) is recalled and the axial gradient of the axial stress is ignored:

$$\rho \left\{\frac{\partial u_z}{\partial t} + \frac{\dot{\phi}}{r} \frac{\partial u_z}{\partial r}\right\} = \mu \left\{\frac{\partial^2 u_z}{\partial r^2} + \frac{1}{r} \frac{\partial u_z}{\partial r}\right\}. \tag{64}$$

Equation (54) crudely estimates the radial gradient of the axial velocity distribution to be of exponential form, with a decay coefficient, $\lambda_1$ and maximum shear rate, $\hat{K}$. The radial derivative of this distribution will also be of the same exponential form. It is assumed that the last term in equation (64) will dominate the right-hand side of the equation and, therefore, equation (64) is approximated as:

$$\frac{\partial u_z}{\partial t} = \frac{1}{r} \frac{\partial u_z}{\partial r} \left\{ \frac{\mu}{\rho} - \dot{\phi}(t) \right\} \cdot \tag{65}$$

Providing that $\dot{\phi}(t)$ is independently determined, equation (65) is separable and can be solved with standard methods. Its solution is given in Appendix C. With this distribution in hand, the complete but approximate stress distribution is specified in terms of the undetermined differentiable function, $\dot{\phi}(t)$.

## E.  The Rod Inversion Region I

The steady penetration theory, as described in Appendix A, presumed that the penetrator/target interaction surface moves along the symmetry axis with constant velocity, U.  If a coordinate frame of reference is attached to the intersection point of this surface with the symmetry axis (stagnation point), then penetrator material approaches this point with a relative velocity, $S = V - U$, where V is the penetrator velocity in the laboratory frame and target material approaches from the opposite direction with a relative velocity, U.  In this translating coordinate frame, the axial penetration process appears steady.  The interaction surface has a characteristic mushroom shape that remains constant throughout the steady penetration process.  Figure 13 is a schematic description of this surface along with a hypothesized control volume, c.
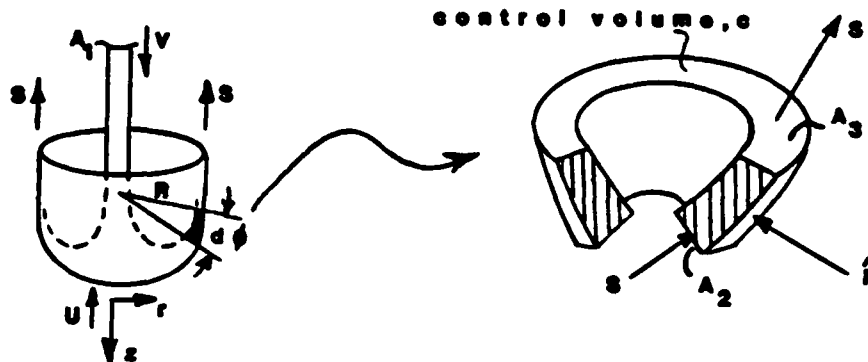


Figure 13.  The Penetrator Interaction Surface and
Control Volume, c

The penetrator, characterized by its circular cross section, $A_1$, density, $\rho_p$, and velocity, V, upon reaching the stagnation region, inverts and flows along the expanding target cavity, through the incremental control volume, c. As in the plastic deformation regions of the target, incompressibility is assumed, material enters the control volume through surface, $A_2$, and exits the control volume through $A_3$.  Assuming that the flow is steady (no acceleration) during the angular deflection, $d\phi$, the target must supply a force $\hat{F}$, determined by the relation:

38

$$\hat{F} = \int_{c.s.} \vec{\bar{s}} \, \rho_p \, \vec{\bar{s}} \, d\hat{A} \tag{66}$$

which is a statement of the conservation of linear momentum. The inner surface may be interpreted as a free stream surface, upon which the pressure is zero and from Bernoulli's equation, the speed $|\vec{\bar{s}}|$ must be constant. If mass flows through surfaces, $A_1$, $A_2$ and $A_3$ only and the flow velocity, S is uniform over each of these, then the incompressible continuity equation requires that:

$$\rho_p |\vec{\bar{s}}| A_1 = \rho_p |\vec{\bar{s}}| A_2 = \rho_p |\vec{\bar{s}}| A_3 = \text{constant} \tag{67}$$

and, therefore, equation (66) becomes:

$$\hat{F} = \rho_p |\vec{\bar{s}}|^2 A_1 \sin d\emptyset \cdot \tag{68}$$

Cross section, $A_1$, is given by $\pi r_p^2$, where $r_p$ is the penetrator radius. The pressure within this incremental control volume may be estimated as the force acting upon the outer surface over the area of this outer surface:

$$P = \frac{\hat{F}}{2\pi r R d\emptyset} \tag{69}$$

where R is the radius of curvature of the outer surface, $d\emptyset$ is the angular deviation of the velocity vector $\vec{\bar{s}}$ and r is the radial position of the midpoint of the outer surface. Substituting equation (68) into (69) yields:

$$P = \frac{1}{2} \rho_p \frac{r_p^2 |\vec{\bar{s}}|^2 \sin d\emptyset}{r R d\emptyset} \tag{70}$$

where for small deflection angles, $d\emptyset = \sin d\emptyset$ and then

$$P = \rho_p \, r_p^2 \frac{|\vec{\bar{s}}|^2}{2rR} \cdot \tag{71}$$

The steady penetration theory requires stress continuity at the stagnation point, thereby relating $|\vec{\bar{s}}|$ and U:

$$\rho_p |s|^2 = \rho U^2 \tag{72}$$

where $\rho$ is the target density. Equation (71) may then be alternatively written:

$$P = \rho r_p^2 \frac{U^2}{2rR} \cdot \tag{73}$$

From differential geometry, the radius of curvature is related to the instantaneous surface slope and its derivative:

39

$$\frac{1}{R} = \frac{\left|\frac{d^2z}{dr^2}\right|}{\left[1 + \left(\frac{dz}{dr}\right)^2\right]^{3/2}} . \tag{74}$$

In order to evaluate the terms $dz/dr$ and $d^2z/dr^2$, the steady penetration theory is once again recalled. The time rate of change of the axial position of the stagnation point is defined as:

$$\frac{dz}{dt} = U = \frac{V}{1 + \sqrt{\rho/\rho_p}} . \tag{75}$$

If $z = z(t(r))$ where $t(r)$ has a unique inverse, $r(t)$ and $dr/dt \neq 0$, then:

$$\frac{dz}{dr} = \frac{dz}{dt}\frac{dt}{dr} = U\frac{dt}{dr} \tag{76}$$

$$\frac{d^2z}{dr^2} = \frac{d}{dr}\left(U\frac{dt}{dr}\right) = U\frac{d^2t}{dr^2} .$$

The inverse functions are given by the rules of differentiation,

$$\frac{dt}{dr} = \left\{\frac{dr}{dt}\right\}^{-1}$$

$$\frac{d^2t}{dr^2} = \frac{-\frac{d^2r}{dt^2}}{\left(\frac{dr}{dt}\right)^3} \tag{77}$$

and when combined with equation (76) and written in more compact form yield:

$$\frac{dz}{dr} = \frac{U}{\dot{r}}$$

and $\tag{78}$

$$\frac{d^2z}{dr^2} = \frac{-U\ddot{r}}{\dot{r}^3} .$$

Substituting expressions (78) into equation (73) then couples the pressure in the incremental control volume with the kinematic properties of the outer surface $(r, \dot{r}, \ddot{r})$ at any particular time, upon any axial plane:

$$P(t) = \rho r_p^2 U^3 \left\{ \frac{|-\ddot{r}|}{r\dot{r}^3\left(1 + \frac{U^2}{\dot{r}^2}\right)^{3/2}} \right\} . \tag{79}$$

In other words, if the radial acceleration process of the target cavity relative to a fixed axial plane is known a priori, then the time variation of the pressure in the penetrator at the axial coordinate can be determined. However, it is this acceleration process that is the desired solution, thereby suggesting the coupling between Regions I and II.

## F. The Boundary Coupling of Regions I-IV Yielding the Governing Differential Equations

As noted in Section IIA, the problem is divided into separate regions of different deformation behaviors to allow an analytic formulation. The formulation of Region I produces a relationship between the pressure within the reversed flow penetrator and flow properties of a point of intersection of the penetrator interaction surface and a particular axial plane. Regions II, III and IV yield the stress distributions on constant z planes as a function of radial position and the function $\phi(t)$. Regions III and IV presume negligible axial deformations while Region II, obeying the parallel flow constraint, allows for axial velocity, axial displacement and shear stress in the r-z plane. Before the stress distributions can be quantitatively described, the function $\phi(t)$ must be determined. Indeed, once this function is known, then the displacement and velocity fields as well as the stress fields will be determined.

In order to determine the function $\phi(t)$, the radial stress equations in Regions II, III and IV will be utilized. The boundaries, whether real or imaginary, separate these Regions. From the continuity equation applicable for the plastic flow Regions, the relation for the radial velocity is:

$$U_r = \frac{\dot{\phi}(t)}{r} . \tag{80}$$

If the velocity of a particle at position r, at time t is expressed as dr/dt, then upon integration of equation (80), the position of a particle originally located at $r_o$ is given by:

$$r = \left[ r_o^2 + 2\phi(t) \right]^{1/2} \tag{81}$$

for any time t. This expression may be twice differentiated to obtain the acceleration at a given radial position and time:

$$\ddot{r} = \frac{\ddot{\phi}}{r} - \frac{\dot{\phi}^2}{r^3} . \tag{82}$$

The positions of the boundaries may be similarly described:

$$a(t) = \left[ a_o^2 + 2\phi(t) \right]^{1/2}$$

$$a'(t) = \left[ a_o'^2 + 2\phi(t) \right]^{1/2} \tag{83}$$

$$b(t) = \left[ b_o^2 + 2\phi(t) \right]^{1/2} .$$

The outer boundary, c(t) can be considered constant if the target is assumed semi-infinite, i.e.:

$$c(t) = \left[ c_o^2 + 2\phi(t) \right]^{1/2} \tag{84}$$

but $|c_o^2| \gg |\phi|$, so

$$c(t) \approx c_o .$$

41

If the lateral dimension is finite and the outer boundary is likely to permanently deform, then the elastic Region IV vanishes and a traction free boundary condition can be applied directly to b(t).

The magnitude of the penetration rate determines the nature of the matching conditions at these boundaries. As noted in the introduction, framing camera experiments involving optically transparent materials suggest that shock waves are likely if the penetration rate equals or exceeds the local sound speed of the target. If the penetration is "subsonic," shock waves are less likely and the stress and velocity distributions are then continuous across the boundaries. This has been both experimentally and numerically confirmed. Pritchard [70] considered subsonic conditions and made measurements at gage locations on the penetration trajectory. He found that as the penetrator interface approached the gage, the stress and strain field increased rapidly (but continuously) from zero to the stagnation value without any evidence of shock discontinuities. The computational work of Wagner [104] recognizes the same behavior, even during the initial transient phase. For most conventional armor applications, the sound speed in metallic target materials is typically greater than the penetration rates of both kinetic energy penetrators and shaped-charge jets. For these situations, stress as well as velocity continuity will be enforced.

The radial stress variation is identical in both Regions II and III. Stress continuity at boundary, a', then allows these two Regions to be considered as one. This combined plastic Region then has an inner boundary, a, and an elastic/plastic outer boundary, b (for the semi-infinite problem). The radial stress at any radial position r, $a \leq r \leq b$ is then given by equation (61) of Region II:

$$\sigma_{rr}(r) - \sigma_{rr}(a) = \left\{\rho\ddot{\emptyset} + \sigma_y\right\} \ln \frac{r}{a} + \frac{1}{2}\left\{\rho\dot{\emptyset}^2 - \mu\dot{\emptyset}\right\}\left(\frac{1}{r^2} - \frac{1}{a^2}\right). \quad (85)$$

The condition of stress continuity on the inner boundary is:

$$\sigma_{rr}(a) = -P(t) \quad (86)$$

where P(t) is determined from the control volume analysis of Region I. Combining (86), (85), (83) and equation (79) of Region I yields:

$$\sigma_{rr}(r) = \left\{\rho\ddot{\emptyset} + \sigma_y\right\} \ln \left[\frac{r_o^2 + 2\emptyset}{a_o^2 + 2\emptyset}\right]^{1/2} + \frac{1}{2}\left\{\rho\dot{\emptyset}^2 - \mu\dot{\emptyset}\right\}\left(\frac{1}{r_o^2+2\emptyset} - \frac{1}{a_o^2+2\emptyset}\right) \quad (87)$$

where

$$P(t) = \frac{1}{2}\rho r_p^2 U^3 \left\{\frac{\left|\ddot{\emptyset}\left(a_o^2 + 2\emptyset\right)^{1/2} - \dot{\emptyset}^2\left(a_o^2 + 2\emptyset\right)^{-1/2}\right|}{\dot{\emptyset}^3\left(1 + \frac{u^2\left(a_o^2 + 2\emptyset\right)}{\dot{\emptyset}^2}\right)^{3/2}}\right\}.$$

$\emptyset(t)$ is the undetermined function of time, $r_o$ and $a_o$ the initial radial positions of the point $r(t)$ and the cavity wall respectively. If the stress, $\sigma_{rr}(r)$, is known at a point $r$ for all time, then equation (87) becomes a second order nonlinear ordinary differential equation in $\emptyset(t)$. Three cases in which this stress boundary condition can be determined are now considered.

The first case involves penetration into metallic cylinders of small radial dimension. The penetration process is subsonic; stress and velocity continuity is assumed throughout and the lateral target boundary is unconstrained. This situation suggests both the neglect of the elastic region altogether and the traction-free condition on the outer boundary. Given $\sigma_{rr}(b) = 0$, for all time, equation (87) then becomes:

$$\{\rho\ddot{\emptyset} + \sigma_y\} \ln \left[\frac{a_o^2 + 2\emptyset}{b_o^2 + 2\emptyset}\right]^{1/2} + \frac{1}{2}\left\{\rho\dot{\emptyset}^2 - \mu\dot{\emptyset}\right\}\left(\frac{1}{a_o^2+2\emptyset} - \frac{1}{b_o^2+2\emptyset}\right)$$

$$+ \frac{1}{2}\rho r_p^2 U^3 \left\{\frac{\left|\ddot{\emptyset}\left(a_o^2 + 2\emptyset\right)^{1/2} - \dot{\emptyset}^2\left(a_o^2 + 2\emptyset\right)^{-1/2}\right|}{\dot{\emptyset}^3\left(1 + \frac{U^2\left(a_o^2 + 2\emptyset\right)}{\dot{\emptyset}^2}\right)^{3/2}}\right\} = 0 \; . \tag{88}$$

The second case involves the penetration into very massive metallic targets. The penetration process is subsonic; stress and velocity continuity is assumed, but the target is semi-infinite or of very large lateral dimension. An elastic region bounds the plastic deformation region. Stress continuity at the elastic/plastic boundary, $b(t)$ requires that:

$$\sigma_{rr_p}(b) = \sigma_{rr_e}(b) \quad \text{(for all time).} \tag{89}$$

Recalling the Hohenemser-Prager flow condition (equation (26) Section III), applied to the elastic boundary point, $b$,

$$|\sigma_{\theta\theta} - \sigma_{rr}| = \sigma_y + \mu \frac{\dot{\emptyset}}{b^2} \tag{90}$$

and remembering that in the elastic region, $\sigma_{\theta\theta}(r) = -\sigma_{rr}(r)$, then

$$\sigma_{rr}(b) = \frac{1}{2}\left(\sigma_y + \mu \frac{\dot{\emptyset}}{b^2}\right). \tag{91}$$

Equation (87) then becomes:

$$\{\rho\ddot{\emptyset} + \sigma_y\} \ln \left[\frac{a_o^2 + 2\emptyset}{b_o^2 + 2\emptyset}\right]^{1/2} + \frac{1}{2}\left\{\rho\dot{\emptyset}^2 - \mu\dot{\emptyset}\right\}\left(\frac{1}{a_o^2+2\emptyset} - \frac{1}{b_o^2+2\emptyset}\right) +$$

$$\frac{1}{2}\rho r_p^2 U^3 \left\{\frac{\left|\ddot{\emptyset}\left(a_o^2 + 2\emptyset\right)^{1/2} - \dot{\emptyset}^2\left(a_o^2 + 2\emptyset\right)^{-1/2}\right|}{\dot{\emptyset}^3\left(1 + \frac{U^2\left(a_o^2 + 2\emptyset\right)}{\dot{\emptyset}^2}\right)^{3/2}}\right\} = \frac{1}{2}\left(\sigma_y + \mu \frac{\dot{\emptyset}}{b^2}\right). \tag{92}$$

The third and final case involves deep penetration into low sound speed materials. The penetration is supersonic; a shock wave representing a discontinuity in stress and particle velocity separates quiescent material from plastically flowing material. If the wave is assumed to be a radially

43

diverging cylindrical wave that follows the experimentally observed linear
relationship between particle and wave velocities, then the radial stress may
be estimated from the one-dimensional Rankine-Hugoniot relations:

$$\sigma_{rr} = \rho C u_p \tag{93}$$

where the stress is proportional to the wave speed C, the particle velocity $u_p$
and the undeformed density, $\rho$. The aforementioned relationship between wave
and particle velocities is given by:

$$C = C_o + \lambda u_p \tag{94}$$

where the material constants are available in tabular form from several shock
property compendia [112, 113, 114]. Combining equations (93) and (94) with
the particle velocity expression (80) at shock position, b(t), yields:

$$\sigma_{rr}(b) = \rho \, \frac{\dot{\phi}}{b} \left\{ C_o + \lambda \, \frac{\dot{\phi}}{b} \right\} \tag{95}$$

and upon combination with equation (87) the governing ordinary differential
equation becomes:

$$\left\{ \rho \ddot{\phi} + \sigma_y \right\} \ell n \left[ \frac{a_o^2 + 2\phi}{b_o^2 + 2\phi} \right]^{1/2} + \frac{1}{2} \left( \rho \dot{\phi}^2 - \mu \dot{\phi} \right) \left( \frac{1}{a_o^2 + 2\phi} - \frac{1}{b_o^2 + 2\phi} \right) +$$

$$\frac{1}{2} \rho r_p^2 U^3 \left\{ \frac{\left| \ddot{\phi} \, (a_o^2 + 2\phi)^{1/2} - \phi^2 \, (a_o^2 + 2\phi)^{-1/2} \right|}{\dot{\phi}^3 \left( 1 + \frac{U^2(a_o^2 + 2\phi)}{\dot{\phi}^2} \right)^{3/2}} \right\} = \tag{96}$$

$$\rho \, \frac{\dot{\phi}}{(b_o^2 + 2\phi)^{1/2}} \left\{ C_o + \lambda \, \frac{\dot{\phi}}{(b_o^2 + 2\phi)^{1/2}} \right\} .$$

## G.  The Determination of the Initial Conditions

The previous section coupled the deformation Regions by applying
appropriate matching conditions at the boundaries of the plastic Regions II
and III.  The resulting ordinary differential equations, while highly
nonlinear are certainly simpler to solve than the original non-linear
partial differential equations.  Equations (88), (92) and (96) are not likely
to yield exact solutions in their full form.  Either additional approximations
must be applied to reduce these to more tractable analytic form or the
equations could be approximately solved with many standard numerical
techniques.  However, before either approach may be pursued, two initial
conditions on $\phi(t)$ and the initial values $a_o$ and $b_o$ must be independently
specified to make the system determinant.  The target density, $\rho$, the
penetrator dimension, $r_p$, the steady penetration rate, U, the target yield
strength, $\sigma_y$, the target viscosity, $\mu$, and the shock properties $C_o$ and $\lambda$ are
problem parameters which must also be known before a solution is obtained.

The cavity expansion process begins when the penetrator/target interface arrives at a particular z-plane of interest. The penetrator interface proceeds through the remainder of the target in a steady fashion but the trailing cavity expands radially through an unsteady process. It is this acceleration of the cavity wall in the radial direction that is the heart of this report. Both experiments and higher-order numerical solutions have shown that there is a region which preceeds this moving interface that accelerates the originally quiescent target material to some undetermined velocity and stress configuration. Figure 14 shows the essential characteristics necessary to establish the initial conditions.



Figure 14. Schematic Description of the Interaction "Bulb"

The first initial condition has already been implicitly defined. The current position of an element, a(t), displaced from its original position, $a_o$, was determined from the incompressible continuity equation as:

$$a(t) = \left[a_o^2 + 2\emptyset(t)\right]^{1/2}.$$  (97)

By definition, therefore:

$$\emptyset(0) = 0.$$  (98)

The initial radial velocity of the cavity wall at this initial radial position has also been determined:

$$\dot{a}(0) = \frac{\dot{\phi}(0)}{a_o} \tag{99}$$

but at this point, its value is undetermined. It is known that the value should be finite and positive. Expression (99) along with the requirement that the initial radial velocity be finite precludes the possibility of $a_o$ equaling zero. Indeed the stress distributions would also be singular upon the axis of symmetry ($r=0$) if this were allowed. $a_o$ is, therefore, slightly offset from this axis.

Hill [79] and Eichelberger [61] recognized the necessity of determining the radial velocity behavior so that the penetration process might be more completely understood. Hill assumed that the cavity wall initially maintains contact with a symmetrical ovoid shaped penetrator "bulb" and that the radial velocity is proportional to the steady penetration velocity and the instantaneous slope of the interaction surface described by:

$$a = A \sin \frac{\pi}{2} \frac{z}{L} \cdot \tag{100}$$

The radial velocity is then defined:

$$\dot{a} = U \frac{da}{dz} \tag{101}$$

or

$$\dot{a} = \frac{\pi}{2} U \frac{A}{L} \cos \left( \frac{\pi}{2} \frac{z}{L} \right) \cdot \tag{102}$$

For the initial value, $z=0$ and, therefore:

$$\dot{a}(0) = \frac{\pi}{2} \frac{A}{L} U \tag{103}$$

but the ratio A/L is not necessarily known a priori. If the surface is hemispherical in shape, the ratio A/L is unity.

Eichelberger [61], in an attempt to verify the proportionality between $\dot{a}(0)$ and U, performed instrumented jet penetration experiments. Considering a steel jet penetrating a steel target, a jet collection technique together with a rotating mirror camera and a film switch/oscillograph method was used to simultaneously determine the jet velocity (V), penetration velocity (U) and mass (M) as a function of time. The incremental mechanical work (dK) done by the jet in displacing an incremental volume, $d\tau$, was derived as:

$$\frac{dK}{d\tau} = UV \frac{dM}{d\tau} \cdot \tag{104}$$

The experimental values of the above expression were plotted against $U^2$ and the result is presented in Figure 15. In an earlier theoretical effort, Bethe [19] derived an expression for the work required to expand a cylindrical hole to a volume, $\tau$. In differential form this relationship was given:

$$\frac{dK}{d\tau} = UV \frac{dM}{d\tau} = \hat{A} + B U^2 \tag{105}$$

46
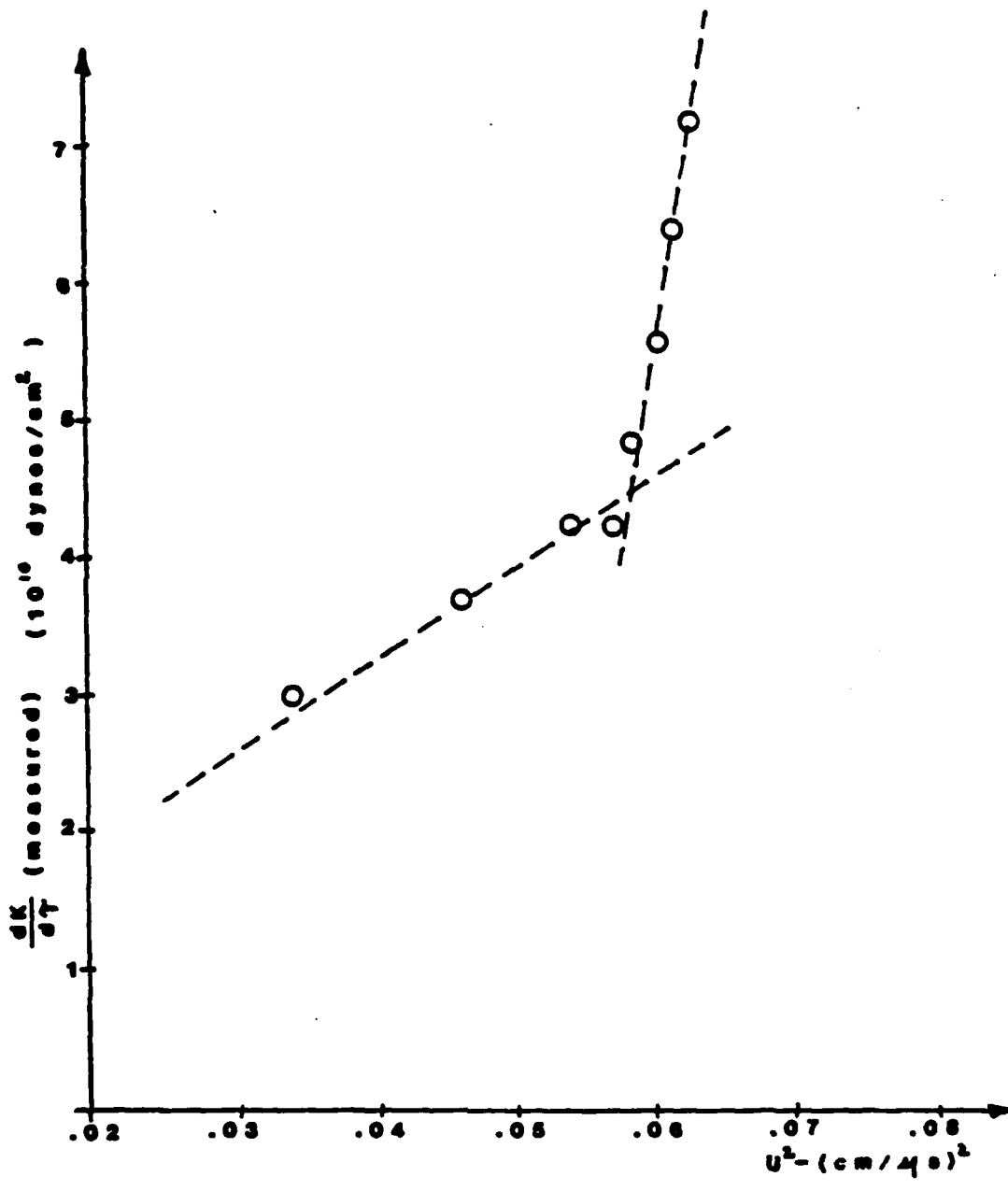
Figure 15. Mechanical Work per Unit Volume Plotted as a Function of
the Square of the Penetration Velocity, Eichelberger [61]

where $\widehat{A}$ represents an average flow stress during plastic deformation and b was given as $.455\rho \left(\frac{\dot{a}}{u}\right)^2$ where $\dot{a}$ is the radial velocity. By measuring the slopes from Figure 15 directly, $\dot{a}(0)$ (the initial radial velocity) can be estimated. For penetration velocities greater than $2.5 \times 10^5$ cm/s, the radial velocity is given by:

$$\dot{a}(0) = 1.4 U \qquad (106)$$

and for penetration velocities below $2.5 \times 10^5$, it appears that:

$$\dot{a}(0) = .43 U \qquad (107)$$

is more appropriate. Öpik [39] developed an approximate hydrodynamic theory for the motion of cavities produced by the impact of meteorites. By assuming that resistance in the axial and radial directions is of the same form, he applied the steady Bernoulli equation and obtained the following value for the cavity's initial radial velocity:

$$\dot{a}(0) = \sqrt{\frac{\rho}{\rho + \rho_p}}\, U \qquad (108)$$

where $\rho_p$ is the penetrator density. For similar target and penetrator materials:

$$\dot{a}(0) = \frac{\sqrt{2}}{2}\, U\ . \qquad (109)$$

Considering the level of approximations invoked to obtain the above expressions, the precise value of the initial radial velocity is still unavailable. To at least narrow the limits within which $\dot{a}(0)$ may vary, an analogy can be made to the theory of compressible axisymmetric stagnation flow. White [115] discusses the case of fluid flow past bodies of revolution of finite dimension, D, and approach velocity, U. The value of the local velocity gradient $\overline{K}$ at the stagnation point and the distance, x, from this point determine the velocity of the flow field on the edge of the boundary, $U_e$, as:

$$U_e = \overline{K}x\ . \qquad (110)$$

The velocity gradient $\overline{K}$ depends upon D and U and to a lesser extent, upon the body shape and approach Mach number. For subsonic fluid flow (Mach number <1), the Rayleigh-Janzen procedure can be used to estimate the velocity gradient $\overline{K}$. Two body shapes, presented by White, are suitable for further investigation. They are the flatnosed cylinder and the sphere. Experiments conducted by Fugelso [63] and Weihrauch [73] consider the penetration of high speed metallic rods (V = 1-2 km/s) into thick finite targets. The shapes of the interaction surface are observed with flash x-ray photography. The surfaces nearest to the stagnation region appear to be somewhat between flat and hemispherical. At higher velocities, shaped charge jets have been radiographed (unpublished Ballistic Research Laboratory experiments) while penetrating into homogeneous targets. The penetrator interaction surfaces have similar shapes as those of the constant velocity rod experiments. Finite difference calculations of Harlow [55] and Kucher [56] further support these observations.

48

Throughout this report, it has been assumed that the penetration process is steady when considering the axial penetration rate. The accuracy has been experimentally and numerically confirmed. In addition to the rate being steady, the shape of the interaction surface is assumed to remain unchanging as the penetration proceeds. The validity of this approximation is qualitatively confirmed by the experiments just mentioned. If the target material behaves like a fluid in this stagnation region, then the expressions for the sphere and blunt-nosed cylinder, presented by White [115], determine the initial radial velocity of the cavity wall near the axis of symmetry. Recalling equation (110) the radial velocity, $\dot{a}(0)$ is related to the stagnation gradient, $\overline{K}$ and the initial radial position, $a_o$ by:

$$\dot{a}(0) = \overline{K}a_o .$$
(111)

If the initial radial velocity $a(0)$ occurs at the point where surface curvature begins (up to this point the surface is flat) then the blunt-nosed cylinder configuration, Figure 16, is plausible. White notes that while the compressible stagnation gradient, $\overline{K}$ is not known for this configuration, it should be less than the incompressible spherical and greater than the supersonic blunt-nose measurement $\left(\overline{K} = .15 \frac{U}{a_o}\right)$ of Trimmer [116]. White

determines an incompressible value of $\pi/4 \frac{U}{a_o}$ , equation (111) then becomes:

$$\dot{a}(0) = \frac{\pi}{4} U .$$
(112)
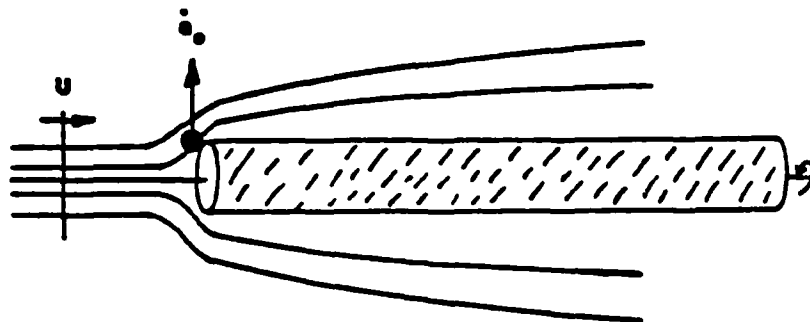


Figure 16. Blunt-nosed Cylinder in an Uniform Flow

If the interaction surface geometry is more hemispherical near the axis of symmetry and the flow is subsonic ($U < .6\ C_o$), then the Rayleigh-Janzen procedure may be applied to estimate the stagnation velocity gradient. Kaplan [117] considers a sphere in an uniform compressible flow. The incompressible solution is expanded in powers of the Mach number, and the resulting velocity and pressure distributions are presented for a sphere of diameter, D and flow velocity, U.
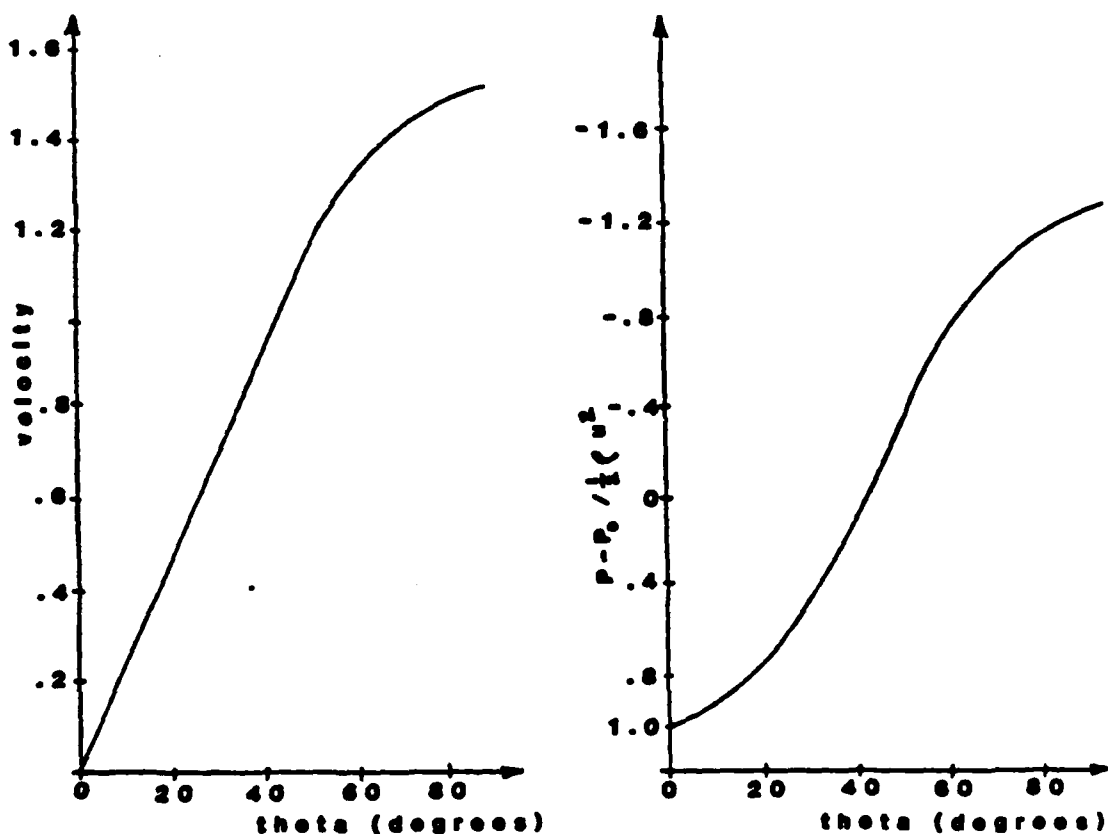


Figure 17. The Velocity and Pressure Distributions upon the Surface of a Sphere (Kaplan [117])

Near the stagnation point ($\theta = 0$) the velocity varies linearly with radial position and the pressure varies only slightly for angles less than ten degrees. White [115] determined the stagnation velocity gradient for this case:

$$\frac{\overline{K}D}{U} = 3\ (1 - 0.252M_o^2 - 0.175M_o^4 + \ .\ .\ .) \tag{113}$$

50

where the Mach number $M_o$ is defined as the ratio of the velocity $U$ to the characteristic wave speed, $C_o$. From radiographic evidence it can be observed that the diameter of the interaction region is typically less than four times the penetrator radius, $r_p$, or

$$D \leq 4 \, r_p \tag{114}$$

and upon combination with equations (111) and (113) yields,

$$\dot{a}(0) \geq \frac{3}{4} \frac{a_o}{r_p} U \left(1 - 0.252 M_o^2 - 0.175 M_o^4 + \ldots \right). \tag{115}$$

This inequality is valid only for penetration rates less than $.6 \, C_o$. As an example of its utility, however, consider the case of a kinetic energy penetrator perforating a steel target at 2 km/s ($V = 3.5$ km/s). The sound speed is approximately 6 km/s and the Mach number is, therefore, .33. The difference between the incompressible and compressible estimates is only three percent. This difference will become greater as the impact velocities increase. The ratio $a_o/r_p$ is as of yet undetermined but should be of the order of unity if the limit (115) is to agree reasonably with the earlier estimates of Öpik, Eichelberger and White (blunt-nosed cylinder). The investigations above suggest the following approximation:

$$\dot{a}_o = KU \tag{116}$$

where the constant $K$ is between 0.4 and $\sqrt{2}$ for geometries somewhere between flatnosed and hemispherical and for all penetration velocities (compressible or not). If the constant $K$ can be presumed to be known, then two initial parameters, $a_o$ and $b_o$, still remain to be determined before the cavity growth equation (87) may be integrated.

The two initial conditions, $\emptyset(0)$ and $\dot{\emptyset}(0)$ are restated:

$$\emptyset(0) = 0 \tag{117}$$

and from equations (99) and (116):

$$\dot{\emptyset}(0) = a_o KU \; . \tag{118}$$

The maximum pressure, $P_o$, occurs at the moving stagnation point along the symmetry axis. Kaplan [117], considering subsonic flow around a sphere, observes that the pressure varies only slightly from the stagnation value for angles up to approximately ten degrees from the symmetry axis. Therefore, for initial cavity positions close to the symmetry axis, the pressure is given approximately by the Bernoulli equation (Appendix A) as:

$$P_o = \frac{1}{2} \rho U^2 \tag{119}$$

where the density is the ambient target density and $U$ represents the steady penetration velocity. The pressure in the penetration Region I was derived as:

$$P(t) = \frac{1}{2} \rho r_p^2 U^3 \frac{\left| \ddot{\emptyset} a - \dot{\emptyset}^2/a \right|}{\dot{\emptyset}^3 \left(1 + \frac{U^2 a^2}{\dot{\emptyset}^2}\right)^{3/2}} \; . \tag{120}$$

51

The value of P at time, $t = 0$ is determined by substituting (98) and (118) into expression (120) and upon equating this value with equation (119), the following relation results:

$$|\ddot{\emptyset}_o - K^2 U^2| = [1 + K^2]^{3/2} \frac{a_o^2}{r_p^2} U^2 \qquad (121)$$

where $\ddot{\emptyset}_o$ represents the initial value of $\ddot{\emptyset}(t)$. The absolute value character of (121) can be eliminated by the following argument. The expression for the radial acceleration of a point on the cavity surface was determined as:

$$\ddot{a}(t) = \frac{\ddot{\emptyset}(t)}{a(t)} - \frac{\dot{\emptyset}^2(t)}{a(t)^3} . \qquad (122)$$

Its initial value at the radius $a_o$, with the assumed initial conditions is:

$$\ddot{a}_o = \frac{1}{a_o} [\ddot{\emptyset}_o - K^2 U^2]. \qquad (123)$$

From inspection of the shape of the interaction region during steady penetration, the curvature requires that $\ddot{a}_o$ be negative. Since $a_o$ is finite and positive, equations (123) and (121) then require that

$$\ddot{\emptyset}_o = \left\{ K^2 - [1 + K^2]^{3/2} \frac{a_o^2}{r_p^2} \right\} U^2 . \qquad (124)$$

The radial equation of motion along with the condition of stress continuity at the cavity, at time $t = 0$ is:

$$\left\{ \rho \ddot{\emptyset}_o + \sigma_y \right\} \ln \frac{a_o}{b_o} + \frac{1}{2} \left\{ \rho K^2 U^2 - \mu \frac{KU}{a_o} \right\} \left( 1 - \frac{a_o^2}{b_o^2} \right) = - \frac{1}{2} \rho U^2 \qquad (125)$$

for the subsonic, finite lateral dimension case,

$$\left\{ \rho \ddot{\emptyset}_o + \sigma_y \right\} \ln \frac{a_o}{b_o} + \frac{1}{2} \left\{ \rho K^2 U^2 - \mu \frac{KU}{a_o} \right\} \left( 1 - \frac{a_o^2}{b_o^2} \right) - \frac{1}{2} \left( \sigma_y + \mu KU \frac{a_o}{b_o} \right) = - \frac{1}{2} \rho U^2 \qquad (126)$$

for the subsonic, semi-infinite lateral dimension problem and

$$\left\{ \rho \ddot{\emptyset}_o + \sigma_y \right\} \ln \frac{a_o}{b_o} + \frac{1}{2} \left\{ \rho K^2 U^2 - \frac{\mu K U}{a_o} \right\} \left( 1 - \frac{a_o^2}{b_o^2} \right) - \rho \frac{a_o}{b_o} KU \left( C_o + \lambda \frac{a_o}{b_o} KU \right) = - \frac{1}{2} \rho U^2 \qquad (127)$$

for the case of supersonic penetration.

Combining equations (124), (125) and (126) dividing through both sides by $\rho U^2$ and neglecting the small terms, $\sigma_y / \rho U^2$ and $(a_o/b_o)$ yields:

52

$$\left\{ K^2 - [1 + K^2]^{3/2} \frac{a_o^2}{r_p^2} \right\} \ln \frac{a_o}{b_o} + \frac{1}{2} \left\{ K^2 - \frac{\mu K}{\rho a_o U} \right\} = - \frac{1}{2} \qquad (128)$$

which is approximately true for all three cases. If further,

$$\mu/K\rho a_o U \ll 1 \qquad (129)$$

an assumption which may be verified by applying the material constants $\rho$, $\mu$, the penetration velocity, U and recognizing that $a_o = \bigcirc (r_p)$, then equation (128) reduces to:

$$\left\{ K^2 - [1 + K^2]^{3/2} \frac{a_o^2}{r_p^2} \right\} \ln \frac{a_o}{b_o} = - \frac{1}{2} \left( 1 + K^2 \right). \qquad (130)$$

For the first boundary case considered, the outer boundary, $b_o$, is known and equation (130) relates $a_o$ with the estimated value of K. For the other cases, however, the boundary location, $b_o$, is not necessarily known a priori. In order to determine $a_o$ and $b_o$ for these two cases, a control volume is proposed, centered on the radial position, $b_o$, moving with the boundary velocity $\dot{b}_o$. Ignoring the negligible curvature as the radius increases, the one dimensional conservation of radial momentum requires that:

$$\sigma_r(b_o)A = \int_{c.s.} \dot{b}_o \, \rho \, \dot{b}_o ds = \rho \dot{b}_o^2 A$$

or

$$\sigma_r(b_o) = \rho \left( \frac{\dot{\phi}_o}{b_o} \right)^2 = \rho K^2 U^2 \left( \frac{a_o}{b_\sigma} \right)^2 . \qquad (131)$$

Equating (131) with the stress on the elastic/plastic interface,

$$\sigma K^2 U^2 \left( \frac{a_o}{b_o} \right)^2 = \frac{1}{2} \left( \sigma_y + \mu \frac{\dot{\phi}_o}{b_o^2} \right) = \frac{1}{2} \left( \sigma_y + \mu \frac{a_o K U}{b_o^2} \right) \qquad (132)$$

and once again recognizing that $a_o/b_o \ll 1$ then,

$$\frac{a_o}{b_o} \simeq \frac{\left( \sigma_y/2\rho U^2 \right)^{1/2}}{K} . \qquad (133)$$

Combining equations (133) and (130) establishes a relationship between the initial cavity radius and the initial cavity velocity coefficient, K:

$$\left\{ K^2 - [1 + K^2]^{3/2} \frac{a_o^2}{r_p^2} \right\} \ln \frac{\left( \sigma_y/2\rho U^2 \right)^{1/2}}{K} = - \frac{1}{2} (1 + K^2) . \qquad (134)$$

53

Given a value of K, the initial radius, $a_o$, the initial plastic boundary, $b_o$ and the initial condition $\dot{\emptyset}(0)$ can be estimated. This estimate may be improved by relaxing the approximation (129) and iteratively adjusting $a_o$ until equation (128) is satisfied to the desired accuracy.


## III. SOLUTION OF THE INITIAL VALUE PROBLEM

The preceding chapter established an iterative method for determining the initial conditions necessary for integration of the governing equations; either exactly or numerically. The method required that the initial radial stress equal the stagnation pressure at an initial radius slightly displaced from the symmetry axis and that the radial stress at the plastic boundary be initially given by the one dimensional momentum jump condition. The cavity then radially expands in a decelerating fashion until the stresses in the plastic regions reach values of the order of the static yield strength. When this happens, the problem is for practical purposes completed. It is quite likely, however, that elastic deformations will continue until the stresses vanish completely; but due to their relative magnitudes, they may be practically neglected. The problem will be assumed complete when the stresses everywhere in the plastic regions reach the static elastic range.

## A. Runge-Kutta Solutions to the Complete System

The integration of ordinary differential equations by numerical techniques is well established. Choice of the specific method is usually based upon the ease of application as well as the type of equation considered. In general, equations of second or higher order can be reduced to systems of first order equations, e.g.,

$\ddot{y} = f(x, y, \dot{y})$ can be written as

$\dot{y} = z$

$\dot{z} = f(x, y, z),$

a pair of simultaneous first order equations. One of the most common methods used to solve this system of first order equations is the process of Gill [118]. It differs slightly from the fourth order accurate method originally proposed by Runge [119] in the precise values of the expansion parameters (Cohen [120] compares the two methods). A FORTRAN program of Gill's method is given as an appendix in the text by White [115] and reproduced here (Tables 1 and 2) with the programming logic appropriate to this problem.

The logic located between statements 10 and 20 are expressions for the system of first order differential equations representing the second order differential equation in $\emptyset(t)$ for the subsonic, semi-infinite target case (92). The input parameters are described in order of the occurrence:

X = initial problem time (zero for this problem)

XLIM = maximum problem time (limits actual computer run time)

H = time step (constant for this problem, but not restricted)

M = an index which must be set to zero by the programmer

N = number of first order differential equations (2 for this program)

SIGY = inviscid target yield strength (dynes/cm$^2$)

C$\emptyset$ = bulk sound speed of the target (cm/s)

## Table 1. Runge-Kutta Program

```fortran
      PROGRAM SCOTT(INPUT,OUTPUT,TAPE5=INPUT,TAPE6=OUTPUT)
C
C        4TH ORDER RUNGE KUTTA SOLUTION  ( GILL'S METHOD )
C
      DIMENSION Y(4),F(4)
      REAL MU,LAMDA
    3 FORMAT(2X,'SIGY=',E10.3,'CO=',E10.3,'RHOT=',F10.2,'  MU=',E10.2,'R
     1P=',F10.2,'LAMDA=',E10.2,'U=',E10.2/2X,'Y1=',E10.3,'Y2=',E10.3,2E1
     10.3)
    4 FORMAT(3F10.4,2I5)
    5 FORMAT(8F10.3)
    9 FORMAT(10X,'X= ',E10.3,'XLIM= ',E10.3,'H= ',E10.3,2I5)
   11 FORMAT(2X,'TIME= ',E10.3,'PHIDOT= ',E10.3,'PHI= ',E10.3,'A= ',E10.
     13,'PCHECK= ',E10.3)
   33 FORMAT(8E10.3)
      READ(5,4)X,XLIM,H,M,N
      READ(5,5)SIGY,CO,RHOT,MU,RP,R,U,LAMDA
      READ(5,5)Y(1),Y(2),BO,AO
      WRITE(6,9)X,XLIM,H,M,N
      WRITE(6,3)SIGY,CO,RHOT,MU,RP,LAMDA,U,Y(1),Y(2),BO,AO
      JFLAG=0
      ZZ=0.0
      Z1=0.0
    8 IF(X-XLIM)6,6,7
    6 CALL RUNGE(M,Y,F,X,H,N,K)
      GO TO (10,20),K
   10 A1=AO**2.+2.*Y(2)
      A=SQRT(A1)
      B1=BO**2.+2.*Y(2)
      B=SQRT(B1)
      D=0.5*RHOT*RP**2.*U**3.
      C=ALOG(A/B)
      A2=(1.+U**2.*A1/Y(1)**2.)**1.5
      T1=D/(A*Y(1)*A2)
      A3=(1./B1)-(1./A1)
      T2=((RHOT*Y(1)**2.)-MU*Y(1))*A3/2.
      T3=0.5*(SIGY+MU*Y(1)/B1)
      T4=SIGY*C
      P1=F(1)*A/(Y(1)**3.*A2)
      P2=1./(A*Y(1)*A2)
      PCHECK=D*(P1-P2)
      IF(JFLAG.EQ.0) PCHECK=0.5*RHOT*U**2.
      JFLAG=1
      P=ABS(PCHECK)
      TO=RHOT*C
      F(1)=(T2+T3-T4-P)/TO
      IF(Y(1).LE.0.) GO TO 7
      F(2)=Y(1)
      GO TO 6
   20 Z=SQRT(AO**2.+2.*Y(2))
      ZZ=ZZ+1.
      ZPRINT=1000.
      IF(Z1.EQ.0.) GO TO 25
      IF(ZZ.NE.ZPRINT) GO TO 8
   25 WRITE(6,33)A1,A,B1,B,A2,A3,TO,T1
      WRITE(6,33)T2,T3,T4,F(1),F(2),PO,P1,P2
      WRITE(6,11)X,Y(1),Y(2),Z,PCHECK
      ZZ=0.0
      Z1=1.0
      GO TO 8
    7 STOP
      END
```

55

RHOT = target density $(g/cm^3)$

MU = target viscosity $(dyne - s/cm^2)$

RP = penetrator radius (cm)

U = steady penetration rate (cm/s)

LAMDA = slope of the US-UP data (nondimensional)

$Y(1) = \dot{\phi}(0)$ initial condition $(cm^2/s)$

$Y(2) = \phi(0)$ initial condition $(cm^2)$ ·

BØ = initial position of plastic boundary (cm)

AØ = initial position of cavity surface (cm).

Table 2.  Subroutine Runge

```
C     GILL'S METHOD-RUNGE KUTTA


C
      SUBROUTINE RUNGE(N,Y,F,X,H,M,K)
      DIMENSION Y(4),F(4),Q(4)
      M=M+1
      GO TO (1,4,5,3,7),M
 1    DO 2 I=1,N
 2    Q(I)=0.
      A=0.5
      GO TO 9
 3    A=1.7071067811865475244
 4    X=X+H*0.5
 5    DO 6 I=1,N
      Y(I)=Y(I)+A*(F(I)*H-Q(I))
 6    Q(I)=2.*A*H*F(I)+(1.-3.*A)*Q(I)
      A=.292893218813452475G
      GO TO 9
 7    DO 8 I=1,N
 8    Y(I)=Y(I)+H*F(I)/6.-Q(I)/3.
      M=0
      K=2
      GO TO 10
 9    K=1
 10   RETURN
      END
```

The case of subsonic penetration into a target with small lateral dimension
can be considered by setting the program variable, T3, to zero throughout the
calculation.  The program then solves equation (88) which was derived by
applying a traction free boundary condition to this lateral surface.  The
supersonic penetration case can be similarly considered by substituting the
expression for T3 with,

T3 = RHOT*(Y(1)/B)*(CØ + LAMDA*Y(1)/B)

which represents the jump stress at the shock surface (also the
elastic/plastic boundary) derived from the one-dimensional Rankine-Hugoniot
relations.

The material properties, SIGY, CØ, RHOT, LAMDA and MU must be supplied
since no default values are included.  The first three may be found in con-
ventional material handbooks.  The viscosity coefficient, MU, may be estimated
in many cases from the literature review of Walters [125], as described in
Appendix B; otherwise, an independent experiment is required to determine this

parameter. The design parameters, RP and U, must also be specified before the calculations may proceed. In the case of a kinetic energy projectile, RP is the design value, but for high velocity jets, a precise value is not usually known. Estimates can be made from flash x-ray photographs taken of the jet before and after it interacts with a particular target element. The penetration velocity, U, can either be determined experimentally or calculated from the one dimensional steady model (Appendix A).

The initial conditions, Y(1), Y(2), AØ and BØ are entered as input and must be determined by the method described in the preceding chapter. The remaining input parameters, X, XLIM, H, M and N are related to the solution execution. The initial time, X, is zero. The solution proceeds out to the time specified, XLIM, or to the point where the velocities drop to zero (all stresses are of elastic magnitude). M and N should be set to zero and two respectively. The time step, H, is constant throughout the calculation. Its value must be selected with care. The characteristic time of most cavity expansion processes is of the order of microseconds, consequently H must be of an order less than this to insure temporal resolution as well as numerical convergence. Since the length of the calculation depends inversely upon the step size, an infinitesimally small value is prohibitive. A suggestion for the determination of an appropriate step size is that one selects a reasonably small value, say $10^{-9}$ seconds and allows the program to run its course. Then select an order of magnitude smaller value and let the program run once again. The difference between the two calculations should be very small and the solutions should converge as the step size is progressively diminished. The choice of the final step size will then be limited between a value that ensures numerical convergence and a value that is reasonable from a cost (computer time) viewpoint. For the range of problems considered in this report, a value of $10^{-10}$ seconds is appropriate.

## B. Reduction to Quadrature via Additional Approximations

The equations developed in Section II represent the cavity growth behavior, stress distributions and velocity distributions that can be expected during deep steady penetration. Approximations concerning the nature of the behavior were made after reviewing experimental and computational evidence. The governing equations of motion were subsequently reduced to single, second order, ordinary differential equations which, unfortunately, are highly nonlinear, thereby making their exact solution very difficult, if not impossible. In Section IIIA a Runge-Kutta technique is described which can be utilized to solve the full equations numerically. In this section, additional approximations are imposed to simplify the equations so that an exact solution is possible.

Suppose the viscosity is negligible and the pressure at the inner boundary vanishes quickly so that the cavity expansion process involves only the initial momenta and stress distributions, then equation (92) reduces to:

$$\left\{ \rho \ddot{\phi} + \sigma_y \right\} \ln \frac{a}{b} + \frac{1}{2} \dot{\phi}^2 \left( \frac{1}{a^2} - \frac{1}{b^2} \right) = \frac{1}{2} \sigma_y. \tag{135}$$

The plastic boundary, b, is typically much greater than the cavity dimension, a, thereby suggesting the approximation:

57

$$\left(\frac{1}{a^2} - \frac{1}{b^2}\right) \simeq \frac{1}{a^2} . \tag{136}$$

If further it is assumed that the logarithmic term does not vary significantly during the expansion process,

$$\ln \frac{a}{b} = \ln \frac{a_o}{b_o} = \overline{K}_1 \tag{137}$$

then equation (135) simplifies to:

$$\ddot{\emptyset} + \frac{1}{2} \frac{\dot{\emptyset}^2}{\overline{K}_1(a_o^2 + 2\emptyset)} = \frac{\sigma_y}{\rho} \left\{ \frac{1}{2\overline{K}_1} - 1 \right\} . \tag{138}$$

Define the new variables,

$$y = \frac{1}{2} \overline{K}_1(a_o^2 + 2\emptyset) = n(a_o^2 + 2\emptyset)$$

$$\dot{y} = 2n\dot{\emptyset}$$

$$\ddot{y} = 2n\ddot{\emptyset}$$

$$A_1 = \frac{\sigma_y}{\rho} \left(\frac{1-n}{n}\right)$$

then (138) becomes:

$$2nA_1 y = y\ddot{y} + \frac{\dot{y}^2}{2n} . \tag{139}$$

Let $\hat{P} = \frac{dy}{dt} = \dot{y}$ and $\ddot{y} = \frac{d}{dt} \hat{P} = \frac{dy}{dt} \frac{d}{dt} \hat{P} = \hat{P} \frac{d\hat{P}}{dy}$

then (139) becomes:

$$2nA_1 y = yP \frac{dP}{dy} + \frac{P^2}{2n} . \tag{140}$$

Let $\hat{z} = \hat{P}^2$ then $\frac{d\hat{z}}{dy} = 2\hat{P} \frac{d\hat{P}}{dy}$ and (140) becomes:

$$4nA_1 = \frac{d\hat{z}}{dy} + \frac{\hat{z}}{ny} . \tag{141}$$

Let $\hat{m} = \frac{\hat{z}}{ny}$ with $\frac{d\hat{m}}{dy} = \frac{1}{n} \frac{y \frac{d\hat{z}}{dy} - \hat{z}}{y^2}$ and then (141) becomes:

$$4nA_1 = ny \frac{d\hat{m}}{dy} + n\hat{m} + \hat{m}$$

58

or rearranged as:

$$\frac{dy}{y} = \frac{d\hat{m}}{4nA_1 - \hat{m}(n+1)} .$$ (142)

Integrating both sides yields:

$$\ln y = \frac{-n}{(n+1)} \ln \left\{ 4nA_1 - (n+1)\hat{m} \right\} + \ln C_1$$ (143)

or

$$yC_1 = \left\{ 4nA_1 - (n+1)\hat{m} \right\}^{-\frac{n}{n+1}}$$

or

$$\hat{m} = \frac{4nA_1 - (yC_1)^{-\frac{n+1}{n}}}{n+1} .$$ (144)

Performing the inverse transformations, $\hat{z} = \hat{m}y$, $\hat{P} = \sqrt{\hat{z}}$ and $\frac{dy}{dt} = \hat{P}$ yields:

$$dt = \left\{ \left(\frac{n}{n+1}\right) \left( 4nA_1 y - C_1^{\left(\frac{n}{n+1}\right)} y^{\left(\frac{2n+1}{n+1}\right)} \right) \right\}^{-1/2} dy.$$ (145)

The problem has been, therefore, reduced to numerical quadrature. A function, $t = f(y)$ will result. The inverse of this expression, $y = f(t)$ then determines $\emptyset(t)$ through the inverse transform:

$$\emptyset(t) = 1/2\left(\frac{y}{n} - a_o{}^2\right).$$ (146)

The advantage of this approach over the numerical solution of the full equations is not obvious. While the quadrature may be performed by hand, a more accurate and timely approach would be to utilize a computer. The difference in computer running cost between a Runge-Kutta solution and a finely partitioned integration algorithm is most likely negligible. Furthermore, the accuracy of the quadrature solution is limited by the approximations invoked to reduce the governing equations to the form (138); these approximation errors typically exceed any error introduced by the fourth order Runge-Kutta algorithm.

Alternate sets of approximations can be applied to the full equations (88), (92) and (96) reducing them to varying forms, some of which may have analytic solutions. The overwhelming limitation to this approach, however, is in the ability to estimate the errors introduced by each approximation. Therefore, for the remainder of this report, the numerical solution to the full equations will be pursued.

## IV. PARAMETRIC DEPENDENCE AND COMPARISON WITH EXPERIMENTS

Section II dealt with the formulation of the cavity expansion problem. The generally complex system of governing field equations was reduced to initial value problems by applying approximations suggested by experiments and previous numerical investigations. Appropriate initial conditions were determined from problem parameters by specification of the boundary stress conditions. Section III dealt with possible solutions of the initial value problems. A Runge-Kutta technique was proposed to solve the full equations (88), (92) and (96) with properly specified initial conditions. The full equations were reduced to a simpler form only after additional approximations, consequently the accuracy of the simplified solution was in question and the advantage to be gained by the simplification was reduced. This section will present Runge-Kutta solutions to the full equations as developed in Section IIF.

The governing equations and initial conditions involve the previously defined problem parameters: $\rho$, $\mu$, $\sigma_y$, $\lambda$, $C_o$, U, $r_p$, K, $a_o$ and $b_o$. The impact velocity, penetrator density and penetrator strength characteristics are implicitly included within the penetration velocity, U (as described in Appendix A). The functional influence of these parameters on the growth behavior of the target cavity appears explicitly in equations (88), (92) and (96) but the relative importance of each parameter for the prediction of the final cavity dimension or the instantaneous growth rate has not yet been determined. Within the following several sections, the parametric dependencies will be presented. The particular examples selected are those that have been studied experimentally, thereby allowing a comparison between the model's predictions and actual measurements. Unfortunately, the growth rate cannot be observed experimentally. However, the time-integrated final value can and will be utilized.

## A. Dependence of the Initial Conditions (K, $a_o$, $b_o$)

As already noted in Section IIG, the precise value of the initial radial velocity, $\dot{a}(0)$ is not known. Estimates are available from different models and the range within which $\dot{a}(0)$ is expected to vary is $0.4U \leq \dot{a}(0) \leq 1.4U$. If K is known, then $a_o$ and $b_o$ are determined by the iterative method described in Section IIG. Therefore, K will be chosen between these limits, $a_o$ and $b_o$ will be subsequently determined and the growth behavior will be predicted for the following situation.

Silsby [121] and Blanks [122] performed experiments that involved the normal impact and penetration of long tungsten alloy rods into armor steel targets. Impact velocities were varied between 2 and 4.5 km/s and the final hole diameters were measured. The resulting cavities were cylindrical in shape and the quoted final cavity diameters represented averages of the diameter at several depths. The lateral dimensions of the steel plate were quite·large and the sound speed in steel is approximately 6 km/s, therefore equation (92), the subsonic, semi-infinite case is selected to model this problem. The following values are assumed:

$$\rho_p = 17.3 \text{ g/cm}^3 \text{ (measured)}$$

$$\rho = 7.85 \text{ g/cm}^3 \text{ (measured)}$$

$$r_p = 0.39 \text{ cm (measured)}$$

$$\sigma_y = 1 \times 10^{10} \text{ dynes/cm}^2 \text{ (Goldsmith [3])}$$

$$V = 4.4 \times 10^5 \text{ cm/s (two measured values}$$

$$V = 3.3 \times 10^5 \text{ cm/s are selected for study)}$$

and the viscosity, $\mu$, is given by Harlow and Pracht [55] as

$$\mu = 2 \times 10^4 \text{ poise (fit to the data of Walsh, et al.}$$
[123]).

The penetration velocity is then determined by equation (A.3) for the two chosen impact velocities. Representative values for the constant K are selected and corresponding $a_o$'s and $b_o$'s are determined. Figure 18 presents the Runge-Kutta solutions for the 4.4 cm/s impact velocity and the following initial condition parameters:

| selected values | values iteratively determined | |
|---|---|---|
| K = 1.400 | $a_o$ = .205 cm | $b_o$ = 3.180 cm |
| K = .780 | $a_o$ = .132 cm | $b_o$ = 1.150 cm |
| K = .700 | $a_o$ = .112 cm | $b_o$ = .838 cm . |

Values of K less than ~.70 were unable to satisfy equation (128) for any initial cavity dimension. Therefore, the correct solution should lie somewhere between the predictions corresponding to K = 1.4 and K = .70. The value, .78, represents the incompressible blunt cylinder configuration presented by White [115]. The predicted final cavity radius for this value agrees quite well with the experimental measurement of Silsby [121]. The final hole dimension does not scale linearly with the constant K, although the magnitude increases as K increases. The time required for the stresses to decay to elastic magnitude increases with increasing K.

Figure 19 presents the Runge-Kutta solutions for the 3.3 km/s impact velocity with the following initial condition parameters:

| selected values | values iteratively determined | |
|---|---|---|
| K = 1.400 | $a_o$ = .200 cm | $b_o$ = 2.220 cm |
| K = .780 | $a_o$ = .119 cm | $b_o$ = .732 cm . |

Once again the value of K = .78 yields a final cavity dimension that agrees reasonably well with the independent experiment for V = 3.3 km/s. Comparing Figure 18 and 19 for the same K, the diameter of the cavity and the time required to reach the final value increase with increasing impact velocity. Additional comparisons with experiments for variable impact velocities will be given in the next section. In addition to the cavity growth curves, the stress distributions, $\sigma_{rr}$ and $\sigma_{\theta\theta}$, are presented in Figure 20 for three times

61
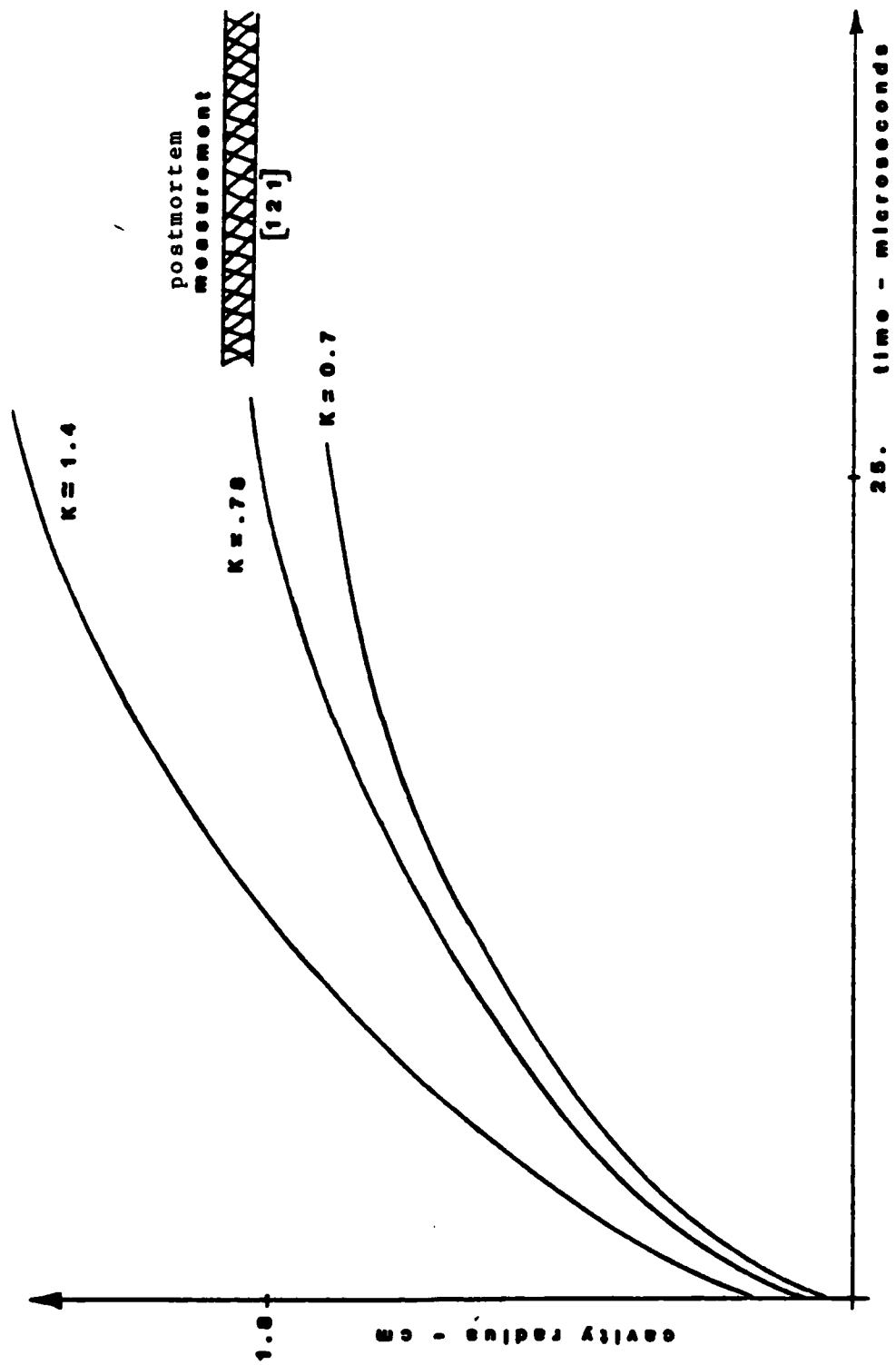
Figure 18.  Parametric Dependence of the Initial Condition Constant, K for Impact Velocity, 4.4 km/s.
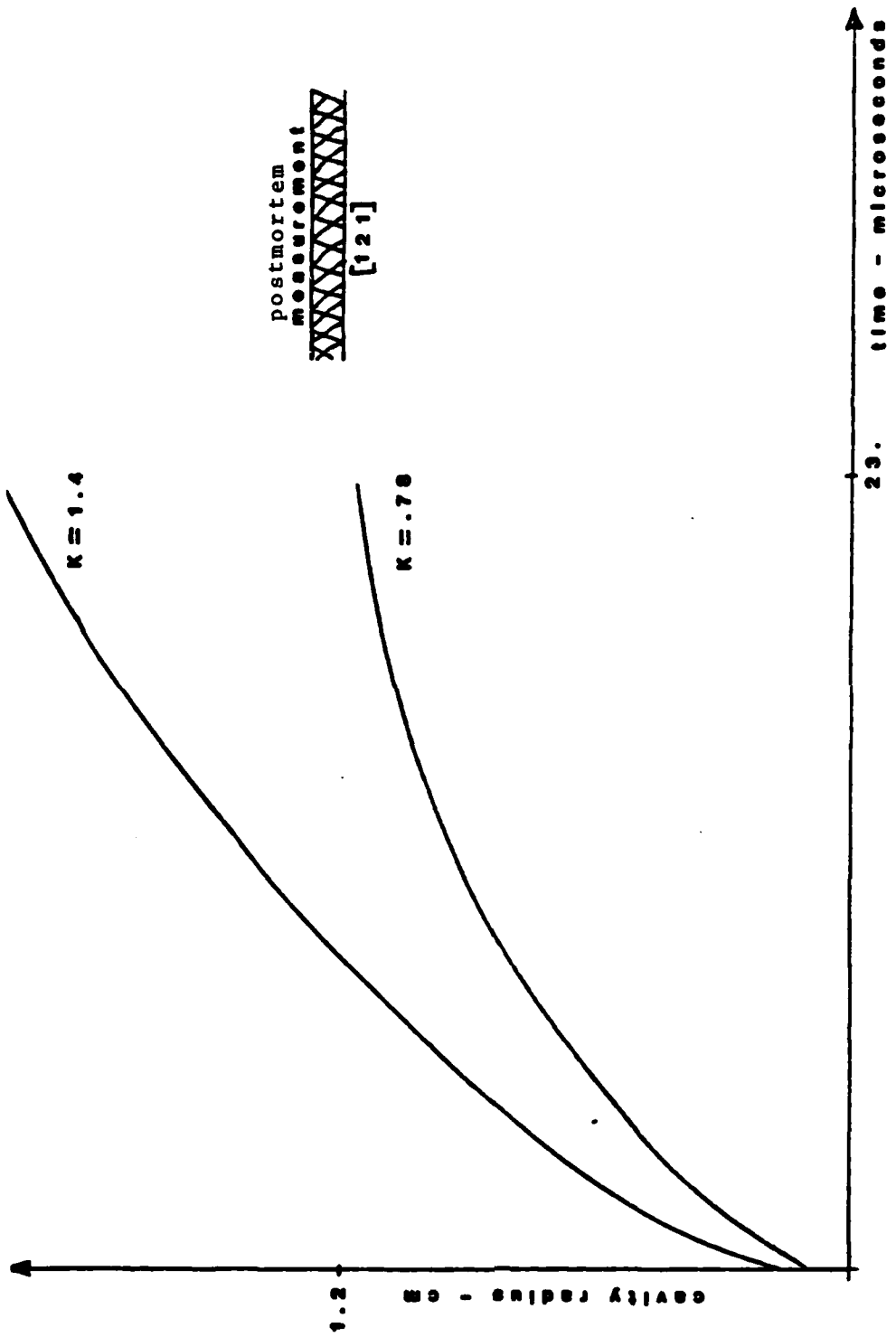
Figure 19. Parametric Dependence of the Initial Condition Constant, K for Impact Velocity, 3.3 km/s.
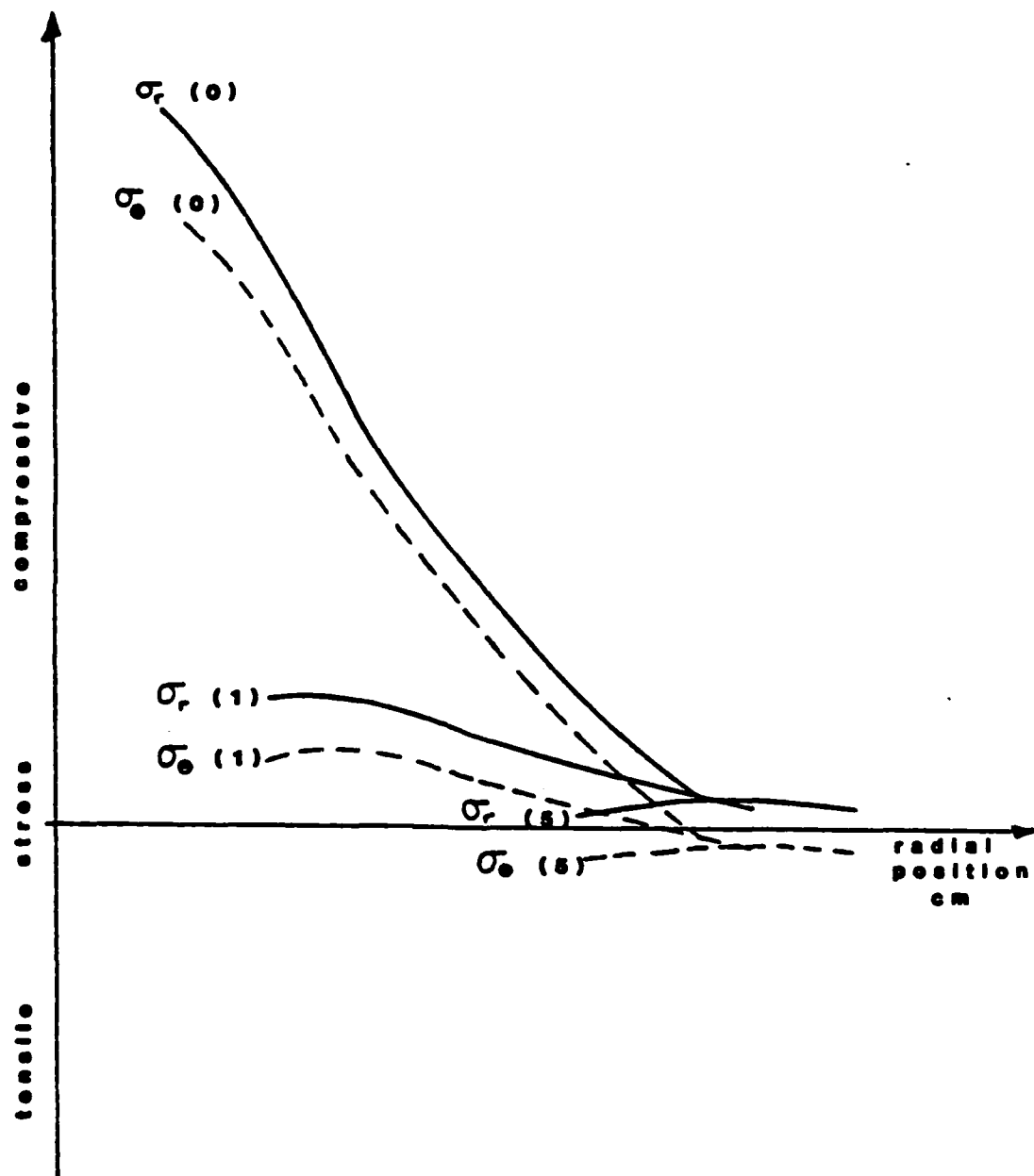
Figure 20. Radial and Circumferential Stress Distributions at 0, 1 and 5 Microseconds for V = 3.3 km/s.

after the penetrator surface passes the particular axial plane. Both radial and circumferential stresses are initially compressive near the cavity, the circumferential stress is less than the radial stress by the amount,

$(\sigma_y + \mu\dot{\phi}/r^2)$ and is tensile near the elastic/plastic boundary. As time progresses, both stresses decay in magnitude and at 5 microseconds, the radial stress is compressive while the circumferential stress is completely tensile. The spatial gradients of both stress components decay very quickly. At 5 microseconds, the stress distributions appear almost spatially flat, but their difference still exceeds the static yield stress; therefore plastic flow will continue until the yield criterion is no longer met. This occurs at approximately 23 microseconds (Figure 19).

The selected value of K significantly influences the final cavity dimension, the time to reach this value and the instantaneous velocity at any radial coordinate. For the case just considered, the estimate based upon the incompressible flow over a blunt cylinder yields an accurate prediction of the final cavity dimension for both impact velocities. A value of K = .78 will, therefore, be assumed for the remaining parametric calculations.

## B. Dependence upon Impact Velocity and Static Target Strength

The previous section presented cavity growth solutions to equation (92) for the case of a tungsten alloy rod penetrating armor plate. The solutions were observed to depend upon the initial condition parameter, K, which relates the initial radial velocity with the steady penetration velocity, U. A value of K = .78 produced reasonable agreement between the calculation and the experiments of Silsby [121]. Hohler and Stilp [66] performed experiments with both steel and tungsten alloy rods at several impact velocities with targets composed of different strength steels. Figure 21 summarizes their results for the tungsten rods (1.5 $\leq$ V $\leq$ 4 km/s) for steels with hardnesses of 180 BHN $(\sigma_y \sim 5 \times 10^9$ dynes/cm$^2$ and 300 BHN $(\sigma_y \sim 9 \times 10^9$ dynes/cm$^2)$. As is physically expected, the normalized final cavity dimension decreases with increasing target hardness (or flow stress) and increases with increasing impact velocity. The two isolated points represent the calculation results from the previous section for an assumed static strength of $(1 \times 10^{10}$ dynes/cm$^2)$ and a slightly larger penetrator dimension $(r_p = .39$ cm). The experimental data do not identify the dependence of penetrator strength and density or target density, but the calculations assume a dependence of the form:

$$U = \frac{1}{1 + \sqrt{\rho/\rho_p}} \ V$$

so as the penetrator density is decreased, the penetration rate will decrease and one should then observe a decrease in the cavity dimension for the same impact velocity. This trend is observed by comparing the experimental data presented in Figure 22 with Figure 21. The results for the high hardness steel (300 BHN) show negligible penetrator density influence but for the lower hardness alloy (180 BHN) the effect is more pronounced and follows the predicted trend. The four separate points on Figure 22 represent the model's final cavity predictions for the following parameter values:
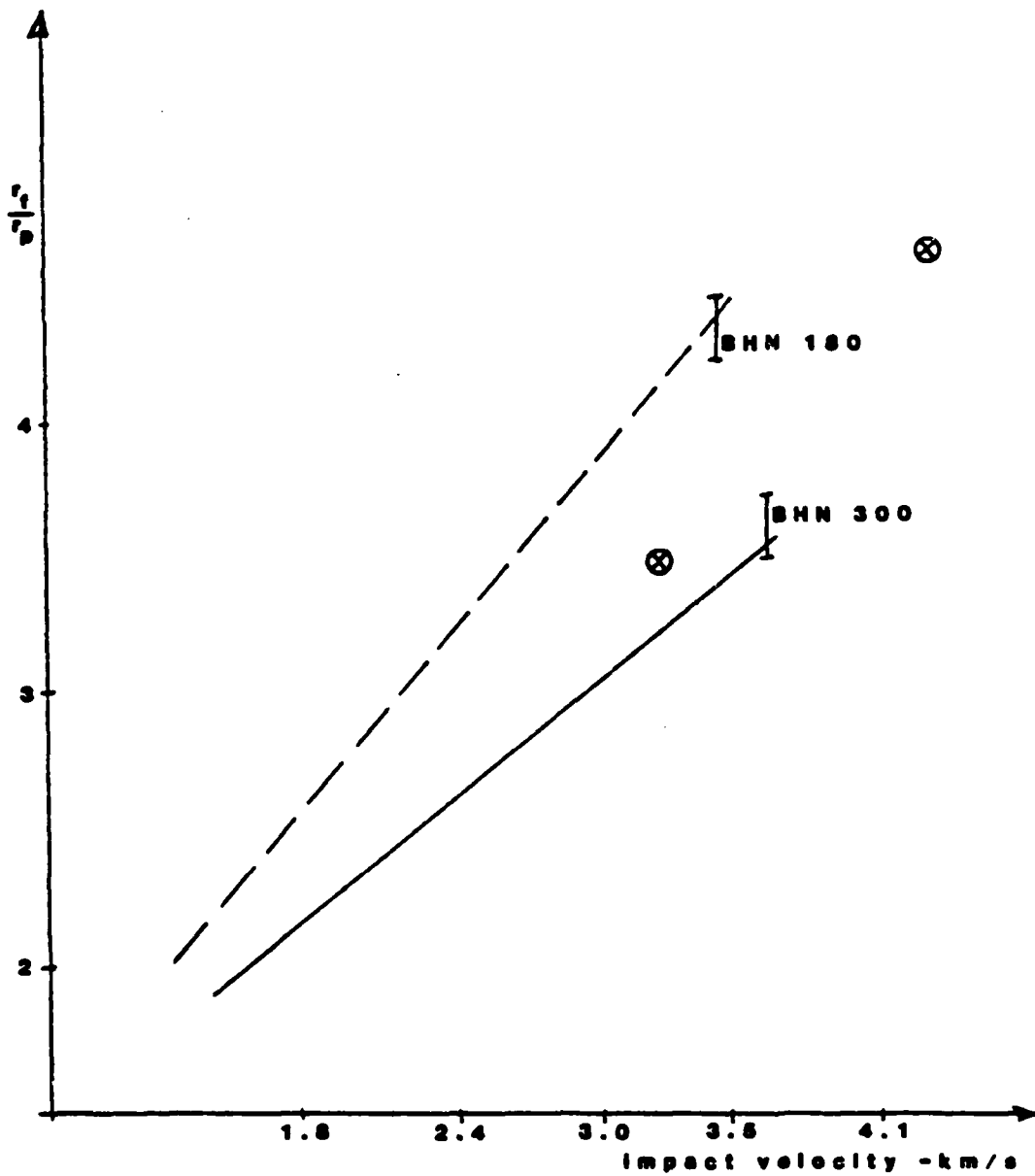
Figure 21. The Normalized Cavity Dimension Variation with Respect to Impact Velocity and Target Strength for Tungsten Rods and Steel Targets.
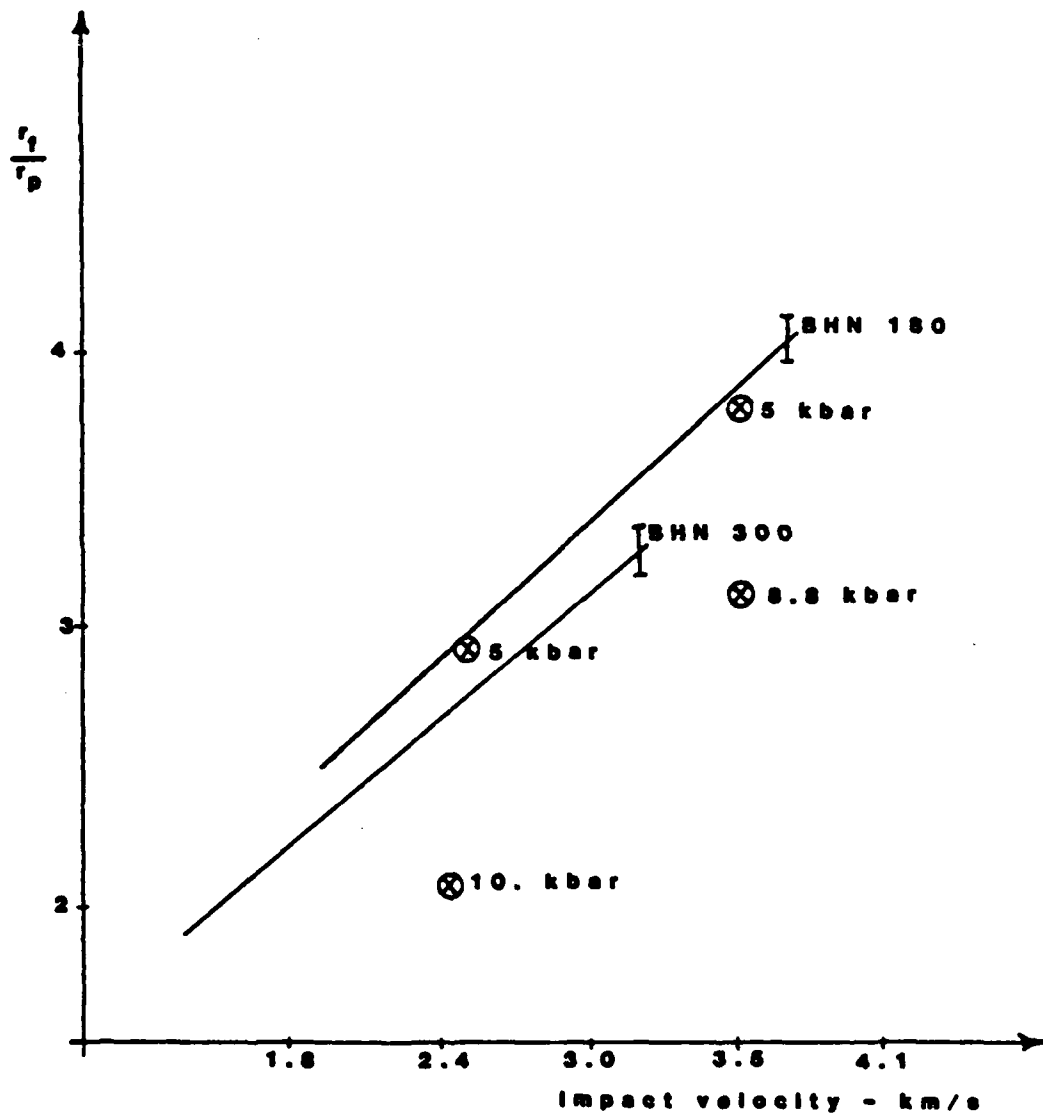
Figure 22. The Normalized Cavity Dimension Variation with Respect to Impact Velocity and Target Strength for Steel Rods and Steel Targets.

$\rho_p = 7.8$ g/cm$^3$ (measured)

$\rho = 7.8$ g/cm$^3$ (measured)

$r_p = .27$ cm (measured)

$\mu = 2 \times 10^4$ poise (from section 4-1)

$\sigma_y = 5 \times 10^9$ dynes/cm$^2$ (estimated)

to $1 \times 10^{10}$ dynes/cm$^2$ (estimated)

$V = 3.5 \times 10^5$ cm/s

and $1.18 \times 10^5$ cm/s

$K = .78$.

Once again the initial values of $a_o$ and $b_o$ must be estimated such that the initial radial stress at $a_o$ equals the stagnation pressure. The following values were used:

| | | | |
|---|---|---|---|
| $V = 3.5$ km/s | $\sigma_y = 5 \times 10^9$ dynes/cm$^2$ | $a_o = .090$ cm | $b_o = .692$ cm |
| | $\sigma_y = 8.8 \times 10^9$ dynes/cm$^2$ | $a_o = .082$ cm | $b_o = .473$ cm |
| $V = 2.4$ km/s | $\sigma_y = 5 \times 10^9$ dynes/cm$^2$ | $a_o = .080$ cm | $b_o = .350$ cm |
| | $\sigma_y = 1.0 \times 10^{10}$ dynes/cm$^2$ | $a_o = .090$ cm | $b_o = .350$ cm |

and the growth curves are presented in Figure 23. The variation of the final cavity dimension with respect to both the static yield strength and impact velocity qualitatively agrees with the experimental trend. Quantitatively, the agreement is good for the lower strength alloy but the calculations overestimate the high strength alloy in Figure 22 and underpredict the high strength alloy in Figure 21. Part of this discrepancy is undoubtedly attributable to the uncertainty of the static yield strength. Hohler and Stilp [66] note an observed range of measured hardness for the high strength alloy between 260 and 330 BHN. The quoted yield strength varies between $8.8 \times 10^9$ and $1.08 \times 10^{10}$ dynes/cm$^2$. The growth rate model is concerned with the flow stress; the static yield strength is only one component of this property and material viscosity influences the instantaneous value. Therefore, the two parameters, $\sigma_y$ and $\mu$ must be more precisely defined in order to improve the agreement. Eichelberger [14] presents a relationship between the target Brinell hardness and an "average flow stress" defined by the proportionality of crater volume and penetrator kinetic energy. The relationship for this flow stress, $\sigma$, is: $\sigma = 2.6 \times 10^8 \times$ (BHN). Therefore, the expected flow stress for the high strength alloy (BHN = 300) should be of the order, $8 \times 10^{10}$ dynes/cm$^2$. This value is an order of magnitude higher than the static yield strength, $\sigma_y = 9 \times 10^9$ dynes/cm$^2$. The Hohenemser-Prager yield assumption relates the flow stress with the static yield stress in the following way:

$$\sigma = \sigma_y + \mu \frac{\dot{\phi}}{r^2} \qquad (147)$$
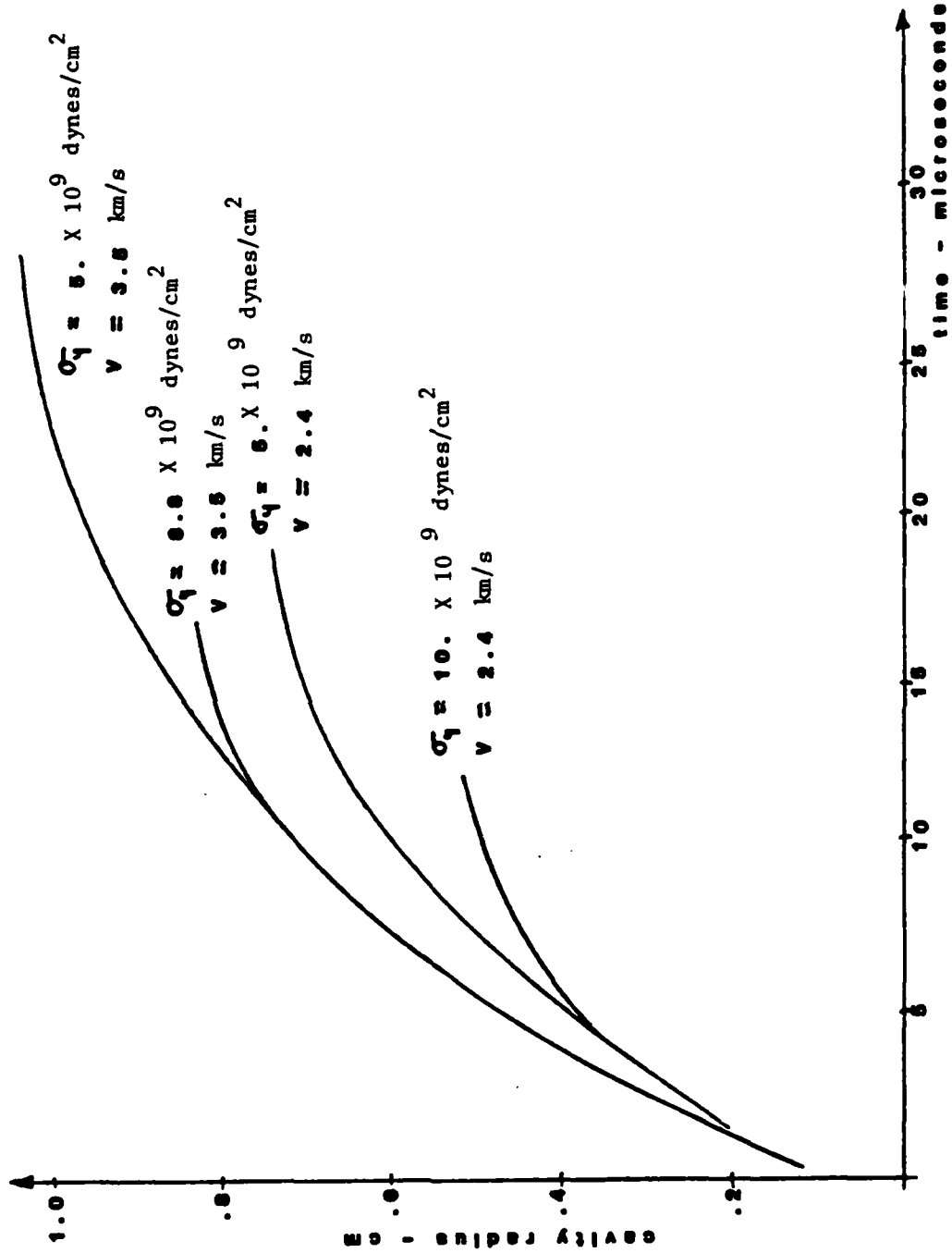
Figure 23. Radial Cavity Growth for Steel Rods Penetrating Steel Targets.

and with the initial values, $\dot{\phi}(o) = 1.12 \times 10^4$ cm/s and $r(o) = a_o = .082$ cm

for the high strength alloy case. As shown in Figure 23, the influence of the

viscosity coefficient is clear. In this case, $\sigma = 9 \times 10^9 + \mu(1.66 \times 10^6)$

dynes/cm$^2$. A value of $\mu = 2 \times 10^4$ was determined by Harlow [55] and used in
these calculations. Initially, when the velocities (rates of strain) are
greatest, the viscous contributions predominate the flow stress. The sensi-
tivity of the calculations to the viscosity coefficient will be investigated
in the next section. Leave it to say that the flow stress has a pronounced
effect upon the final cavity dimension but, unfortunately, a precise value for
this parameter is not available in general.

As an additional check of the overall model, calculations of cavity growth
in aluminum targets are presented. Perez [81] published the results of impact
tests involving steel rod penetrators into 2024 aluminum targets with
velocities ranging between 2 and 4 km/s. Perez assumes the static yield

strength for this aluminum alloy as $2 \times 10^9$ dynes/cm$^2$. The Metals Handbook

[124] gives the tensile strength as $4 \times 10^9$ dynes/cm$^2$; therefore, both values
will be independently assumed and the calculation results will be compared
with the data of Perez. Figure 24 presents the calculated growth curves for
the following problem parameters:

$$\rho_p = 7.8 \text{ g/cm}^3$$
$$\rho = 2.7 \text{ g/cm}^3$$
$$r_p = .15 \text{ cm}$$
$$\sigma_y = 2 \times 10^9 \text{ dynes/cm}^2$$
$$\quad 4 \times 10^9 \text{ dynes/cm}^2$$
$$V = 2.5 \times 10^5 \text{ cm/s}$$
$$\quad 4.0 \times 10^5 \text{ cm/s}$$
$$K = .78$$

and $\mu = 5 \times 10^3$ poise (Walters [125]).

The initial condition parameters are:

| | | | |
|---|---|---|---|
| V = 2.5 km/s | $\sigma_y = 2 \times 10^9$ dynes/cm$^2$ | $a_o = .050$ cm | $b_o = .281$ cm |
| | $\sigma_y = 4 \times 10^9$ dynes/cm$^2$ | $a_o = .044$ cm | $b_o = .186$ cm |
| V = 4.0 km/s | $\sigma_y = 2 \times 10^9$ dynes/cm$^2$ | $a_o = .057$ cm | $b_o = .551$ cm |
| | $\sigma_y = 4 \times 10^9$ dynes/cm$^2$ | $a_o = .052$ cm | $b_o = .340$ cm . |

The trends are similar to those observed in the steel targets with the
exception that the times required for cavity arrest are consistently shorter
in the aluminum target. The difference is most likely due to the relative
magnitudes of the radial momentum distributions. The data of Perez [81] is
reproduced in Figure 25 along with the four calculated final cavity
dimensions. The model predictions again qualitatively agree with the
experiment but since the flow stress (or $\sigma_y$ and $\mu$ parameters) are not

precisely known, a quantitative comparison should not be attempted.
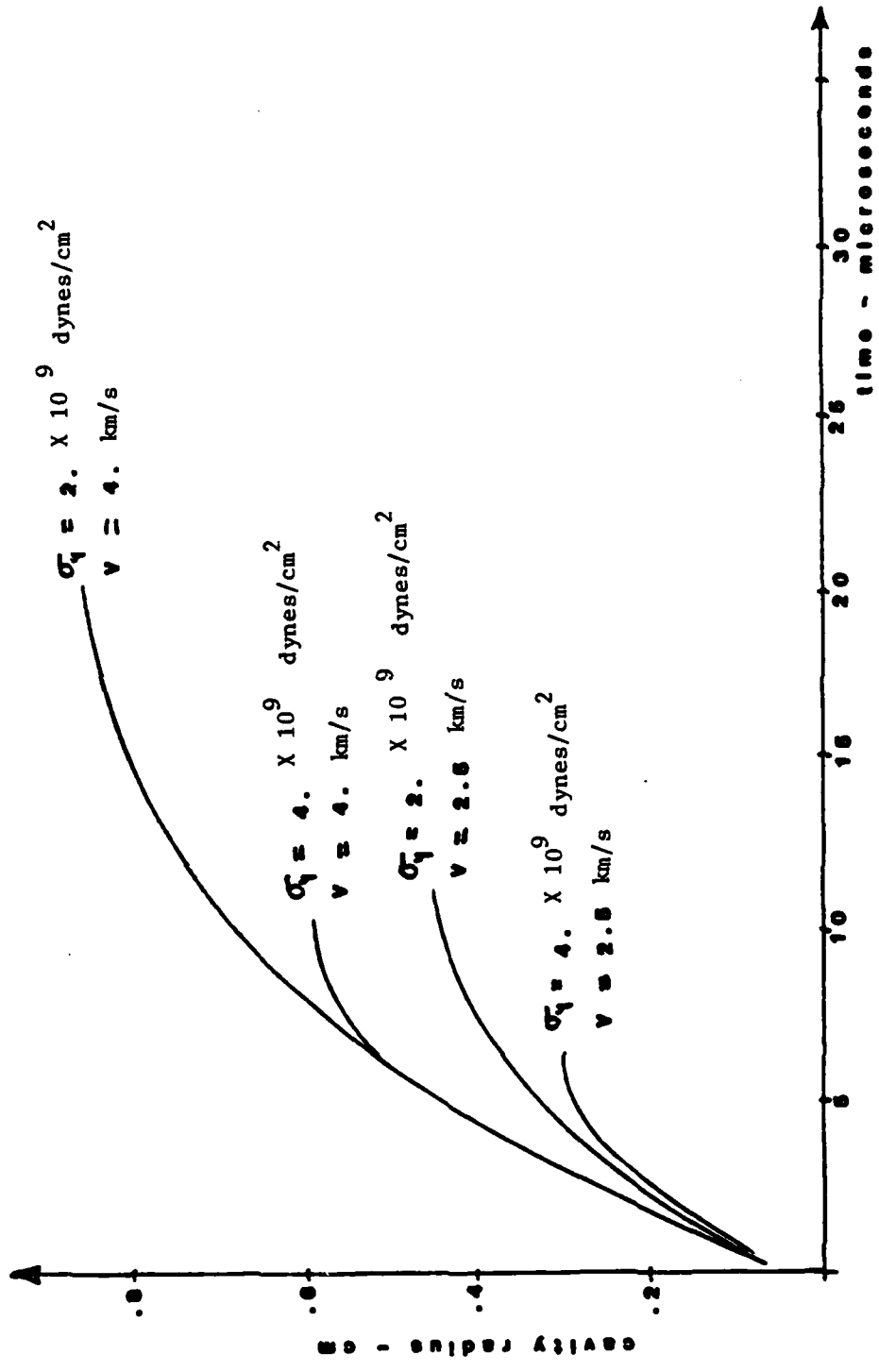
Figure 24. Radial Cavity Growth for Steel Rods Penetrating Aluminum Targets.
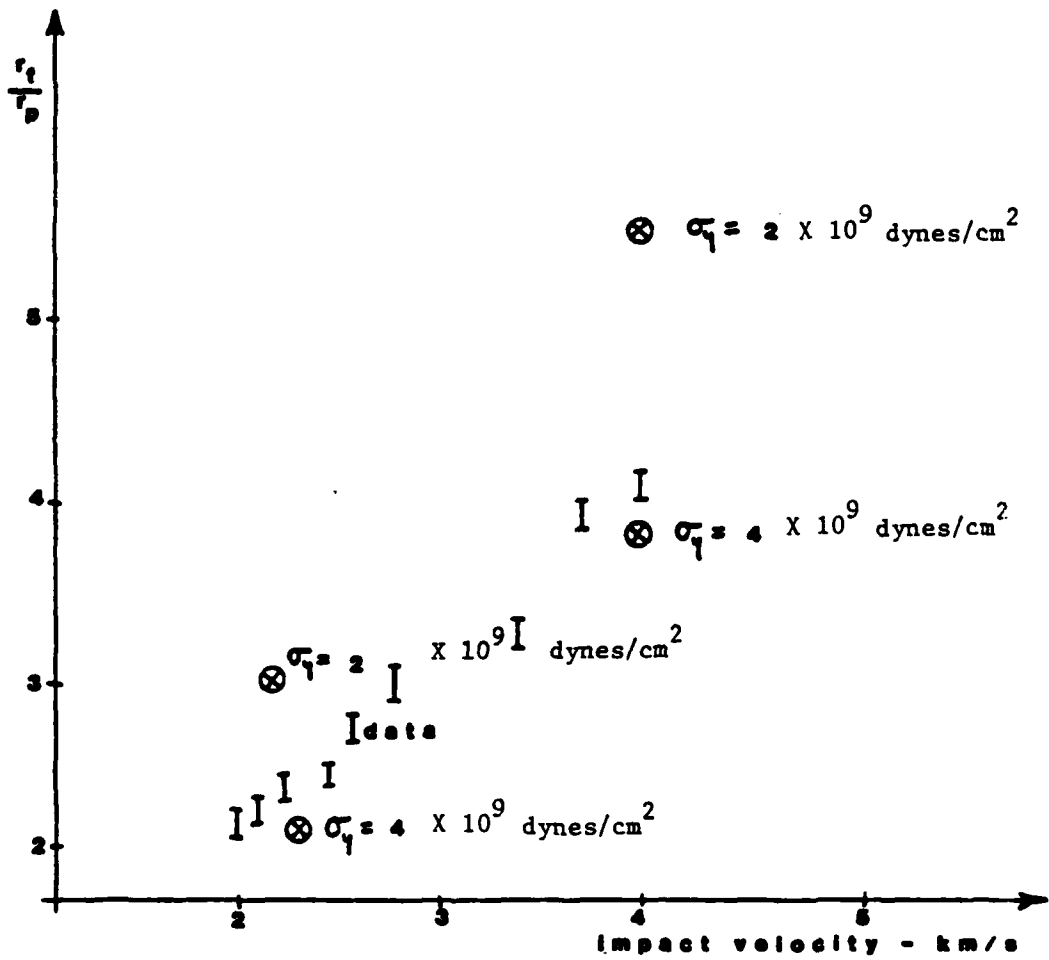
Figure 25. The Normalized Cavity Dimension Variation with Respect to Impact Velocity for Steel Rods and Aluminum Targets.

## C.  Dependence upon the Viscosity

As noted in Appendix B, the neglect of viscosity effects within impact and penetration problems is not justifiable in general.  In the previous section it was observed that the flow stress has an important role in determining the final cavity dimension and that both the static yield strength, $\sigma_y$ and the target viscosity, $\mu$, influence the specific value of this flow stress.  This section will be concerned with the viscous contribution only.  No experiments have been performed that isolate the material viscosity parameter and its influence upon the target cavity dimension.  A parametric variation of the viscosity coefficient will yield a variation in the predicted growth behavior. A particular case of study is chosen to compare with the finite difference calculation of Kucher [56] and the problem parameters are:

$$\rho_p = 8.9 \text{ g/cm}^3$$
$$\rho = 7.8 \text{ g/cm}^3$$
$$r_p = 0.1 \text{ cm}$$
$$\sigma_y = 1.36 \times 10^{10} \text{ dynes/cm}^2$$
$$V = 7.6 \times 10^5 \text{ cm/s}$$
$$K = .78$$

and the target viscosities considered are, in poise, $\mu = 1 \times 10^0$, $1 \times 10^2$, $1 \times 10^4$ and $1 \times 10^5$.

The initial conditions for the first three viscosities are determined from equation (130) and for the last viscosity from equation (128) since the approximation (129) is not appropriate for this order of magnitude.  The initial values are:

$\mu = 1 \times 10^0$, $1 \times 10^2$, $1 \times 10^4$    $a_o = .036$ cm    $b_o = .368$ cm

$\mu = 1 \times 10^5$                     $a_o = .045$ cm    $b_o = .461$ cm

and the resulting calculations are presented along with the calculation of Kucher [56] in Figure 26.  The effect of viscosity is not significant until values of the order of $10^4$ poise or greater are selected.  For viscosities greater than $\sim 1 \times 10^4$ poise, the influence is not linear.  An order of magnitude variance of the viscosity coefficient produces a reduction of only approximately 30% of the final cavity dimension.  Therefore, reasonable estimates should be expected as long as the viscosity coefficient can be determined to within the correct order of magnitude.  Walters [125] notes that given the current state of understanding, an order of magnitude estimate is perhaps as good as one might expect.  The relative importance of the viscosity coefficient can be observed explicitly in the relation for the flow stress, equation (147).  Depending on the magnitude of the static yield strength, the local radial velocity, $\phi/r$ and the radial position, the coefficient may or may not affect this flow stress.  For the range of these parameters encountered in this example, viscosity on the order of $10^4$ poise or greater will contribute significantly to the value of the flow stress.
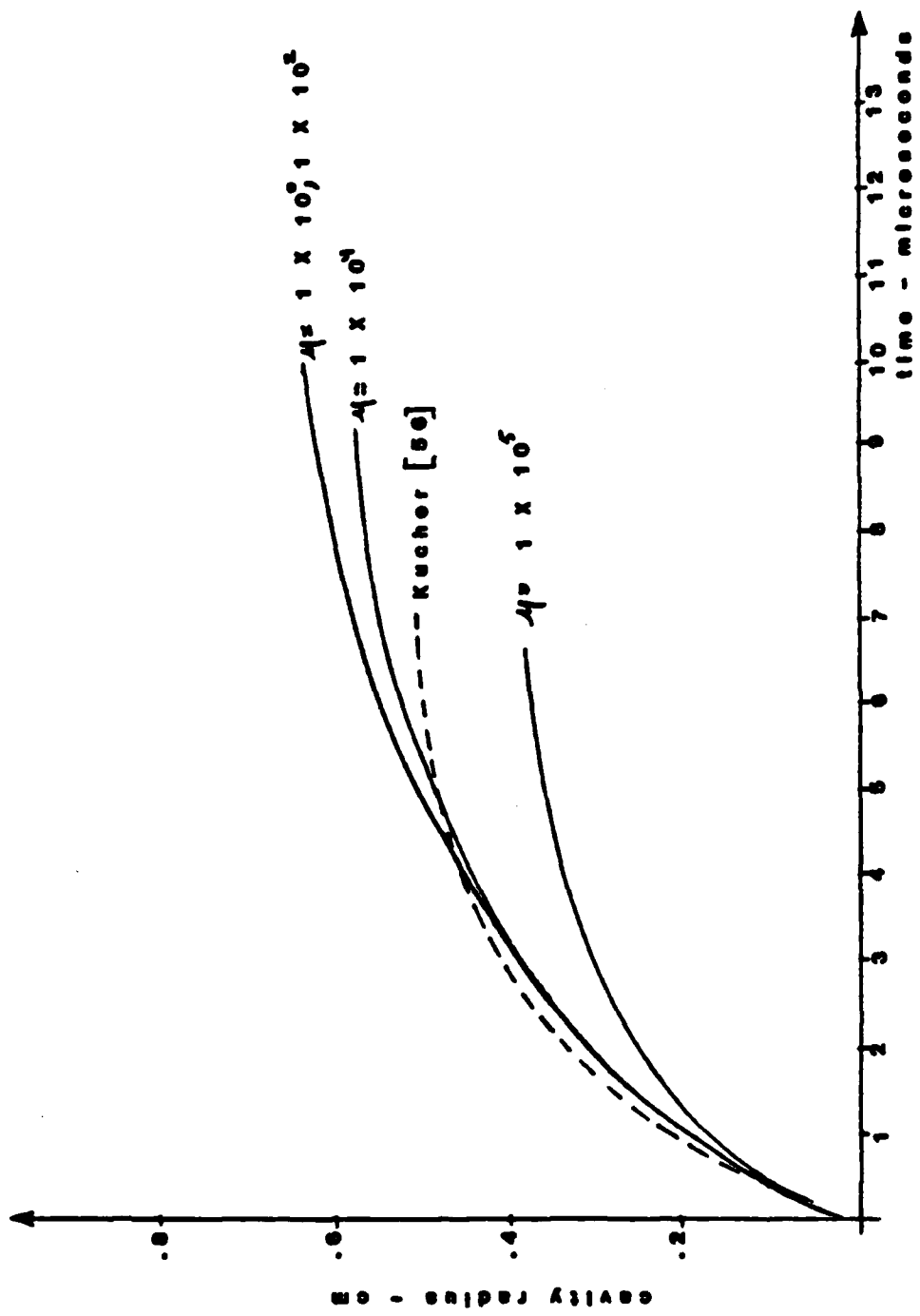
Figure 26. Parametric Dependence of the Viscosity Coefficient, $\eta$, Upon the Cavity Growth Behavior.

74

The finite difference calculation of Kucher [56] utilized an Eulerian, compressible and explicitly inviscid formulation but the computational method introduced an implicit, effective viscosity of undetermined magnitude; although it is known to have the form

$$\mu_{\text{effective}} = 1/2\rho\overline{U}\Delta x$$

where $\Delta x$ represents the characteristic mesh dimension and $\overline{U}$ is the local mean fluid speed. Assuming the results of Kucher are accurate, the value of $\mu = 2 \times 10^4$ poise (determined by Harlow [55]) yields the growth model solution with the same final cavity dimension. However, it should be pointed out that the two differ slightly in the early time growth rates.

## D. Dependence upon Penetrator Radius

The governing equations (88, 92, and 96) include the penetrator dimension, $r_p$, as a problem parameter. One would expect that the target cavity would increase if the penetrator diameter were increased (all other parameters held constant). This is reflected in the normalized data published by Hohler and Stilp [66] and Perez [81] which assert a linear scaling between penetrator and cavity dimensions. Frequently, the penetrator dimension is not known precisely, especially for shaped-charge jets. For these situations a range of values is typically assumed and predictions are similarly determined. As an example of the growth model's ability to handle such a problem, the following parameters are assumed:

$$\rho_p = 8.9 \text{ g/cm}^3$$
$$\rho = 7.8 \text{ g/cm}^3$$
$$r_p = 0.15, \ 0.2, \ 0.3 \text{ cm}$$
$$V = 6.9 \times 10^5 \text{ cm/s}$$
$$K = 0.78$$
$$\sigma_y = 1 \times 10^{10} \text{ dynes/cm}^2$$
and $\mu = 2 \times 10^4$ poise.

This case represents typical high speed jet penetration. Dipersio, et al. [126] radiographically measured jet velocities and dimensions at selected times after charge detonation. The jet was copper and had a linear velocity distribution that varied between 8.3 and 1.0 km/s. At three inches deep within the target, the jet was eroded to an incoming velocity of 6.9 km/s and the jet radius was estimated to be between .15 and 0.3 cm in dimension. The initial condition parameters can be iteratively determined and are:

| | | |
|---|---|---|
| $r_p = 0.15$ cm | $a_o = .056$ cm | $b_o = .601$ cm |
| $r_p = 0.2$ cm | $a_o = .074$ cm | $b_o = .80$ cm |
| $r_p = 0.3$ cm | $a_o = .112$ cm | $b_o = 1.20$ cm . |

Figure 27 presents the calculated growth curves for the specified input parameters. The measurements [126] were taken at three inches deep into the
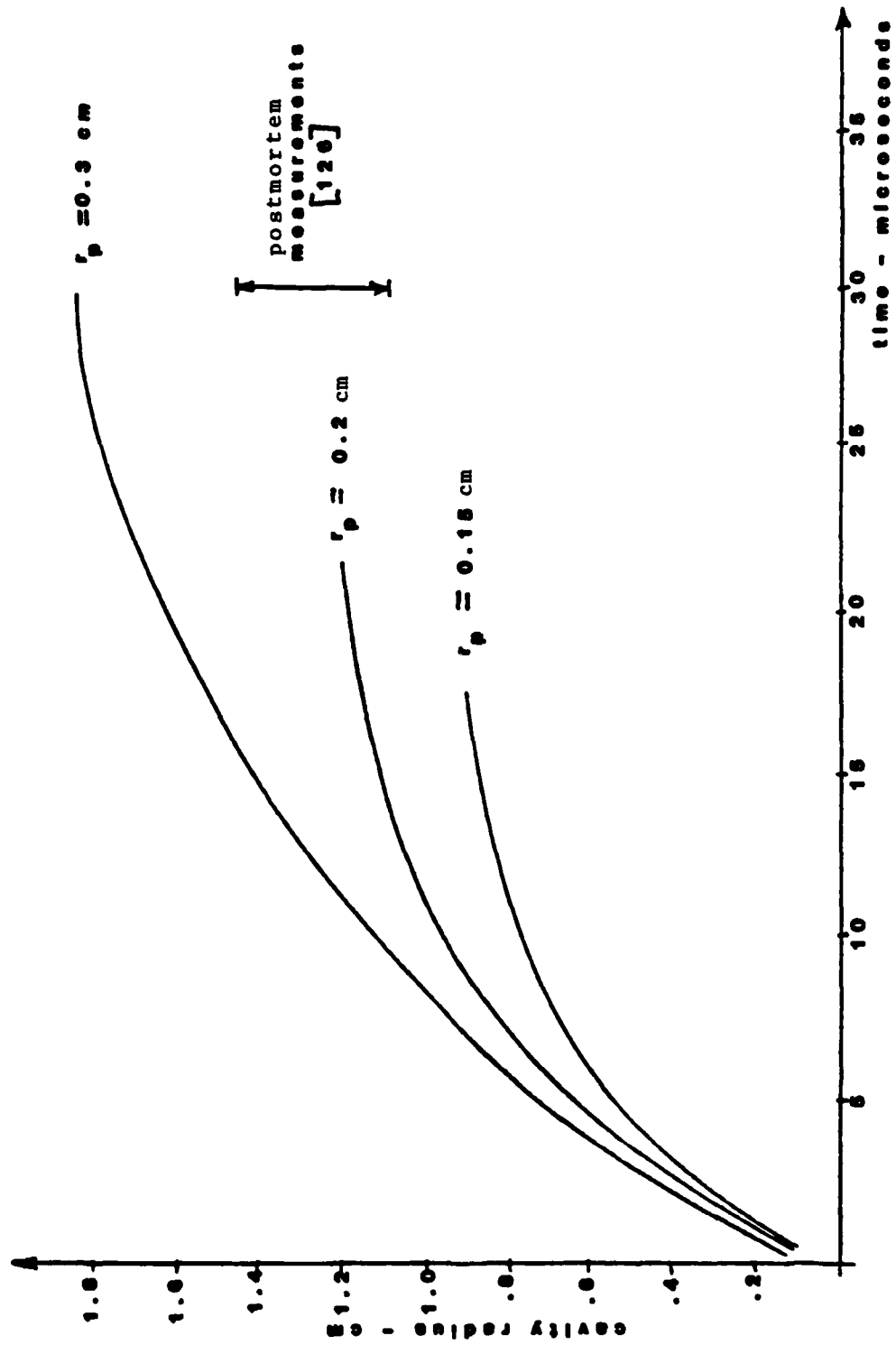
Figure 27. Parametric Dependence of the Penetrator Radius, $r_p$, upon the Cavity Growth Behavior.

target (where steady conditions would be likely) and represent several test shots for the same configuration. The cross section of the hole at each axial position is not perfectly circular, therefore measurements were made for the greatest and the least diameter at each axial plane. The cavity growth model predictions for final cavity radius identify the linear dependence upon the penetrator dimension. The time required to reach the final cavity dimension also exhibits a linear dependence upon this parameter. The experimental measurements lie within the range of the calculated predictions for the estimated range of jet radii.

## E.  Comparison Between Semi-infinite and Finite Lateral Boundaries

The preceding sections compare postmortem measurements with the model predictions for ranges of the problem parameters. All cases have assumed that the target dimension in the plane of the entrance surface is large in comparison with the penetrator diameter or cavity dimension. This configuration is typically the case in practice but occasionally the question arises; if the lateral dimension is not overwhelmingly large, what will be the effect upon the growth behavior prediction? The formulation of the governing equations includes this possibility. Equation (88) was derived under the presumption that the lateral boundary is circular in cross section and is relatively small in dimension. The radial stress is assumed to vanish at this surface. As an example of how the behavior will change if the lateral boundary is small, the aluminum target case of section IVB will be recalled. The following parameters are assumed:

$$\rho_p = 7.8 \text{ g/cm}^3$$
$$\rho = 2.7 \text{ g/cm}^3$$
$$r_p = 0.15 \text{ cm}$$
$$V = 4.0 \times 10^5 \text{ cm/s}$$
$$K = 0.78$$
$$\sigma_y = 2 \times 10^9 \text{ dynes/cm}^2$$
$$\text{and } \mu = 5 \times 10^3 \text{ poise.}$$

The initial condition parameters were iteratively determined for the semi-infinite case from equation (134) but if the lateral boundary is known and the radial stress is set to zero upon this surface, then equation (128) must be utilized. The boundary, $b_o$, will be assumed to be 0.4 cm; the initial cavity position is then iteratively determined to be 0.050. The calculated result for this finite boundary problem is presented along with the semi-infinite solution in Figure 28. Initially ($t < 5 \mu s$) the two curves are similar but as time proceeds, a difference develops. The semi-infinite target curve exhibits a gradual deceleration of the cavity until the motion is arrested due to the diminishing plastic stresses. Once the yield criterion is no longer met, the problem is terminated since only elastic displacements could continue. The plastic region is always bounded by an elastic region of infinite mass.

The finite lateral boundary problem exhibits noticably different behavior. The deceleration for times greater than 5 microseconds is less than that for
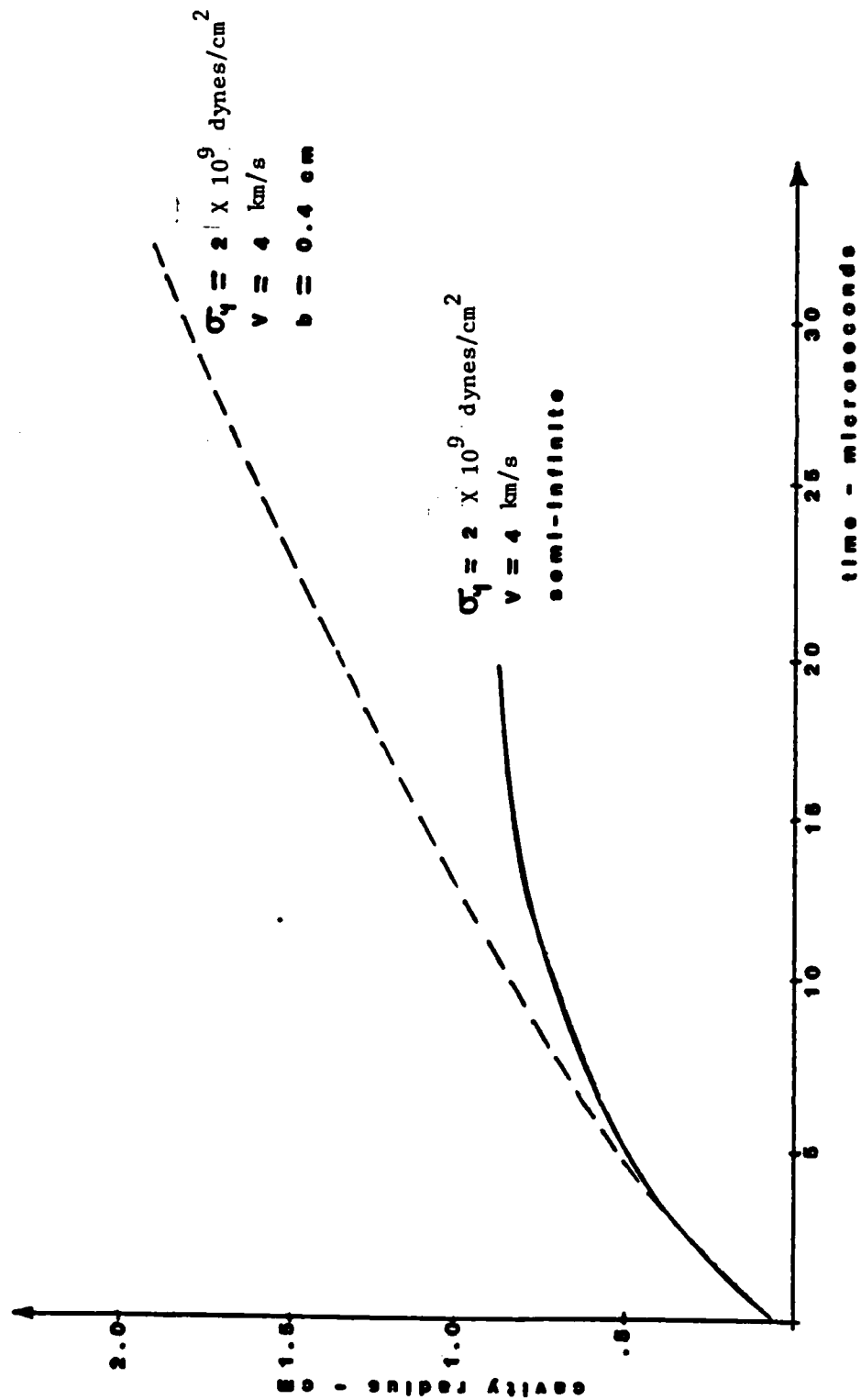
Figure 28. Comparison Between Semi-Infinite and Finite Lateral Boundaries.

78

the semi-infinite case. It is, however, not zero so the problem will continue for a much longer time. At 40 microseconds, the difference between $a_o$ and $b_o$ is .03 cm at a radius of 2.3 cm. The target then appears as a thin, expanding cylinder. The strain experienced by the tube material may be estimated by

$$\frac{u_r}{r_o} \sim \frac{r}{r_o} = \frac{2.3}{0.05} = 46 \text{ at } t = 40 \ \mu s.$$

It is, therefore, likely that fracture or instabilities would have set in by this time in an actual problem and that the original plasticity assumption may not even apply. It would be difficult to perform an experimental measurement of the final "tube" dimension if it could even be recovered intact. Perhaps a more suitable measurement to compare with this calculation would be to measure the outer surface velocity in an average manner with the use of a high speed framing camera. At this point, such an experiment has not been performed. From the calculation results alone, it can be qualitatively stated that decreasing the lateral boundary dimension will increase the cavity dimension.

## F. Comparison with Entrance Hole Data

Throughout this chapter the calculated final cavity dimensions were compared with experimental data. Experiments have not been published that measure the growth behavior during the expansion process deep within the target. However, radial cavity growth at the initial impact surface has been observed radiographically [14, 35] and at least the shapes of the experimental curves are similar to the shapes of the predicted curves for the steady penetration problem. In order to compare, qualitatively, the initial transient growth behavior with the deep, steady growth behavior, the following configuration will be assumed. Eichelberger [14] considered the entrance hole expansion in an aluminum (1100F) target block resulting from the impact of a short steel disc, $V = 5$ km/s. If instead, the disc thickness is assumed many times longer, then a steady penetration condition should occur and the equations in Section IIF should then apply. The experiment involving the transient entrance surface [14] can then be compared with the predicted behavior that would result if the penetrator had greater length. The problem parameters are:

$$\rho_p = 7.8 \text{ g/cm}^3$$
$$\rho = 2.7 \text{ g/cm}^3$$
$$r_p = 0.4 \text{ cm}$$
$$V = 5.0 \times 10^5 \text{ cm/s}$$
$$\sigma_y = 2 \times 10^9 \text{ dynes/cm}^2 \text{ (assumed)}$$
$$K = .78 \text{ (assumed)}$$

and $\mu = 5 \times 10^3$ (as in Section IVB).

The initial condition parameters are iteratively determined as: $a_o = .151$ cm, $b_o = 1.928$ cm and the penetration velocity, U is calculated from the steady penetration model (Appendix A) as $3.15 \times 10^5$ cm/s. This value is less than the elastic wave speed in aluminum. Therefore, equation (92), the

79

subsonic, semi-infinite case, will be utilized. Figure 29 presents both the experimental measurement for the entrance surface and the calculated prediction for axial planes deep within the target. The two curves are considerably different in terms of both final dimension and instantaneous slope (velocity). The isolated sources of the discrepancy (ignoring the uncertainty of the values of yield strength and viscosity) are the difference in the axial boundary conditions, the length of the penetrator and the degree of transient axial behavior. If the free surface boundary condition were the only variable involved, it would be expected that the final cavity dimension for the steady problem be less than the final dimension for the entrance surface. The transient penetration rate lies between the impact velocity and steady penetration rate; consequently the initial condition on radial velocity would be greater and, therefore, it would be expected that the entrance cavity be larger than the cavity at some depth into the target. However, the results show just the opposite behavior. This is attributable to the difference in penetrator length. Eichelberger fired a steel disc (radius = 0.4 cm, length = 0.05 cm) end on at the semi-infinite aluminum target. Steady axial behavior was never achieved and due to the very short length, relaxation from the rear penetrator surface reduced the time over which the penetrator could interact with the target. Subsequently, less radial impulse is imparted to the entrance plane material than would be if the penetrator length were increased. Therefore, in order to study the effects of the transient nature of the free surface boundary of the entrance cavity, the length of the penetrator must be increased and the experiment must be repeated (keeping all other parameters fixed). The model predictions will then show the deviation associated with the transient, free boundary condition, alone.

## V.  CONCLUSIONS AND SUGGESTIONS FOR FURTHER RESEARCH

The primary intent of this report was to develop a model for the expansion of a cavity created during the penetration of hypervelocity rods and apply it by predicting parametric trends for problems of practical interest. The model was formulated by making several assumptions as to the behavior of the flowing target material during the cavity expansion process. These approximations are supported by experimental evidence and the qualitative results of finite difference calculations. By specifying stress conditions at the boundaries of the plastic regions, the governing system of nonlinear field equations was reduced to simpler ordinary differential equations. Upon estimation of the initial conditions, the initial value problems were solved numerically for several situations where experimental results were available. The following conclusions can therefore be stated:

a.  The calculated predictions of the final radial cavity dimension show the same parametric variation as the experiments.

b.  The time dependent growth of the cavity agrees qualitatively well with the finite difference calculations of Kucher [56] but is significantly different from the experimentally observed entrance hole behavior of short disc impact [14].
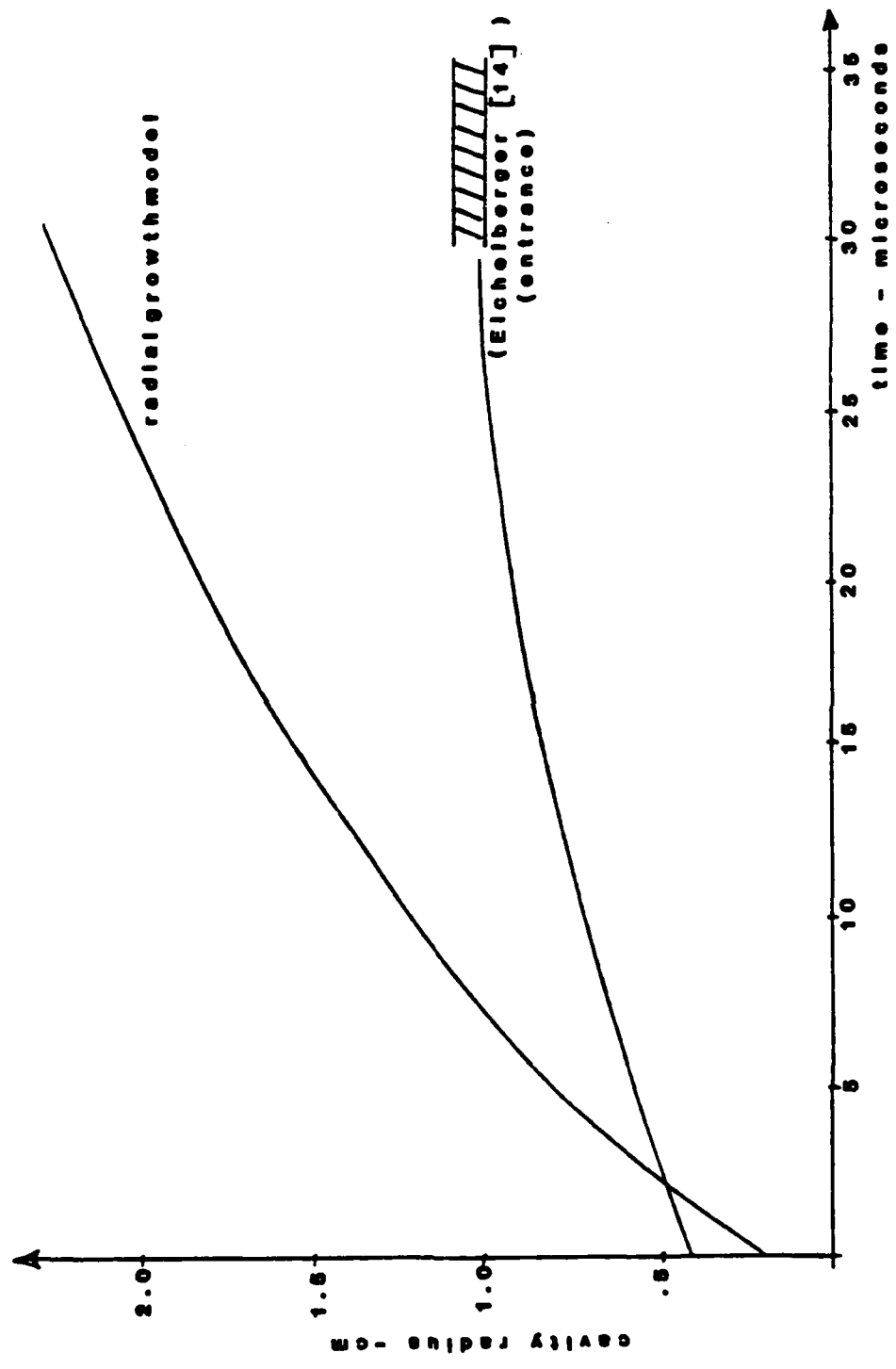
Figure 29. Comparison Between Entrance Surface Cavity Growth and the Radial Growth of Cavities Deep Within the Target.

c. The accuracy of the model predictions depends upon the accuracy with which the initial conditions (V, $r_p$, K, U) and the target material characteristics ($\sigma_y$, $\mu$) may be determined.

d. The analogy with the incompressible fluid flow over a blunt cylinder yields an estimation for the initial conditions that consistently results in close agreement with the experiments.

e. The Hohenemser-Prager visco-plastic flow assumption predicts initial flow stress values within the range of those published by Eichelberger [14] from independent experiments.

f. The analysis is applicable to cavity growth resulting from both kinetic energy penetrators (1 km/s $\leq$ V $\leq$ 4 km/s) and shaped charge jets (2 km/s $\leq$ V $\leq$ 10 km/s) as long as the physical characteristics of each is known to sufficient accuracy and the steady penetration presumption is valid.

The formulation required axial symmetry, material isotropy, plastic incompressibility and steady penetration. If any of these approximations is violated, a new formulation must be performed. As already noted in Appendix A, the steady penetration theory may not be applicable to material combinations with substantially different compressibilities or when the hydrodynamic pressure is of the order of the target strength or less. Similarly, the radial cavity expansion model is limited to problems where hydrodynamic penetration is applicable (V > 1 km/s for $\sigma_y \sim 1 \times 10^9$ dynes/cm$^2$). The model is limited also by the requirement for input values that may not be easily determined, i.e., $\mu$, $\sigma_y$, $r_p$, etc. Additionally, materials that do not exhibit plastic flow prior to rupture or fracture cannot be investigated since the plastic characteristics have implicitly been assumed to predominate the cavity expansion process.

Beyond the obvious requirement for further research of material characterization during ballistic impact, an alternate formulation of the completely transient, initial impact problem for long rod penetrators should be pursued and be compared with the results from this report. An experimental observation of the growth of the cavity, deep within the target, or stress measurements (similar to those of Pritchard [70]) at points displaced from the penetration trajectory, taken during the early expansion times, are also very much needed.

## ACKNOWLEDGMENTS

## LIST OF SYMBOLS
### (Units According to CGS Convention)

$a(t)$      – radial position of the cavity surface

$a_o$      – initial value of $a$

$a'(t)$      – radial position of the boundary that separates Regions II and III

$A$      – radius of penetrator bulb, equation (100)

$\hat{A}$      – Bethe's flow stress parameter, equation (105)

$A_1$      – transform variable in Section (IIIB)

$A_i$      – cross sectional areas

$b(t)$      – radial position of the elastic/plastic boundary

$b_o$      – initial value of $b$

$b_i$      – body force vector

$B$      – Bethe's radial pressure parameter

$c(t)$      – radial position of the target lateral dimension

$c$      – wave speed

$c_o$      – elastic wave speed

$c_1$      – integration constant in Section (IIIB)

$dK$      – incremental mechanical work

$d\tau$      – incremental cavity volume

$d\phi$      – incremental control volume deflection angle

$D$      – body of revolution diameter

$D_c$      – cavity diameter

$D_p$      – penetrator diameter

$\dot{e}_{ij}$      – strain rate tensor

$\dot{e}^e_{ij}$      – elastic component of strain rate tensor

$e^p_{ij}$      – plastic component of strain rate tensor

$F$      – yield function

$\hat{F}$ — target resistance force

$K$ — initial condition parameter, equation (116)

$K_o$ — elastic boundary constant

$K_1$ — elastic boundary constant

$\overline{K}_1$ — transform constant in Section (IIIB)

$\overline{K}$ — stagnation velocity gradient

$\hat{K}$ — maximum shear rate

$L$ — length of penetrator bulb

$\hat{M}$ — transform variable in Section (IIIB)

$M$ — penetrator mass

$M_o$ — local Mach number

$n$ — transform variable in Section (IIIB)

$P$ — pressure in the penetrator control volume

$\hat{P}$ — transform variable in Section (IIIB)

$P_o$ — stagnation pressure

$P(t_F)$ — penetration depth in Appendix A

$r$ — radial coordinate

$r_p$ — penetrator radius

$R$ — radius of curvature

$S$ — relative velocity scalar

$S$ — also root to principle stress determinant

$\vec{S}$ — relative velocity vector

$S_i$ — principle stress vector

$U$ — penetration rate

$U_e$ — velocity at the edge of the boundary layer

$U_i$ — velocity vector

$U_p$ — particle velocity

| | |
|---|---|
| $\overline{U}$ | – local mean fluid speed |
| $\overline{U}_i$ | – displacement vector |
| $V$ | – impact velocity |
| $x$ | – distance from stagnation point |
| $x_i$ | – coordinate vector |
| $y$ | – transform variable in Section (IIIB) |
| $z$ | – axial coordinate |
| $\hat{z}$ | – transform variable in Section (IIIB) |
| $\gamma_{rz}$ | – shear strain in the r-z plane |
| $\delta_{ij}$ | – Kronecker delta |
| $\Delta x$ | – characteristic mesh dimension |
| $\theta$ | – circumferential coordinate |
| $\Theta$ | – angular displacement from symmetry axis |
| $\Theta_1$ | – deflection angle of microstructure bands |
| $\lambda$ | – slope of the $U_s - U_p$ data |
| $\lambda$ | – bulk viscosity coefficient, equation (46) |
| $\lambda_1$ | – empirical fitting parameter, equation (54) |
| $\mu$ | – shear viscosity coefficient |
| $\nu$ | – Poisson's ratio |
| $\pi$ | – 3.14 . . . |
| $\rho$ | – target density |
| $\rho_p$ | – penetrator density |
| $\rho_t$ | – target density |
| $\sigma$ | – average flow stress during high strain, strain rate deformation |
| $\sigma_y$ | – target yield strength in uniaxial tension, measured quasi-statically |
| $\sigma_{ij}$ | – stress tensor |

$\sigma^o_{ij}$      – rate independent components of the stress tensor

$\tau$      – target shear strength

$\emptyset$      – undetermined function of time

# REFERENCES

1. Backman, M., "Terminal Ballistics," Naval Weapons Center Publication, NWC-TP-5780 (1976).

2. Billington, E. and Tate, A., "The Physics of Deformation and Flow," McGraw-Hill, NY (1981).

3. Goldsmith, W., "Impact, the Theory and Physical Behavior of Colliding Solids," Edward Arnold LTD., London (1960).

4. Johnson, W., "Impact Strength of Materials," Edward Arnold LTD., NY (1972).

5. Kinslow, R., "High-Velocity Impact Phenomena," Academic Press, NY (1970).

6. Zukas, J., Nicholas, T., Swift, H., Greszczuk, L. and Curran, D., "Impact Dynamics," Wiley-Interscience, NY (1982).

7. Proceedings, Symposia on Hypervelocity Impact, 3-7, Defense Documentation Center, Cameron, VA (1959-1965).

8. Allison, F., "A Review of the Theories Concerning Crater Formation by Hypervelocity Impact," Proc., 3rd Symp. on Hyper. Impact, Chicago, IL (1959).

9. Cook, M. and Keyes, R., "Microsecond Framing Camera Observations of High Velocity Impact," Proc., 3rd Symp. on Hyper. Impact, Chicago, IL (1959).

10. Hopkins, H. and Kolsky, H., "Mechanics of Hypervelocity Impact of Solids," Proc., 4th Symp. on Hyper. Impact, Eglin A.F.B., FL (1960).

11. Backman, M. and Goldsmith, W., "The Mechanics of Penetration of Projectiles into Targets," Int. J. Eng. Sci., Vol. 16, 1 (1978).

12. Bjork, C., "The Effects of Meteroid Impact on Steel and Aluminum in Space," Proc., 10th Int. Astronautical Congress, London (1959).

13. Cook, M., "Mechanism of Cratering in Ultra-High Velocity Impact," J. Appl. Phys., Vol. 30, No. 5, 725 (1959).

14. Eichelberger, R. and Kineke, J., "Hypervelocity Impact," Kurzeitphysik, Vollrath ed., Springer-Verlag, NY (1967).

15. Herrmann, W. and Jones, A., "A Survey of Hypervelocity Impact Information," A.S.R.L. Report No. 99-1 (1961).

16. Jones, A., Polhemus, J. and Herrmann, W., "Survey of Hypervelocity Impact Information II," A.S.R.L. Report No. 99-2 (1963).

17. Prater, R., "Hypervelocity Impact-Material Strength Effects on Crater Formation and Shock Propagation in Three Aluminum Alloys," Air Force Inst. of Tech. Doctoral Dissertation (1970).

18.  Vinson, J., "On the Analysis of Structures Impacted by Hypervelocity Projectiles," Univ. of Delaware Tech. Report 89 (1968).

19.  Bethe, H., "Attempt of a Theory of Armor Penetration," Frankford Arsenal Report (1941).

20.  Perez, E., "Experimental and Theoretical Study on the Penetration of Semi-Infinite Metal Targets by Great-Length Metal Projectiles With a Velocity Higher Than 2000 m/s," Sciences et Techniques de l'Armement, Vol. 56, No. 1, Paris (1982).

21.  Wright, T., "A Survey of Penetration Mechanics for Long Rods," U.S. Army Ballistic Research Laboratory Report, ARBRL-TR-02496 (1983).

22.  Byrnside, N., Torvik, P. and Swift, H., "Impact Crater Formation at Intermediate Velocities," J. Basic Eng., 394 (1972).

23.  Christman, D., Wenzel, A. and Gehring, J., "Penetration Mechanisms of High-Velocity Rods," Proc. 7th Symp. on Hyper. Impact, Tampa , FL (1964).

24.  Christman, D. and Gehring, J., "Analysis of High-Velocity Projectile Mechanics," J. Appl. Phys., Vol. 37, No. 4 (1966).

25.  Eichelberger, R., "Summary: Theoretical and Experimental Studies of Crater Formation," Proc. 6th Symp. on Hyper. Impact, Cleveland, OH (1963).

26.  Gehring, J., Meyers, C. and Charest, J., "Experimental Studies of Impact Phenomena and Correlation With Theoretical Models," Proc. 7th Symp. on Hyper. Impact, Tampa, FL (1964).

27.  Jonas, G. and Zukas, J., "Mechanics of Penetration: Analysis and Experiment," Int. J. Eng. Sci., Vol. 16, 879 (1978).

28.  Sagamonyan, A., "Penetration of Solids into Compressed Continuous Media. Chapter III.  Penetration of Solids After High Speed Impact," Izdat. Moskovskogo Universiteta, 250 (1974).  (In Russian)

29.  Abbott, K., "Metallurgical Observations of High Speed Impact," Watertown Arsenal Laboratories Tech. Report 161-85/1 (1960).

30.  Holloway, L., "Observations of Crater Growth in Wax," U.S. Army Ballistic Research Laboratory Report, MR-1526 (1963).

31.  Johnson, W., Travis, F. and Loh, S., "High Speed Cratering in Wax and Plasticine," Int. J. Mech. Sci., Vol. 10, 593 (1968).

32.  Keys, R., Bartlett, R. and Cook, M., "Framing Camera Observations of Ultra-High Velocity Penetration in Transparent Targets and a Mechanism for Crater Expansion," Proc., 4th Symp. on Hyper. Impact, Eglin A.F.B., FL (1960).

33.  Kineke, J., "An Experimental Study of Crater Formation in Lead," Proc. 3rd Symp. on Hyper. Impact, Chicago, IL (1959).

34. Pond, R. and Glass, C., "Metallurgical Observations and Energy Partitioning," High-Velocity Impact Phenomena, Academic Press, NY (1970).

35. Turpin, W. and Carson, J., "Hole Growth in Thin Plates Perforated by Hypervelocity Pellets," Air Force Materials Laboratory Report, TR-70-83 (1970).

36. Yuan, S. and Billingsley, T., "An Experimental Investigation of High Velocity Impact," Appl. Sci. Res., Vol. 24, 431 (1971).

37. Davids, N. and Huang, Y., "Shock Waves in Solid Craters," J. Aero. Sci., Vol. 29, No. 5, 550 (1962).

38. Fuchs, O., "Impact Phenomena," A.I.A.A. J., Vol. 1, No. 9, 2124 (1963).

39. Öpik, E., "Researches on the Physical Theory of Meteor Phenomena: 1. Theory of the Formation of Meteor Craters," Acta et Comm. Univ. Tartuensis (1936).

40. Rae, W. and Kirchener, H., "A Blast Wave Theory of Crater Formation in Semi-Infinite Targets," Proc., 6th Symp. on Hyper. Impact, Cleveland, OH (1963).

41. Rand, J., Anderson, C. and Wilbeck, J., "A Parametric Analysis of the Penetration Process," Proc., 8th Int. Symp. on Ballistics, Hauge, Netherlands (1983).

42. Rostoker, N., "The Formation of Craters by High Speed Particles," Meteoritics, 11 (1952).

43. Seizew, M., Kuhl, A. and Blankenship, V., "The Role of Viscosity of Solids in Microparticle Cratering," Acta. Astronautica, 5 (1978).

44. Silberstein, I., "Crater Size in Hypervelocity Impact," Ph.D. Dissertation, Univ. of Illinois (1967).

45. Scott, B. and Walters, W., "A Model of the Crater Growth Rate Under Ballistic Impact Conditions," Proc., 12th Southeastern Conf. on Theor. and Appl. Mech., Georgia (1984).

46. Taylor, G., "Formation and Enlargement of a Circular Hole in a Thin Plastic Sheet," Quart. J. Mech. Appl. Math., Vol. 1, 103 (1948).

47. Whitesides, J. and Yuan, S., "Viscous Effects on Hypervelocity Impact," J. Appl. Phys., Vol. 42, No. 11, 4156 (1971).

48. Zaid, M., "An Analytical Approach to Hypervelocity Impact Mechanics," Proc., 4th Symp. on Hyper. Impact, Eglin A.F.B., FL (1960).

49. Hardage, B., "Hypervelocity Impact with Flow and Shock Penetration Through Fluid, Plastic and Elastic Zones," Ph.D. Dissertation, Oklahoma State Univ. (1967).

50. Riney, T., "Solutions of Viscoplastic Equations for Axisymmetric Hypervelocity Impact," Air Proving Ground Center Tech. Doc. Report, TDR-62-74 (1962).

51. Riney, T., "Visco-Plastic Solution of Hypervelocity Impact Cratering Phenomenon," Proc., 6th Symp. on Hyper. Impact, Cleveland, OH (1963).

52. Riney, T., "Depth of Penetration of Hypervelocity Projectiles," A.I.A.A. J., Vol. 3, No. 1, 52 (1965).

53. Sedgewick, R., Hageman, L., Herrmann, R. and Waddell, J., "Numerical Investigations in Penetration Mechanics," Int. J. Eng. Sci., Vol. 16, 859 (1978).

54. Wilkins, M., "Mechanics of Penetration and Perforation," Int. J. Eng. Sci., Vol. 16, 793 (1978).

55. Harlow, F. and Pracht, W., "Formation and Penetration of High Speed Collapse Jets," Phys. of Fluids, Vol. 9, No. 10, 1951 (1966).

56. Kucher, V., "Computer Study of the Effects of Rod Diameter and Target Thickness on the Penetration Process," U.S. Army Ballistics Research Laboratory Report, ARBRL-TR-02046 (1978).

57. Kucher, V., "Multiple Impacts on Monolithic Steel," U.S. Army Ballistics Research Laboratory Report, ARBRL-TR-02406 (1982).

58. Birkhoff, G., MacDougall, D., Pugh, E. and Taylor, G., "Explosives With Lined Cavities," J. Appl. Phys., Vol. 19, No. 6, 563 (1948).

59. Boyle, V., "Transient Hypervelocity Impact Phenomena in a Transparent Target," U.S. Army Ballistics Research Laboratory Report, BRL-MR-1567 (1964).

60. Brooks, P., "On the Prediction of Crater Profiles Produced in Ductile Materials by the Impact of Rigid Penetrators at Ballistic Velocities," Def. Res. Board Report, D.R.E.V. R-686/73, Quebec, Canada (1973).

61. Eichelberger, R. and Rostoker, N., "Jet and Target Characteristics," 14th Bimonthly Report (CIT-ORD-17), FUNDAMENTALS OF SHAPED CHARGES, Carnegie Inst. of Tech. (1948).

62. Eichelberger, R., "Experimental Test of the Theory of Penetration by Metallic Jets," J. Appl. Phys., Vol. 27, No. 1, 63 (1956).

63. Fugelso, E., Taylor, J. and Hantel, L., "Evalutation of Combined Obliquity and Yaw for U-.75 wt. % Penetrators," L.A.S.L. Report (1976).

64. Glass, J. and Bruchey, W., "Internal Deformation and Energy Absorption During Penetration of Semi-Infinite Targets," Proc., 8th Int. Symp. on Ballistics, Hauge, Netherlands (1983).

65. Hauver, G., "Penetration with Instrumental Rods," Int. J. Eng. Sci., Vol. 16, 871 (1978).

66. Hohler, V. and Stilp, A., "A Penetration of Steel and High Density Rods in Semi-Infinite Steel Targets," Proc., 3rd Int. Symp. on Ballistics, Karlsruhe, F.R.G. (1977).

67. Johnson, W., Sengupta, A., Gosh, S. and Reid, S., "Mechanics of High Speed Imapct at Normal Incidence Between Plasticine Long Rods and Plates," J. Mech. Phys. Solids, Vol. 29, No. 5/6, 413 (1981).

68. Moss, G., Toms, S., Vitalli, R. and Merindino, A., "Effect of Target Microstructure on Penetration by Shape Charge Jets," U.S. Army Ballistics Research Laboratory Report, BRL-MR-1739 (1966).

69. Pond, R. and Hsu, W., "Hypervelocity Target Dynamics as Seen by Three Dimensional Markers," J. of Spacecraft, Vol. 7, No. 5, 594 (1970).

70. Pritchard, D., "Measurements of Dynamic Stress and Strain Components in Targets Struck by Penetrators," U.S. Army Ballistics Research Laboratory Report, ARBRL-MR-03095 (1981).

71. Summers, J. and Niehaus, W., "A Preliminary Investigation of the Penetration of Slender Rods in Thick Metal Targets," N.A.S.A. Tech. Note, D-137 (1959).

72. Weihrauch, G., "Das Verhalten von Kupferstiften beim Auftreffen auf Verschiedene Werkstoffe mit Geschwindigkeiten Zwischen 50 m/s und 1650 m/s," RAPPORT-BERRICHT 7/71, Deutsch-Französisches Forschungsinstitut, SAINT-LOUIS (1971).

73. Weihrauch, G. and Lehr, H., "Experimental Studies on Terminal Ballistics of Kinetic Energy Projectiles," Proc., 3rd Int. Symp. on Ballistics, Karlsruhe, F.R.G. (1977).

74. White, J., Wahll, M. and Backoffen, J., "Observations of Compressibility Related Effects in Shaped Charge Jet Penetration," J. Appl. Phys., Vol. 53, No. 6, 4515 (1982).

75. Mok, C., "Effects of Solid Strength on the Propagation and Attenuation of Spherical and Plane Shock Waves," J. Appl. Phys., Vol. 39, No. 4, 2072 (1968).

76. Torvik, P. and Prater, R., "A Simple Model for the Shock Wave Induced by High Speed Impact," J. of Spacecraft and Rockets, Vol. 9, No. 1, 13 (1972).

77. Eichelberger, R. and Gehring, J., "Effects of Meteroid Impacts on Space Vehicles," Am. Rocket Soc. J., Vol. 32, 1583 (1961).

78. Alekseevskii, V., "Penetration of a Rod Into a Target at High Velocity," Fizika Goveniya i Vzryva, Vol. 2, 99 (1966). (in Russian)

79. Hill, R., Mott, N. and Pack, D., "Penetration by Munroe Jets," Ministry of Supply Theoretical Research Report No. 2/44 (1944).

80. Majerus, J., Walters, W. and Neitzel, G., "Impact Models for Penetration and Hole Growth," Proc., 4th Int. Symp. on Ballistics, Monterey, CA (1978).

81. Perez, E., "A Theory for Armor Penetration by Hypervelocity Long Rods," Proc., 4th Int. Symp. on Ballistics, Monterey, CA (1978).

82. Sagamonyan, A., "The Piercing of a Plate by a Thin Solid Projectile," Matematika, Mekhanika, Vol. 30, No. 5, 104 (1975). (in Russian)

83. Tate, E., "A Theory for the Deceleration of Long Rods After Impact," J. Mech. Phys. Solids, Vol. 15, 387 (1967).

84. Tate, E., "Further Results in the Theory of Long Rod Penetration," J. Mech. Phys. Solids, Vol. 17, 141 (1969).

85. Wright, T., "Penetration With Long Rods: A Theoretical Framework and Comparison with Instrumented Impacts," U.S. Army Ballistics Research Laboratory Report, ARBRL-TR-02323 (1981).

86. Kucher, V., "Preliminary Computer Computations for Slender Rod Impact Problems," U.S. Army Ballistics Research Laboratory Report, ARBRL-TR-1957 (1977).

87. Backman, M., "Elastic and Plastic Behavior in the Impact of Cylinders Against Plates," J. Appl. Phys., Vol. 30, No. 9, 1397 (1959).

88. Cristescu, N., "Dynamic Plasticity," North Holland, Amsterdam (1967).

89. von Karman, T. and Duwez, P., "The Propagation of Plastic Deformation in Solids," J. Appl. Phys., Vol. 21, 987 (1950).

90. Koehler, J. and Seitz, F., "On the Propagation of the Plastic Deformation Produced by an Expanding Cylinder," N.D.R.C. Armor and Ordnance Report, A-139 (1943).

91. Kolsky, H., "Stress Waves in Solids," Dover Pub., NY (1963).

92. Lipkin, J. and Kipp, M., "Wave Structure Measurements and Analysis in Hypervelocity Impact Experiments," J. Appl. Phys., Vol. 47, No. 5, 1979 (1976).

93. Frazier, J. and Karpov, B., "Impact Experiments in Wax," Proc., 5th Symp. on Hyper. Impact, Denver, CO (1961).

94. Dong, Y. and Chen, T., "An Experimental Research of the Vertical Penetrating Process of High-Velocity, Long-Rod, Armor-Piercing Projectiles," Acta Armamentarii, No. 2 (1981).

95. Timoshenko, S. and Goodier, N., "Theory of Elasticity," McGraw-Hill, NY (1934).

96. Appelby, E., "The Dynamic Viscoplastic Expansion of a Cylindrical Tube," J. Appl. Mech., 654 (1964).

97.  Al-Hassani, S., Hopkins, H. and Johnson, W., "A Note on the Fragmentation of Tubular Bombs," Int. J. Mech. Sci., Vol. 11, 545, (1969).

98.  Agagabian, E., "Stresses in a Tube Produced by Sudden Load Application," Ukrainskiy Matematicheskiy Zhurnal, Inst. Matematiki, Vol. 5, No. 3, 325 (1953).  (in Russian)

99.  Allen, D. and Sopwith, D., "The Stresses and Strains in a Partly Plastic Thick Tube Under Internal Pressure and End-Load," Proc. Roy. Soc., London, A, Vol. 205, 69 (1950).

100.  Cook, G., "The Stresses in Thick Walled Cylinders of Mild Steel Overstrained by Internal Pressure," Inst. Mech. Eng., 407 (1934).

101.  Hill, R., Lee, E. and Tupper, S., "The Theory of Combined Plastic and Elastic Deformation with Particular Reference to a Thick Tube Under Internal Pressure," Proc. Roy. Soc., London, A, Vol. 191, 278 (1947).

102.  Kachanov, L., "Foundations on the Theory of Plasticity," North-Holland Pub., London (1971).

103.  Nadai, A., "Plasticity," McGraw-Hill Pub., NY (1931).

104.  Wagner, M., "Analytical Study of Penetration Mechanics," Naval Weapons Center Contract Report, N00123-68-C-0839 (1969).

105.  Godunov, S., Deribas, A., Zabrodin, A. and Kozin, N., "Hydrodynamic Effects in Colliding Solids," J. Comp. Phys., Vol. 5, 517 (1970).

106.  Godunov, S., Deribas, A., Zakharenko, I. and Mali, V., "Investigation of the Viscosity of Metals in High-Velocity Collisions," Fizika Goreniya i Vzryva, No. 1, 135 (1971).  (in Russian)

107.  Hohenemser, K. and Prager, W., "Über die Ansätzer der Mechanik Isotroper Kontinua," Zeit. f. Angew, Math. und Mech., Band 12, Heft 4 (1932).

108.  Prager, W., "Linearization in Viscoplasticity," Oestereichisches Ingenieur-Archiv, Vol. 15 (1961).

109.  Fung, Y., "Foundations of Solid Mechanics," Prentice Hall Pub., London (1965).

110.  Alder, B., ed., "Methods in Computational Physics, Vol. 3, Fundamental Methods in Hydrodynamics," Academic Press, NY (1964).

111.  Moss, G., "Shear Strains, Strain Rates and Temperature Changes in Adiabatic Shear Bands," Shock Waves and High Strain-Rate Phenomena in Metals, Plenum Pub., NY (1981).

112.  Marsh, S., "LASL Shock Hugoniot Data," Univ. of California Press, Berkeley, CA (1980).

113. Kohn, B., "Compilation of Hugoniot Equations of State," Air Force Weapons Laboratory Report, AFWL-TR-69-38 (1969).

114. Van Thiel, M., "Compendium of Shock Wave Data," Lawrence Radiation Laboratory Report, UCRL-50108, Vol. 1 (1966).

115. White, F., "Viscous Fluid Flow," McGraw-Hill Pub., NY (1974).

116. Trimmer, L., Arnold Eng. Dev. Center, AEDC-TR-68-99, TN (1968).

117. Kaplan, C., "The Flow of a Compressible Fluid Past a Sphere," NACA Tech. Note 762 (1940).

118. Gill, S., "A Process for the Step-by-Step Integration of Differential Equations in an Automatic Digital Computing Machine," Proc. Camb. Phil. Soc., Vol. 47, 96 (1951).

119. Runge, C., "Uber die Numerische Aufl"o"sung von Differential-gleichungen," Math. Ann., 46 (1895).

120. Cohen, A., "Numerical Analysis," John Wiley Pub., NY (1963).

121. Silsby, G., "Semi-Infinite Armor Penetration by Long Rods at 2.0 to 4.5 km/s," Proc. DARPA/DARCOM Armor/Anti-Armor Program Review, Arlington, VA (1983).

122. Blanks, J., "Penetration Test of Semi-Infinite Steel Targets by Tungsten Alloy Rods," Arnold Eng. Dev. Center Report, TSR-83-V26, TN (1983).

123. Walsh, J., Schreppler, R. and Willig, F., "Limiting Conditions for Jet Formation in High Velocity Collisions," J. Appl. Phys., Vol. 24, No. 3, 349 (1953).

124. Lyman, T., "Metals Handbook, 8th ed.," Am. Soc. Metals, Ohio (1964).

125. Walters, W., "Influence of Material Viscosity on the Theory of Shaped Charge Jet Formation," U.S. Army Ballistics Research Laboratory Report, ARBRL-MR-02941 (1979).

126. Dipersio, R., Simon, J. and Merendino, A., "Penetration of Shaped Charge Jets into Metallic Targets," U.S. Army Ballistics Research Laboratory Report, ARBRL-TR-1296 (1965).

127. Pugh, E., "A Theory of Target Penetration of Jets," NDRC A-274 (1944).

128. Evans, W. and Ubbelohde, A., "Formation of Munroe Jets and Their Action on Massive Targets," Res. Sup. A. R. Research, 3-7 (1950).

129. Pack, D. and Evans, W., "Penetration by High-Velocity (Munroe) Jets: I," Proc. Phys. Soc., London, B64, 298 (1951).

130. Allison, F. and Vitali , R., "A New Method of Computing Penetration Variables for Shaped-Charge Jets," U.S. Army Ballistics Research Laboratory Report, BRL-R-1184 (1963).

131. Haugstad, B., "Compressibility Effects in Shaped Charge Jet Penetration," J. Appl. Phys., Vol. 52, No. 3, 1243 (1981).

132. Dullum, O. and Haugstad, B., ''On the Effect of Finite Strength in Long Rod Penetration," Forsvarets Forskningsinstitutt Rapport-81/4001, Norwegian Defense Research Establishment, Kjeller, Norway (1981).

133. Flis, W. and Chou, P., "Penetration of Compressible Materials by Shaped-Charge Jets," Proc., 8th Int. Symp. on Ballistics, Hauge, Netherlands (1983).

134. Allen, W. and Rogers, J., "Penetration of a Rod Into a Semi-Infinite Target," J. Franklin Inst., 272 (1961).

135. Van Thiel, M. and Edwards, L., "Target Penetration: Scaling and Code Consistency," Lawrence Livermore National Laboratory A-Division Quarterly Report, UCRL-50028-78-3 (1978).

136. Becker R., "Über Plastizität, Verfestigung und Rekristallisation," Zeits. Techn. Phys., 7 (1926).

137. Orowan, E., "Die Dynamische Auffassung der Kristallplastizität," Zeits. f. Phys., 89 (1934).

138. Hopkinson, B., "The Effects of Momentary Stresses in Metals," Proc. Roy. Soc., 74 (1905).

139. Elam, C., "The Influence of Rate of Deformation on the Tensile Test with Special Reference to the Yield Point in Iron and Steel," Proc. Roy. Soc., London, A, 165 (1938).

140. Davis, E., "The Effect of the Speed of Stretching and the Rate of Loading on Yielding of Mild Steel," Trans. A.S.M.E., 61 (1939).

141. Manjoine, M. and Nadai, A., "High Speed Tension Tests at Elevated Temperatures," Proc. A.S.T.M., 40 (1940).

142. Bell, J., "The Physics of Large Deformation of Crystalline Solids," Springer-Verlag Pub., NY (1968).

143. Bell, J., "The Dynamic Plasticity of Metals at High Strain Rates: an Experimental Generalization," Behavior of Materials Under Dynamic Loading, Proc. A.S.M.E., NY (1965).

144. Malvern, L., "Experimental Studies of Strain Rate Effects and Plastic Wave Propagation in Annealed Aluminum," Behavior of Materials Under Dynamic Loading, Proc. A.S.M.E., NY (1965).

145. Perzyna, P., "The Constitutive Equations for Rate Sensitive Plastic Materials," Quart. Appl. Math., Vol. 20, 321 (1963).

146. Gillis, P. and Gilman, J., "Dynamical Dislocation Theory of Crystal Plasticity," J. Appl. Phys., Vol. 36, No. 11, 3370 (1965).

95

147. Klahn, R., Mukherjee, A. and Dorn, J., "Strain Rate Effects," 2nd Int. Conf. on Strength of Metals and Alloys, Asilomar, CA, ASM, Vol. 3 (1970).

148. Alder, J. and Phillips, K., "The Effect of Strain Rate and Temperature on the Resistance of Aluminum, Copper and Steel to Compression," J. Inst. of Metals, 83 (1954).

149. Butcher, B. and Karnes, G., "Strain Rate Effects in Metals," J. Appl. Phys., Vol. 37, No. 1, 402 (1966).

150. Campbell, J., "The Yield of Mild Steel Under Impact Loading," J. Mech. Phys. Solids, Vol. 8, 54 (1954).

151. Campbell, J. and Duby, J., "The Yield Behavior of Mild Steel in Dynamic Compression," Proc. Roy. Soc., A, 236A, 24 (1956).

152. Hawkyard, J., Eaton, D. and Johnson, W., "Dynamic Yield Strength of Copper and Low Carbon Steel at Elevated Temperatures," Int. J. Mech. Sci., Vol. 10, 929 (1968).

153. Hecker, S., "Experimental Studies of Yield Phenomena in Biaxially Loaded Metals," Constitutive Equations in Viscoplasticity, A.M.D., Vol. 20, A.S.M.E., NY (1976).

154. Taylor, G., "The Use of Flat-Ended Projectiles for Determining Dynamic Yield Stress:  Theoretical Considerations," Proc. Roy. Soc., A, Vol. 194 (1948).

155. Whiffen, A., "The Use of Flat-Ended Projectiles for Determining Dynamic Yield Stress.  II Tests on Various Metallic Materials," Proc. Roy. Soc., A, Vol. 194 (1948).

156. Wilkins, M. and Guinan, M., "Impact of Cylinders on a Rigid Boundary," J. Appl. Phys., Vol. 44, No. 3, 1200 (1973).

157. White, M., "On the Behavior of a Material with a Yield Point," J. Appl. Mech., 39 (1949).

158. Zener, C. and Holloman, J., "Effect of Strain Rate Upon Plastic Flow of Steel," J. Appl. Phys., Vol. 15, 22 (1944).

159. Ludwik, P., "Elemente der Technologischen Mechanik," Springer Pub., Berlin (1909).

160. Kotliarevskii, J., Reference by Cristescu [88], J. Prike. Mech. Tech. Fiz., 6 (1961).

161. MacCormack, R., "The Effect of Viscosity in Hypervelocity Impact Cratering," A.I.A.A. Hyper. Impact Conf., Cincinnati, OH (1969).

162. Walsh, J. and Tillotson, J., "Hydrodynamics of Hypervelocity Impact," Proc. 6th Symp. on Hyper. Impact, Cleveland, OH (1963).

163. Ravid, M. and Bodner, S., "Dynamic Perforation of Viscoplastic Plates by Rigid Projectiles," Int. J. Eng. Sci., Vol. 21, No. 6 (1983).

164. N.M.A.B. Committee on Materials Response to Ultra-High Loading Rates, "Materials Response to Ultra-High Loading Rates," National Materials Advisory Board Report, No. 356, N.A.S., Washington (1980).

## APPENDIX A

## DERIVATION OF THE STEADY PENETRATION RATE

The theory describing the penetration of high speed rods and jets was developed during World War II [58, 79, 127 - 129] presumably to allow the design of armor and anti-armor warheads. Working independently, Hill, Mott and Pack [79] (England, 1944) and Pugh [127] (U.S.A., 1944) considered essentially the same configuration, as shown in Figure A1,
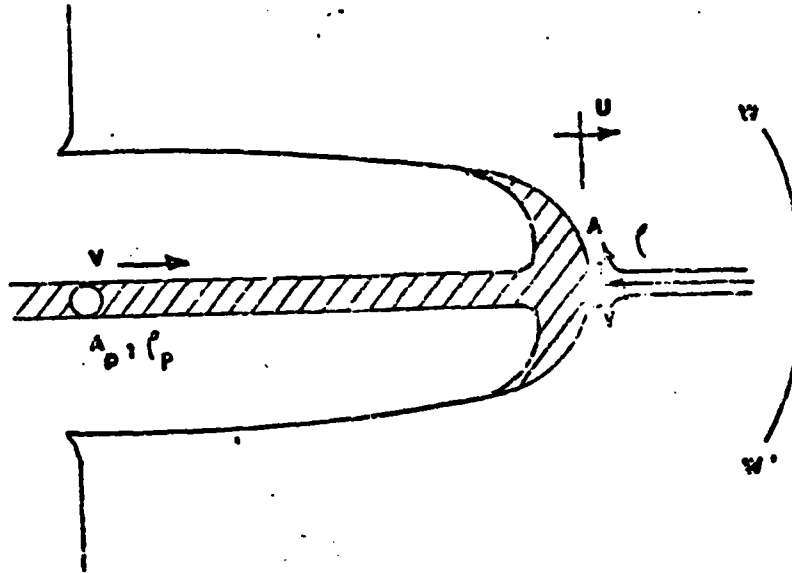


Figure A1.    The Penetration of a Semi-Infinite Target with a Long Penetrator.

where Ap represents the penetrator cross sectional $\rho$ and $\rho_p$ the target and penetrator densities, respectively. V represents the velocity of the penetrator with respect to a stationary frame, A represents the crossection of the target over which the penetrator interacts and the surface W - W' represents a shock surface (if the velocity is sufficient). The interface is presumed to translate to the right at a constant velocity, U. If the frame of reference is attached to the intersection point of penetrator surface and the symmetry axis, moving with a constant speed U, then the axial flow in this moving frame appears steady. Surface A is bombarded on one side by the penetrator moving with a relative velocity (V - U) and on the other side by target material moving in the opposite direction with relative velocity U. Within this system of translating coordinates, the incoming penetrator is sprayed out radially upon impact, losing its axial momentum. Therefore, the forces on both sides of A must be equal and opposite. Pugh, thereby obtained:

$$\rho_p Ap(V - U)^2 = \rho A U^2$$

(A.1)

and upon solving for U,

99

$$U = \frac{V}{1 + \sqrt{\frac{\rho A}{\rho_p A_p}}} \quad . \tag{A.2}$$

Equation (A.2) can be further simplified by assuming that $A = A_p$, then:

$$U = \frac{V}{1 + \sqrt{\rho / \rho_p}} \quad . \tag{A.3}$$

Hill obtained the same relationship for the penetration velocity by applying the theory of free streamlines. Upon the translating stagnation point, the pressures (given by the Bernoulli equation) must equal in both the target and penetrator. For the incompressible case,

$$1/2 \rho_p (V-U)^2 = 1/2 \rho U^2 \tag{A.4}$$

and equation A.3 then follows. Both Hill and Pugh recognized that compressibility of either the penetrator or target would influence the value of the pressure on either side of the stagnation point, i.e.,

$$\int_0^{P_0} \frac{dp}{\rho} = \left(1/2\right) U^2 \quad . \tag{A.5}$$

The effects of compressibility were subsequently studied by Allison and Vitali [130], Harlow and Pracht [55], Haugstad and Dullum [131, 132] and Flis and Chou [133]. Considering metal targets, Allison concludes that the incompressible approximation is sufficiently accurate for practical problems. Harlow, using a stiffened-gas equation of state for steel and aluminum with a multidimensional Eulerian, finite difference technique, concludes that both the steady and incompressible assumptions are quite appropriate. The works of

Haugstad and Flis, however, show that for materials with significantly different compressibilities, the error resulting from the application of the incompressible assumption to the determination of the pressure and hence penetration velocity could be on the order of 30%.

The presumption that the materials behave like fluids is based on the argument that the inherent strength of the target and penetrator materials is much less than the hydrodynamic pressure. For lesser impact velocities, this presumption is not valid and equation (A.4) is usually modified to include strength-like terms and a pressure variation term, $\gamma$,

$$\rho U^2 = \gamma \rho_p (V - U)^2 + \sigma .$$

(A.6)

With an estimate of the "resistance stress," $\sigma$ and a guess as to the value of $\gamma$, $1 \leq \gamma \leq 2$ (Eichelberger [62], Allen and Rogers [134]) the penetration velocity can be determined once again. The depth at which the penetration ceases can be estimated by assuming that the process ends when the trailing end of the penetrator reaches the stagnation point. Integrating the penetration velocity with respect to time yields the depth,

$$P(t)_F = \int_0^{t_F} U \, dt' = \sqrt{\rho_p/\rho} \int_0^{t_F} (V - U) dt = L\sqrt{\rho_p/\rho} ,$$

(A.7)

where L represents the constant penetrator length. Eichelberger [62] performed an experimental test of this theory for the case of metallic jets. The major distinction between a jet and a hypervelocity rod is that the jet has a variable velocity along its length. This casts doubt on the steady approximation and it would appear that the above equations might not be applicable to these types of penetrators. However, Eichelberger concludes that the hydrodynamic approximations are surprisingly accurate when compared with experimental evidence. This accuracy should diminish with decreasing impact velocity where the solid strength characteristics predominate. However, Christman and Gehring [24] compared the steady penetration theory with experimental data for high speed (1-6 km/s) rods and concluded that within the range of variables considered, the target strength had negligible influence on the penetration rate. This is also confirmed by the finite difference calculation of Van Thiel [135]. In review of the many experimental observations and analytic predictions, it can be assumed that the steady, incompressible penetration model produces a sufficiently accurate estimate of the penetration rate of long penetrators into semi-infinite metallic targets.

## APPENDIX B

## THE YIELD STRESS DURING BALLISTIC IMPACT

Perhaps one of the first researchers to be concerned with the effect of the yield stress variation upon the ability of a penetrator to perforate armor was H. A. Bethe [19] who published in 1941. In the formulation of his armor penetration model, he introduced the Tresca/Mohr yield criterion, which supposes that the target material exhibits an observable elastic-plastic transition stress, $\sigma_y$. This yield stress determined the magnitudes of the resistance stresses within the armor and consequently became an important problem parameter. Bethe recognized that previous theoretical works, (Becker [136] who published in 1926 and Orowan [137] who published in 1935) although not nearly complete, had predicted through statistical mechanics arguments that the yield stress at high rates of strain should be much greater than the yield stress observed in quasi-static testing. In this pioneering paper, Bethe included a review of the early experimental observations of Hopkinson [138], Elam [139], Davis [140] and Manjoine and Nadai [141] which all confirmed, at least qualitatively, the aforementioned theoretical trend. The experiments of Elam and Davis showed that even though the yield stress increased up to about one hundred sixty percent of the static value (limited by the speed of the testing machine), it did so with practically no strain hardening. The observations allowed Bethe to select an analytically tractable form for subsequent calculations. Interest in discerning the behavior of materials undergoing simultaneous large strains and rates of strain seemed to escalate during the years following; many experimental studies were published and many constitutive equations were proposed. Reviews of these works can be found in several current texts (Cristescu [88], Billington and Tate [2], Johnson [4], Zukas, et.al. [6]). The conclusion reached in all instances is that the dynamic yield stress is not a characteristic constant of the material, its value depends upon the rate of loading as well as the form of the constitutive equation used for a considered material. Quoting Cristescu, "the mechanism by which the loading rate influences the static stress-strain curve is not yet clearly understood." This is still true today and can be observed by comparing the research papers of the rate-independent, strain hardening proponents (Bell [142, 143]) with those of the rate-dependent community (Malvern [144], Perzyna [145], Gillis [146], Klahn [147], etc. and the numerous Russian workers reviewed by Walters [125]). From dynamic wave propagation experiments, Bell proposes that the following stress-strain function has "wide and remarkable generality" for strain rates up to $10^4$ sec$^{-1}$,

$$\sigma = \left(\frac{2}{3}\right)^{r^{*}/2} G(o) \, B_{\cup} \left(1 - \frac{T}{T_m}\right) \dot{\varepsilon}^{1/2}$$

(B.1)

where $G(0)$ is the static, isotropic, linear elastic, shear modulus, $r^*$ is an integer index, and $B_o$ is a universal dimensionless constant. The rate of strain does not appear explicitly within this expression. This is in contradiction to the many dynamic yield experiments performed by many researchers over many years (Alder and Phillips [148], Butcher and Karnes [149], Campbell [150, 151], Hawkyard [152], Hecker [153], Malvern [144], Taylor [154], Whiffen [155], Wilkins [156], White [157], Zener [158] and many

103

others). Alder and Phillips [148] performed experiments on aluminum, steel and copper with strain rates up to 40 $sec^{-1}$ and found they could best fit the data with a power law form:

$$\sigma = \sigma_o \dot{e}^n \qquad (B.2)$$

where $\sigma_o$ and n are experimentally determined constants. Ludwik [159] proposed the following logarithmic equation:

$$\sigma = \sigma_1 + \sigma_o \ln \frac{\dot{e}^p}{\dot{e}^p_o} \qquad (B.3)$$

where $\sigma_1$ and $\sigma_o$ are constants, and the plastic strain rate is normalized with respect to the quasi-static strain rate. Malvern [144] extended this to include work-hardening, $\sigma = f(e)$,

$$\sigma = f(e) + a\ln(1 + b\dot{e}^p). \qquad (B.4)$$

Hohenemser and Prager [107], and later Kotliarevskii [160] and Perzyna [145] assumed that rate sensitive plastic materials could be modeled with a Bingham type constitutive form,

$$\sigma = \sigma_y + \mu(P,\dot{e},T)\dot{e} \qquad (B.5)$$

where the first term is the rate independent yield stress and that the second term represents the viscous contribution of the yield stress dependent on the material viscosity, which most likely varies with the current state of the material. Many Russian researchers (see Walters [125]) have utilizied this last equation for the yield stress dependence on strain rate. Godunov, et. al. [105] reviews both the experimental evidence and the Russian modeling philosophy for many materials including the typical metals. Godunov [106], in a later report, notes the variation of the experimentally determined viscosity coefficient with different rates of deformation (strain rates) and concludes, as in Figure B1, that the viscosity coefficient has only weak dependence on the rate of strain if the strain rate is sufficiently great, i.e. $\dot{e} > 10^4$. This then simplifies equation (B.5) considerably. If the viscosity coefficient can be independently determined, given of course the expected temperature and pressure regime, then the dynamic yield stress (or flow stress as it is alternately referred to) is a linear function of the rate of strain for a specific range of this rate. The coefficient of viscosity, being approximately constant, would change when passing from one range to another. Perzyna [145], recognizing the insignificance of strain hardening in mild steel (Campbell [150, 151]), generalized the constitutive equations of Hohenemser and Prager [107] to general states of stress,
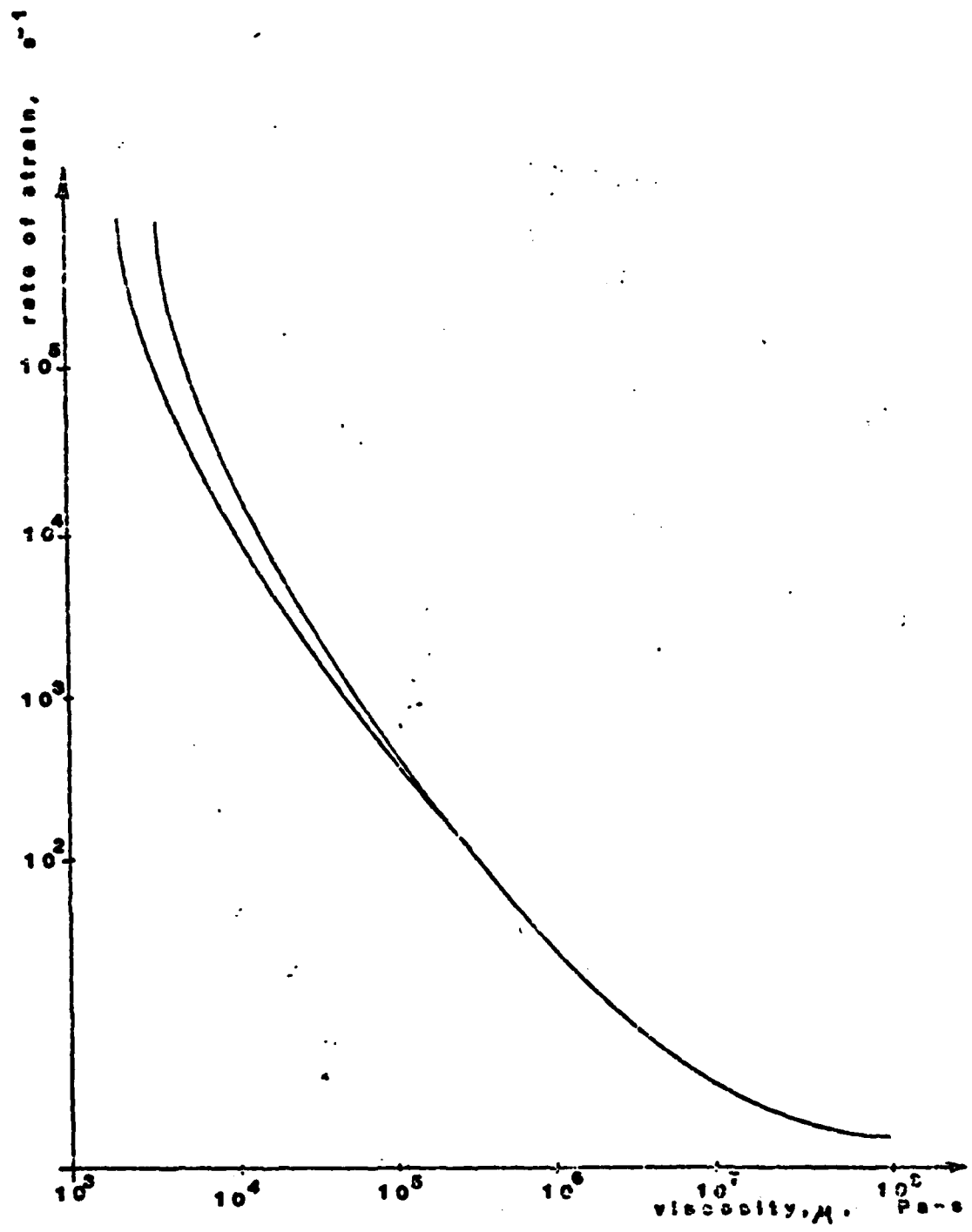
Figure B1.  Variation of Viscosity Coefficient with Rate of Strain,
Walters [125].

$$\dot{e}_{ij} = \frac{S_{ij}}{2G} + \gamma \Phi(F) \frac{\partial F}{\partial \sigma_{ij}} \qquad \text{For } F > 0$$

$$\dot{e}_{ij} = \frac{S_{ij}}{2G} \qquad \text{For } F \leq 0$$

(B.6)

$$\dot{e}_{ii} = \frac{1}{3K} \dot{\sigma}_{ij}$$

where F is the static yield function, $S_{ij}$ denote the components of stress deviation, $e_{ij}$ the components of strain deviation and the elastic constants, G and K, as well as the function $\gamma\Phi(F)$ must be determined experimentally.

The influence of viscosity upon the impact and penetration problem has been investigated theoretically by several authors. Riney [51, 52], MacCormack [161], Walsh [162] using multidimensional, explicit, finite difference techniques concluded that viscous effects are quite significant especially when characteristic dimensions are small. The analytic models of Seizew [43], Whitesides [47] and Ravid and Bodner [163] recognize that viscous effects predominate the flow in the later stages of cavity development. During the later stages, the cavity approaches its final state and the effects of the initial hydrodynamic impact stage are minimal. The neglect of rate dependence is, therefore, difficult to justify in general. The National Materials Advisory Board of the National Academy of Sciences published a summary report [164] that resulted from an extensive review of current constitutive modeling efforts oriented towards utilization within the modern numerical finite difference methods. It was concluded that the sophisticated numerical methods are ultimately limited by the current uncertainty in material response descriptions. A relatively poor understanding of the micromechanical mechanisms of dynamic plastic deformation forces the use of simple, phenomenalogical continuum models. The assumption of perfect plasticity with a constant flow stress has been found to yield "excellent agreement for a number of ordnance designs and is almost always used in ordnance calculations at present," even though the actual problems are characterized by geometric and material complexities. The flow stress is always different from the statically determined value, but its precise value is not well established. The flow stress may have explicit dependence on temperature, strain, strain rate, or pressure in a variety of functional forms.

Equations (B.1 - B.6) represent only a partial sampling of the constitutive equations that have been assumed in order to solve actual problems involving impact and the resulting plastic deformation. The behaviors of specific materials are often best modeled by only one of the above equations, and even then, only after judicious choice of the undetermined constants. The ultimate decision of which constitutive equation to use is usually based on considerations of analytic tractability, reproduction of experimental evidence and compatibility with theoretical arguments. The material constants must also be available if quantitative comparisons are desired in addition to the parametric dependencies. It should be noted at this point that errors resulting from the approximation of the material behavior will most likely manifest themselves as discrepencies between analytic predictions and experimental observations. With this in mind, review of past modeling efforts and their respective successes should be completed before selection of a particular constitutive model for a specific problem.

106

## APPENDIX C

## THE SOLUTION OF THE AXIAL VELOCITY DISTRIBUTION

The formulation of Region II involved approximations to the three dimensional flow field that were both experimentally and numerically supported. Equation (65) originates from the axial momentum equation and couples the temporal and spatial behavior of the axial velocity component as:

$$\frac{\partial U_z}{\partial t} = \frac{1}{r}\frac{\partial U_z}{\partial r}\left\{\frac{\mu}{\rho} - \dot{\emptyset}(t)\right\} ,$$

(C.1)

where $\emptyset(t)$ is the ultimate solution function determined by solving the initial value problems of Section II.F. Suppose that the axial velocity can be represented by:

$$U_z = T(t)R(r)$$

(C.2)

where T and R represent functions of time and radial coordinate respectively. Then equation (C.1) becomes:

$$R\frac{\partial T}{\partial t} = \frac{T}{r}\frac{\partial R}{\partial r}\left\{\frac{\mu}{\rho} - \dot{\emptyset}(t)\right\} .$$

(C.3)

Following arguments standard to the method of separation of variables,

$$\frac{1}{T(\frac{\mu}{\rho} - \dot{\emptyset}(t))}\frac{dT}{dt} = \frac{1}{Rr}\frac{dR}{dr} = \text{constant} = -\psi^2$$

(C.4)

the partial differential equation (C.1) has been reduced to two ordinary differential equations (C.4). Integrating both of these equations (C.4) yields

$$T = \exp\left\{-\psi^2 (\frac{\mu}{\rho}t - \emptyset(t) + C_1)\right\}$$

(C.5)

and

$$R = \exp\left\{-\psi^2 (\frac{r^2}{2} + C_2)\right\} .$$

(C.6)

107

Therefore, via equation (C.2) the axial velocity may be determined:

$$U_z = \exp\left\{ -\psi^2 (\frac{\mu}{\rho}t - \emptyset(t) + \frac{r^2}{2} + C_3) \right\} . \tag{C.7}$$

$\emptyset(t)$ must be independently determined, $C_3$ is determined by the application of the initial condition,

$$U_z(r = a_o, 0) = U$$

$$\emptyset(0) = 0$$

and equation (C.7) then becomes:

$$U_z = U \exp\left\{ -\psi^2 (\frac{\mu}{\rho}t - \emptyset(t) + \frac{r^2 - a_o^2}{2}) \right\} . \tag{C.8}$$

The eigen value $\psi$ remains undetermined but could be empirically deduced from the experimental data presented in Section II.D.

## APPENDIX D

### DESCRIPTION OF THE SOLUTION PROCEDURE

1. Determine the problem parameters,

   $r_p$, $\rho$, $\rho_p$, $\mu$, $\sigma_y$, $C_o$, $\lambda$, $V$

2. Calculate the penetration rate, $U$, from equation (A.3)

3. Determine the appropriate case: supersonic penetration, subsonic penetration and semi-infinite lateral dimension or subsonic penetration and finite lateral dimensions.

4. Select a value of $K$ ($K = \pi/4$ is suggested) and determine the remaining initial values, $a_o$ and $b_o$ by the procedure outlined in Section II.G (for example: equation (134)).

5. Select the appropriate governing equation presented in Section II.F:
   <u>supersonic</u>, (96)

$$\left\{\rho\ddot{\phi}+\sigma_y\right\}\ell n\left[\frac{a_o^2+2\phi}{b_o^2+2\phi}\right]^{1/2} + \frac{1}{2}\left(\rho\dot{\phi}^2-\mu\dot{\phi}\right)\left(\frac{1}{a_o^2+2\phi}-\frac{1}{b_o^2+2\phi}\right) + \frac{1}{2}\rho_p r_p^2 U^3$$

$$\left\{\frac{\left|\ddot{\phi}(a_o^2+2\phi)^{1/2}-\frac{\dot{\phi}^2}{(a_o^2+2\phi)^{1/2}}\right|}{\dot{\phi}^3\left(1+\frac{U^2(a_o^2+2\phi)}{\dot{\phi}^2}\right)^{3/2}}\right\} = \frac{\rho\dot{\phi}}{(b_o^2+2\phi)^{1/2}}\left\{C_o+\lambda\frac{\dot{\phi}}{(b_o^2+2\phi)^{1/2}}\right\}$$

<u>subsonic - finite lateral dimension</u>, $b_o$, (88)

$$\left\{\rho\ddot{\phi}+\sigma_y\right\}\ell n\left[\frac{a_o^2+2\phi}{b_o^2+2\phi}\right]^{1/2} + \frac{1}{2}\left(\rho\dot{\phi}^2-\mu\dot{\phi}\right)\left(\frac{1}{a_o^2+2\phi}-\frac{1}{b_o^2+2\phi}\right) + \frac{1}{2}\rho_p r_p^2 U^3$$

$$\left\{\frac{\left|\ddot{\phi}(a_o^2+2\phi)^{1/2}-\frac{\dot{\phi}^2}{(a_o^2+2\phi)^{1/2}}\right|}{\dot{\phi}^3\left(1+\frac{U^2(a_o^2+2\phi)}{\dot{\phi}^2}\right)^{3/2}}\right\} = 0$$

<u>subsonic - semi-infinite lateral dimension,</u>  (92)

$$\left\{\rho\ddot{\emptyset}+\sigma_y\right\}\left\{\ln\left[\frac{a_o^2+2\emptyset}{b_o^2+2\emptyset}\right]^{1/2}+\frac{1}{2}\left(\dot{\rho}\dot{\emptyset}^2-\mu\dot{\emptyset}\right)\left(\frac{1}{a_o^2+2\emptyset}-\frac{1}{b_o^2+2\emptyset}\right)+\frac{1}{2}\Gamma_\rho^2{}_p U^3\right.$$

$$\left\{\frac{\left|\ddot{\emptyset}(a_o^2+2\emptyset)^{1/2}-\dfrac{\dot{\emptyset}^2}{(a_o^2+2\emptyset)^{1/2}}\right|}{\dot{\emptyset}^3\left(1+\dfrac{U^2(a_o^2+2\emptyset)}{\dot{\emptyset}^2}\right)^{3/2}}\right\}=\frac{1}{2}\left(\sigma_y+\mu\frac{\dot{\emptyset}}{b^2}\right)$$

The equation (92) is included in the FORTRAN program in Table 1. The other two cases can be considered with the programming modifications outlined in Section III.A.

6.  Input all the necessary terms, in CGS units, and choose an initial time increment of $10^{-10}$ seconds. After the calculation is complete, check the solution's first cycle such that the initial pressure is that of the stagnation approximation. Adjust the time increment to confirm convergence.

DISTRIBUTION LIST

| No. of Copies | Organization | No. of Copies | Organization |
|---|---|---|---|
| 12 | Administrator<br>Defense Technical Info Center<br>ATTN: DTIC-DDA<br>Cameron Station<br>Alexandria, VA 22304-6145 | 1 | Director<br>US Army Air Mobility Research<br>and Development Laboratory<br>Ames Research Center<br>Moffett Field, CA 94035 |
| 1 | HQDA<br>DAMA-ART-M<br>Washington, DC 20310 | 1 | Commander<br>US Army Communications -<br>Electronics Command<br>ATTN: AMSEL-ED<br>Fort Monmouth, NJ 07703 |
| 1 | Commander<br>US Army Materiel Command<br>ATTN: AMCDRA-ST<br>5001 Eisenhower Avenue<br>Alexandria, VA 22333-0001 | 1 | Commander<br>ERADCOM Technical Library<br>ATTN: DELSD-L (Reports Section)<br>Fort Monmouth, NJ 07703-5301 |
| 1 | Commander<br>Armament R&D Center<br>US Army AMCCOM<br>ATTN: SMCAR-TSS<br>Dover, NJ 07801 | 1 | Commander<br>MICOM Research, Development<br>and Engineering Center<br>ATTN: AMSMI-RD<br>Redstone Arsenal, AL 35898 |
| 1 | Commander<br>Armament R&D Center<br>US Army AMCCOM<br>ATTN: SMCAR-TDC<br>Dover, NJ 07801 | 1 | Director<br>Missile and Space Intelligence<br>Command<br>ATTN: AIAMS-YDL<br>Redstone Arsenal, AL<br>35898-5500 |
| 1 | Director<br>Benet Weapons Laboratory<br>Armament R&D Center<br>US Army AMCCOM<br>ATTN: SMCAR-LCB-TL<br>Watervliet, NY 12189 | 1 | Commander<br>US Army Tank Automotive<br>Command<br>ATTN: AMSTA-TSL<br>Warren, MI 48397-5000 |
| 1 | Commander<br>US Army Armament, Munitions<br>and Chemical Command<br>ATTN: SMCAR-ESP-L<br>Rock Island, IL 61299 | 1 | Director<br>US Army TRADOC Systems<br>Analysis Activity<br>ATTN: ATAA-SL<br>White Sands Missile Range,<br>NM 88002 |
| 1 | Commander<br>US Army Aviation Research<br>and Development Command<br>ATTN: AMSAV-E<br>4300 Goodfellow Blvd<br>St. Louis, MO 63120 | | |

DISTRIBUTION LIST

| No. of Copies | Organization | No. of Copies | Organization |
|---|---|---|---|
| 1 | Commandant<br>US Army Infantry School<br>ATTN: ATSH-CD-CSO-OR<br>Fort Benning, GA 31905 | 1 | Morton-Thiokol<br>Elkton Division<br>ATTN: B. Scott<br>Box 241<br>Elkton, MD 21921 |
| 1 | Commander<br>US Army Development &<br>  Employment Agency<br>ATTN: MODE-TED-SAB<br>Fort Lewis, WA 98433 | | Aberdeen Proving Ground<br>  Dir, USAMSAA<br>    ATTN: AMXSY-D<br>        AMXSY-MP, H. Cohen |
| 1 | AFWL/SUL<br>Kirtland AFB, NM 87117 | | Cdr, USATECOM<br>  ATTN: AMSTE-TO-F<br>Cdr, CRDC, AMCCOM<br>  ATTN: SMCCR-RSP-A |
| 1 | Air Force Armament Laboratory<br>ATTN: AFATL/DLODL<br>Eglin AFB, FL 32542-5000 | | SMCCR-MU<br>SMCCR-SPS-IL |
| 1 | AFELM, The Rand Corporation<br>ATTN: Library-D<br>1700 Main Street<br>Santa Monica, CA 90406 | | |
| 10 | Central Intelligence Agency<br>Office of Central Reference<br>Dissemination Branch<br>Room GE-47 HQS<br>Washington, D.C. 20502 | | |

USER EVALUATION SHEET/CHANGE OF ADDRESS

This Laboratory undertakes a continuing effort to improve the quality of the reports it publishes. Your comments/answers to the items/questions below will aid us in our efforts.

1. BRL Report Number_____Date of Report_____

2. Date Report Received_____

3. Does this report satisfy a need? (Comment on purpose, related project, or other area of interest for which the report will be used.)_____

_____

_____

4. How specifically, is the report being used? (Information source, design data, procedure, source of ideas, etc.)_____

_____

_____

5. Has the information in this report led to any quantitative savings as far as man-hours or dollars saved, operating costs avoided or efficiencies achieved, etc? If so, please elaborate._____

_____

_____

6. General Comments. What do you think should be changed to improve future reports? (Indicate changes to organization, technical content, format, etc.)

_____

_____

_____

|  | Name _____ |
|  | Organization _____ |
| CURRENT ADDRESS | |
|  | Address _____ |
|  | City, State, Zip _____ |

7. If indicating a Change of Address or Address Correction, please provide the New or Correct Address in Block 6 above and the Old or Incorrect address below.

|  | Name _____ |
|  | Organization _____ |
| OLD ADDRESS | |
|  | Address _____ |
|  | City, State, Zip _____ |

(Remove this sheet along the perforation, fold as indicated, staple or tape closed, and mail.)